Elektromagnetische modellering
van bedrade en draadloze breedbandverbindingen

Electromagnetic Modelling
of Wideband Wired and Wireless Interconnections

Thomas Cuyckens

Promotoren: prof. dr. ir. H. Rogier, prof. dr. ir. D. De Zutter
Proefschrift ingediend tot het behalen van de graad van
Doctor in de Ingenieurswetenschappen: Elektrotechniek

Vakgroep Informatietechnologie
Voorzitter: prof. dr. ir. D. De Zutter
Faculteit Ingenieurswetenschappen en Architectuur
Academiejaar 2014 - 2015

UNIVERSITEIT
GENT

ISBN 978-90-8578-773-0
NUR 959
Wettelijk depot: D/2015/10.500/17

Electromagnetic Modelling of Wideband Wired and Wireless Interconnections

Thomas Cuyckens

Dissertation submitted to obtain the academic degree of
Doctor of Electrical Engineering

Publicly defended at Ghent University on the 3rd of March, 2015

Research funded by a doctoral grant from the Agency for Innovation by Science and Technology in Flanders (IWT)

Supervisors:

prof. dr. ir. H. Rogier
prof. dr. ir. D. De Zutter
Electromagnetics group
Department of Information Technology
Faculty of Engineering and Architecture
Ghent University
St.-Pietersnieuwstraat 41
B-9000 Ghent, Belgium
http://emweb.intec.ugent.be

Members of the examining board:

prof. dr. ir. R. Van de Walle (chairman)	Ghent University, Belgium
prof. dr. ir. D. Vande Ginste (secretary)	Ghent University, Belgium
prof. dr. ir. H. Rogier (supervisor)	Ghent University, Belgium
prof. dr. ir. D. De Zutter (supervisor)	Ghent University, Belgium
prof. dr. ir. J. Bauwelinck	Ghent University, Belgium
prof. dr. ir. J. Verhaevert	Ghent University, Belgium
dr. ir. N. Stevens	KU Leuven, Belgium
dr. ir. A. Collado	Centre Tecnològic de Telecomunicacions de Catalunya, Castelldefels, Spain

"We demand rigidly defined areas of doubt and uncertainty!"

Douglas Adams

Dankwoord in *C majeur*

Maestoso, een lang uitgesponnen V-I beweging do sol do sol do rust sol do. Tremolo forte in de violen 'Boem Paukenslag!' Fermate, het orgelpunt. Stilte . . . de solist laat zijn instrument zakken.[1]

Met deze thesis plaats ik een *orgelpunt* op vier jaar onderzoek. Een weg van labeur *forte* en concentratie *penseroso* afgewisseld met ontspanning *obligato*, repetities *furioso* en trainingen *agitato*. Dit doctoraat heeft me enorme kansen gegeven, zowel academisch als daar buiten. Vooral de vrije tijdsinvulling (*ad libitum*) is iets dat ik enorm waardeer.

Maar een doctoraat is geen *solo*werk. Vier jaar lang, eigenlijk iets langer, ben ik door een *orkest* omringd, gesteund, aangemoedigd, bijgestaan en begeleid in elke stap naar deze *finale grandioso*. En hiervoor verdienen zij niet minder dan een eigen *lofzang*.

Primo, Hendrik en Daniël, mijn promotoren, ik wil jullie bedanken om, in eerste instantie, mij de mogelijkheid te geven dit doctoraat aan te vatten, maar belangrijker, voor de steun en het vertrouwen. Ik ben jullie dankbaar voor de inzichten die jullie mij gaven, voor de geïnvesteerde tijd in het begeleiden, nalezen, *fijnstemmen*, hinten en duizend en een andere dingen. Merci! Misschien wel bijna even belangrijk, maar op een geheel andere manier, was Isabelle, *dirigente* van de administratie. Zij zorgde ervoor dat dat er geen *valse noten* in allerhande, aanvragen, bestelbonnen, weekstaten of andere *partituren* stonden, alles *alla misura*. Dank je wel! Ik wil ook de nog niet vernoemde leden van de jury bedanken voor het beoordelen van mijn *concours* en het aanreiken van kwalitatieve en waardevolle suggesties.

Secundo, den buro op -T, deze ruimte was mijn thuis in het Technicum de voorbije vier jaar. Ik heb het zien veranderen: van vier naar zes bewoners, nieuwe gordijnen, van een naar twee computerschermen/pp, etc. Ik deelde deze ruimte met fantastische mensen. De enige constante, *de tik van de metronoom*, was Arnaut. Samen zijn we aan ons doctoraat begonnen en (bijna) samen zwaaien we af. 't Waren plezante jaren. Bijna even constant, maar niet echt, was Sam. Toen ik toekwam was er Sam en nu ik wegga zijn er twee Sams (Sam de vader, zonder zoon en purple heart Sam, Sam de oudere en Sam de jongere, de synoniemen zijn legio). En niet te vergeten, Wouter, met wie ik niet enkel een onderzoeksonderwerp, maar blijkbaar ook een niet zo heel erg verre voorouder deel. En last (toegekomen), but not least, Arne en Niels, die de sfeer

[1] Deze muzikale leidraad laat me toe om Italiaanse woorden in deze tekst te smokkelen als dank voor de lekkere koffie van de Italiaanse enclave op -T

in den buro een eigen *twist* gegeven hebben. Het was een fijn een bureau met jullie te delen.

Tertio, 'den buro' was niet de enige die voor de goede sfeer zorgde. Bart, Freek en Mykola waren de oorzaak van menig weddenschap, de *componisten* van 'International Thursday' (aka 'Saint-Mykolai Day'), 'Pita Woensdag' en 'Social Friday'. Luigi heeft me meermaals geholpen bij veel te lange meetsessies. Yves was mijn *klankbord* voor muziek in het algemeen en Jazz in 't bijzonder. Yves, je zal iemand anders moeten zoeken om naar 'Jazz in het park' te gaan. Giorgos, bedankt voor de diepgaande discussies allerhande. De 'nieuwe lichting', het is aan jullie om de tradities in ere te houden en door te geven aan de toekomstige generaties,

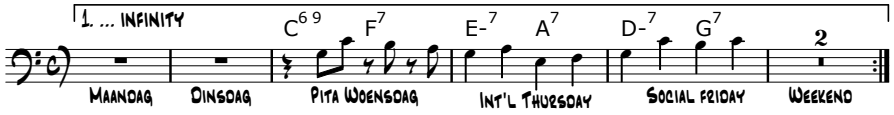

Timo, in een ver verleden collega tijdens het 'vakoverschrijdend practicum', in het recente verleden collega skiër, 't is een mooie studieperiode geweest. Je bent nog niet van mij verlost. Ook de overige collega's van -T en omstreken, zowel nu gisteren als morgen, wens ik te bedanken voor de schone tijden. *A tutti*, bedankt!

Quatro, ook buiten het technicum, zijn er vele mensen die me gesteund hebben, die een luisterend oor geweest zijn (al dan niet vrijwillig) of die er gewoon voor gezorgd hebben dat ik een fantastische vier jaar achter de rug heb. An, Billy, Delphine, Elias, Erik, Klara, Leen, Maarten, Xavier, de muzikanten van het GUSO, the Funk Engineers, the Tromboneyard en Xeado, de topatleten van Stax, jullie hebben ervoor gezorgd dat ik me geamuseerd heb, dat ik afgezien heb, dat ik vele kilometers op de fiets heb afgelegd, dat ik van alles geleerd heb, dat ik nieuwe plaatsen gezien heb. Jullie hebben gezorgd voor geniale stages en weekends voor ... teveel om op te noemen. Een welgemeende dank jullie wel hiervoor. Mijn doctoraat is dan wel voorbij, maar ik verwacht meer van het zelfde.

En mijn laatste en belangrijkste dankwoorden gaan naar mijn ouders, mijn broer Sander en mijn zus Liesbeth voor de steun en aanmoedigingen, voor het wild in het weekend, voor het uitlenen van de auto, voor het nalezen van mijn doctoraat, voor alle kleine en grote dingen, voor alles.

Gent, februari 2015
Thomas Cuyckens

Contents

Samenvatting

Vele fysische fenomenen kunnen gevat worden in enkele elegante vergelijkingen. Meestal wordt het pas ingewikkeld wanneer men probeert om die vergelijkingen op te lossen. Elektromagnetisme is zo een onderzoeksdomein waarin een eenvoudig stelsel van gekoppelde vectoriële differentiaalvergelijkingen in het algemeen analytisch onoplosbaar is. De wiskunde biedt gelukkig een andere aanpak om deze vergelijkingen op te lossen. Met behulp van numerieke technieken kunnen Maxwells vergelijkingen nauwkeurig genoeg opgelost worden om de fysieke werkelijkheid accuraat genoeg te beschrijven. In de laatste honderd jaar werden een aantal populaire numerieke methodes ontwikkeld, elk met hun eigen sterktes en zwaktes. Het doel van deze en vele andere onderzoeksinspanningen is om de algoritmische sterkte van (een van) deze methodes te verbeteren en de zwaktes ervan weg te werken.

Tegenwoordig worden alledaagse voorwerpen slimmer en slimmer. Het bekendste voorbeeld is de alomtegenwoordige smartphone. Ook slimme thermostaten, koelkasten en wasmachines krijgen meer en meer aandacht. Veel minder bekend zijn de intelligente antennesystemen, een belangrijk onderzoeksdomein voor INTEC's[2] elektromagnetisme groep. Deze intelligente antennesystemen worden gemaakt op nieuwe materialen zoals (geleidend) textiel, bevatten geïntegreerde elektronische circuits en kunnen hun stralingspatroon vervormen. Om deze eigenschappen te kunnen realiseren, worden kleine niet-lineaire elektronische componenten geïntegreerd naast grotere antennes. Zoals verderop zal worden uitgelegd, kan dit soort antennes zeer goed gesimuleerd worden met de Eindige-Differenties-in-het-Tijdsdomein methode (the Finite Difference Time Domain method (FDTD)). Tenminste als eerst een specifiek probleem wordt opgelost.

De FDTD methode, een numerieke methode geïntroduceerd door Kane Yee in 1966, heeft enkele voordelen bij het simuleren van geïntegreerde, ingewikkelde systemen. Ten eerste, FDTD is een expliciete methode. Dit betekent dat ze geen dure matrix inversie vereist. Dit maakt ze uitermate geschikt voor het simuleren van een groot aantal onbekenden. Daarenboven is FDTD zeer parallelliseerbaar. Dit resulteert in grote snelheidswinsten tijdens het simuleren. Ten tweede, FDTD opereert in het tijdsdomein. Dit betekent dat om niet lineaire karakteristieken te gebruiken in het lineaire frequentie domein, ze niet polynomiaal benaderd hoeven te worden. Ze kunnen dus direct in de methode geïncorporeerd worden. Langs de andere kant heeft standaard FDTD een groot nadeel. Het algoritme vereist dat er uniforme cellen gebruikt worden in het volledige rekendomein. Dit betekent dat de keuze van de celgrootte uiterst

[2] vakgroep Informatie Technologie, universiteit Gent

belangrijk is. Men probeert om kleine componenten accuraat te modelleren zonder het aantal cellen onnodig op te blazen. Als men, aan de ene kant, te kleine cellen kiest, zal de nauwkeurigheid van de simulatie groot zijn, maar wordt het aantal cellen onhandelbaar. Langs de andere kant, als men de celgrootte te groot kiest, zal men snel resultaten verkrijgen, die dan wel onnauwkeurig zijn. In deze thesis wordt een strategie voorgesteld om deze evenwichtsoefening te omzeilen. Als men de voorwaarde versoepelt om uniforme cellen te gebruiken, kunnen de celdimensies aangepast worden en kan men de specifieke geometrische vereisten van het systeem beter modelleren. De variabele celgrootte heeft als aanvullend voordeel dat het ook de grootte van benaderingsfouten kan verkleinen. Het voorgestelde 'arbitrair onderverdelen van roosters', bouwt op concepten uit de differentiaalmeetkunde en de eindige elementen methode (the Finite Element method (FE)). Uiteindelijk resulteert dit in een nieuw, verbeterd algoritme dat expliciet, stabiel en reciproque is. Het laat nauwkeuriger modelleren toe zonder last te hebben van een exploderend aantal roostercellen.

De techniek die ontwikkeld werd voor het verfijnen van cellen in FDTD werd uitgebreid zodat deze ook toepasbaar is op de Perfect Aangepaste Laag (Perfectly Matched Layer (PML)) begrenzing van het rooster. Sinds de ontwikkeling van de PML door Jean-Pierre Bérenger in 1996, werd het de de facto standaard om FDTD roosters te beëindigen. De reflecties veroorzaakt door PML's zijn vele ordes kleiner dan die veroorzaakt door concurrerende algoritmes. De kost voor het gebruiken van PML's ligt in het feit dat het rekendomein erdoor vergroot wordt en dat de update vergelijking ervan kostelijk is. Maar dit is slechts een lage prijs voor de betere performantie. Het verfijnen van PML-cellen maakt het enerzijds mogelijk om het rooster op elke plaats te begrenzen met een PML met exact dezelfde discretisatie als het rooster. Op die manier worden de geïntroduceerde fouten op de rooster/PML-interface tot een minimum beperkt. Anderzijds biedt het vergroven van PML-cellen de mogelijkheid om het aantal PML-cellen en dus het aantal dure update vergelijkingen te verminderen. Het algoritme kan dus gebruikt worden voor het verhogen van de nauwkeurigheid van de simulatie en voor het verminderen van de rekentijd.

Verschillende voorbeelden van celverfijning bij zowel gewone roosters als bij PML-roosters werden onderzocht. Daarbij werd gefocust op valse reflecties veroorzaakt door de roosterverfijning of door de PML's. Er werd opgemerkt dat celverfijning parallel aan de verfijningsinterface duidelijk meer reflecties veroorzaakt dan verfijning loodrecht op de interface. Dit resultaat kan doorgetrokken worden naar het verfijnen van PML-roosters. Het loodrecht vergroven van PML-cellen veroorzaakt slechts een fractie meer reflecties dan het gebruik van uniforme PML-cellen. Parallelle vergroving, introduceert veel meer reflecties. Deze resultaten werden gevalideerd door uitgebreide simulaties. Naast deze theoretische voorbeelden werd ook de karakteristieke impedantie van een differentieel striplijnpaar en een microstrip gesimuleerd. Dit om de nauwkeurigheid van de methode op een praktisch probleem te testen en om te bevestigen dat de nieuwe methode een wezenlijke versnelling van uitvoering en vermindering

van het benodigde geheugen kan bereiken.

In het tweede deel van deze thesis werd onderzoek gevoerd naar draadloze vermogenstransmissie (Wireless Power Transmission (WPT)) via ultra breedband (Ultra Wide Band (UWB)) antennes. Recentelijk heeft WPT weer aan interesse gewonnen met onder andere het draadloos opladen van smartphones. Het onderzoeksveld, bestaande uit verre veld en nabije veld WPT is eigenlijk veel ouder. Onderzoek naar nabije veld WPT wordt al uitgevoerd sinds men transformators is beginnen gebruiken. Verre veld WPT beleefde zijn glorie-jaren in de jaren *60* en *70*. Ruimtevaartorganisaties deden onderzoek naar het oogsten van zonne-energie in de ruimte en het neerstralen ervan naar de aarde en William Brown voorzag een op afstand bestuurbare modelhelikopter van vermogen door middel van microgolven. Vandaag worden meer praktische toepassingen beoogd. Verre veld WPT toepassingen omvatten het draadloos voeden van moeilijk te bereiken, gedistribueerde sensornetwerken, kabelvrije bureaus en (passieve) Radio Frequency IDentification (RFID) labels.

Vroeger werd verre veld WPT beschreven met behulp van de Friis transmissieformule. De relatie tussen verzonden en ontvangen vermogen verandert echter wanneer men gebruik maakt van UWB antennes of wanneer men in een multipad omgeving werkt. De nieuwe techniek die in deze thesis voorgesteld wordt, vertrekt van een raamwerk waarin alle bouwblokken (zender, kanaal en ontvanger), wiskundig van elkaar gescheiden worden zodat ze ad libitum uitgewisseld of vervangen kunnen worden. De gekozen aanpak vertrekt van een frequentieafhankelijke, amplitudegebaseerde beschrijving van de zender, de ontvanger en het vrije ruimte kanaal. In de volgende stap wordt het vrije ruimte kanaal vervangen door een kanaal in een multipad omgeving. De voorgestelde methode houdt rekening met de frequentieafhankelijkheid van alle betrokken grootheden en de frequentieafhankelijkheid van de transmissie- en reflectiecoëfficiënten van het kanaal. Nadat de transferfunctie van elke bouwsteen bepaald is, kan het complete probleem gesimuleerd worden door het correct combineren van de bouwblokken.

Om de methode te valideren werd de link tussen een UWB antenne op het menselijk lichaam en eenzelfde UWB antenne in een multipad omgeving onderzocht. Merk op dat het onmogelijk was om de volledige set-up te simuleren. Daarvoor was een te grote rekenkracht nodig. Het was ook niet mogelijk om de volledige configuratie na te bootsen in de anechoïsche kamer. Om een oplossing voor het probleem te bekomen, moest een slimme combinatie van metingen en simulaties gebruikt worden. In eerste instantie werd er een vrije ruimte referentieoplossing gesimuleerd op een korte, nog net simuleerbare afstand van 0.75 m. Daarna werd het kanaal vervangen door een kanaal van 5 m. Daarnaast werd ook een referentiemeting gedaan over een afstand van 5 m. Vervolgens werd deze antennelink gereconstrueerd door kanaalsimulaties en stralingspatroonmetingen en -simulaties te combineren. De gereconstrueerde oplossing werd veel sneller verkregen dan de referentieoplossing en sloot er ook goed bij aan. Daarna werd

een multipad, off-body antennelinkconfiguratie geconstrueerd door op gepaste wijze metingen en simulaties van een multipadkanaal en stralingspatronen van de antenne in de vrije ruimte en in de nabijheid van het menselijke lichaam te combineren. Uiteindelijk werd met behulp van de hierboven verkregen oplossing de ideale locatie bepaald waar men de meest optimale vermogensoverdracht heeft, rekening houdend met een groot aantal reflecties en het schaduweffect van het menselijk lichaam.

Summary

Lots of physical phenomena can be caught in a few elegant equations. Things become tougher, when one tries to solve those equations. Electromagnetism is such a research domain governed by a simple set of coupled vectorial differential equations that is analytically unsolvable in the general case. Fortunately, mathematics offers a different tool set to tackle these problems. Using numerical techniques, Maxwell's equations can be accurately approximated to obtain simulation results that describe physical observations at a more than acceptable level. A few popular numerical schemes have been developed in the last century, each with its strengths and weaknesses. The goal of this and many research efforts is to extend the algorithmic strengths and reduce the weaknesses of (one of) those methods.

Nowadays, everyday objects become smart, such as the ubiquitous smart phone, smart thermostats, one talks about smart refrigerators and washing machines, but less known are smart antenna systems, a major research field in the INTEC[3] electromagnetism group. These smart antenna systems come with integrated circuits, are built on novel materials such as (conductive) textiles and can perform radiation pattern shaping. To realize such features, very small, non-linear electronic components have to be integrated beside larger antennas. As will be explained shortly, these types of antennas are well-suited to be simulated using the Finite Difference Time Domain method (FDTD), if it wasn't for a minor issue that first should be mitigated.

FDTD, a numerical method introduced by Kane Yee in 1966, has some advantages to simulate these integrated, intricate systems. First, FDTD is very well suited to simulate a very large numbers of unknowns, because it is an explicit method. This means it does not need a costly matrix inversion. Moreover, FDTD is highly parallelizable, allowing for large speed-ups of the simulations. Second, FDTD operates in the time domain, meaning that non-linear characteristics do not have to be approximate polynomially to be used with the linear frequency domain. Therefore they can be included in a straightforward manner into the method. Conventional FDTD, however, has one major drawback. The algorithm requires uniform cells in the complete calculation domain. Therefore, the selection of the cell size is of paramount importance. One wants to model the small components accurately without unnecessary inflating the number of cells. On the one hand, selecting a too small cell size results in high accuracy but, an untractable amount of cells. On the other hand, selecting a too large cell size yields fast, but inaccurate results.

[3]Department of Information Technology, Ghent University

In this thesis, a mitigation strategy for this trade-off will be presented. By relaxing the uniform cell requirement, cell sizes can be varied to suit particular geometrical demands of the system to be modelled. An additional benefit of this adaptive cell size is the reduction of approximation errors (also known as staircasing errors). The presented 'arbitrary subgridding', builds on a framework with concepts from differential geometry and the Finite Element method (FE). Finally, this results in a novel, improved algorithm, that is explicit, stable and reciprocal. This allows for more accurate modelling using locally refined meshes without the unwanted explosion in the number of cells.

The strategy developed for the subgridding of FDTD meshes was also extended to the Perfectly Matched Layer (PML) termination of the grid. A PML is the de facto standard for FDTD mesh termination since its introduction in 1996 by Jean-Pierre Bérenger. PMLs exhibit reflections that are orders of magnitudes smaller than those caused by competing algorithms. The cost of PMLs lies in the enlargement of the calculation domain and the expensive update equation. But this is just a small price to pay for the improved performance. The subgridding of PMLs allows, on the one hand, for a PML with the exact same discretization as the grid it terminates. This reduces the errors at the mesh/PML interface. On the other hand, a subgridding strategy for PMLs opens up the possibility to reduce the number of expensive PML cells by unrefining the PML with respect to the mesh. The algorithm can thus be used for improving accuracy or for reducing calculation times.

Several subgridding examples of both standard meshes and PML meshes have been investigated, with a focus on spurious reflections caused by the subgridding and/or the PMLs. It has been observed that cell refinement parallel to the subgridding interface causes substantially more reflections than cell refinement normal to this interface. This result can be extended to PMLs. Tangentially unrefining the PML introduces little additional errors compared to a uniform PML, this contrary to normal unrefinement. This result has been verified by extensive simulations. Next to these rather theoretical examples, the characteristic impedance of the modes of a differential stripline pair and a microstrip have been simulated, to verify the accuracy of the method in a real life problem. They were also used to quantify the substantial speed-up factors and memory reductions that can be obtained using the novel algorithm.

In the second part of this thesis, Wireless Power Transmission (WPT) using Ultra Wide Band (UWB) antennas was researched. WPT attracted renewed attention with wireless charging of smart phones. However, the research field, consisting of near field and far field WPT, is much older. Near field WPT has been researched since the use of transformers. Far field WPT research peaked in the *'60*s and *'70*s. Space agencies conducted research into solar power harvesting, whose energy is beamed down to earth, and William Brown powered a remote model helicopter using microwaves. Nowadays more practical applications are aimed at. Far field WPT applications include the wireless

powering of hard to reach, distributed sensor networks, cable-free desks and (passive) Radio Frequency IDentification (RFID) tags.

Historically, far field WPT was described using the Friis transmission formula. However, this relation between transmitted and received power does not hold any longer when it concerns UWB antennas and multipath propagation. The novel technique presented in this thesis starts from a framework in which all building blocks (transmitter, channel and receiver), are mathematically separated, so building blocks can be taken out, swapped and/or replaced ad libitum. The taken approach starts from a frequency-dependent, amplitude-based description of the transmitter, the receiver and the free space channel. In a next step, the free space channel is replaced by a multi-reflection environment. The presented method takes into account the frequency dependency of all involved entities, as well as the frequency dependency of all reflection and transmission coefficients of the channel. After the transfer function of each building block is determined, the complete set-up can be simulated using the correct combination of blocks.

To validate the method, the transmitted power from a UWB antenna placed near the human body to an identical antenna in a multipath environment was studied. Note that it was impossible to entirely simulate the configuration under study due to the too large computational domain needed. Neither was it possible to exactly recreate the set-up in the anechoic chamber. In order to obtain a solution for the configuration, a smart combination of measurements and simulation data was used. First a reference solution in free space was created, by simulating an antenna link over a distance of 0.75 m, which could still be simulated. Next the channel was replaced by a free space channel of 5 m. Additionally, a reference measurement was done by measuring the free space antenna link over a distance of 5 m. Next this antenna link was reconstructed by combining channel simulations and radiation pattern measurements and simulations. It was found that the reconstructed solution was obtained much faster than the reference solution. Moreover, it was in good agreement with the reference solution. Then, a multipath, off-body antenna link configuration was constructed by carefully combining measurement and simulation results of the multipath channel, the on-body and free space radiation pattern. Finally, using the solution above, the location for optimal power transmission in the multipath environment was quickly determined, taking into account a multitude of reflections and shadowing by the human body.

List of Abbreviations

BAN	Body Area Network
BOR-FDTD	Body of Revolution FDTD
CFL	Courant-Friedrichs-Lewy
CFS-PML	Complex Frequency Shifted Perfectly Matched Layer
CPML	Convolution Perfectly Matched Layer
CST-MWS®	Computer Simulation Technology's Microwave Studio®
DBC	Dirichlet Boundary Condition
DFT	Discrete Fourier Transform
EMPro®	Keysight Technology's EMPro 3D EM Simulation Software®
FCC	Federal Communications Commission
FD	frequency domain
FDTD	the Finite Difference Time Domain method
FE	the Finite Element method
GP	Gaussian pulse
INTEC	Department of Information Technology
IP	intellectual property
MoM	the Method of Moments
PEC	Perfect Electric Conductor
PL	path loss
PML	Perfectly Matched Layer
RFID	Radio Frequency IDentification
SAR	Specific Absorption Rate
TD	time domain
UPML	Uniaxial Perfectly Matched Layer
UWB	Ultra Wide Band
WPT	Wireless Power Transmission

List of Symbols

Mathematical symbols

$\lvert\cdot\rvert$	the magnitude of a (complex) number
$\cdot^*$	the complex conjugate
d	depending on the context this is (1) a regular derivative, noted as $\mathrm{d}_\alpha\beta(\alpha)$, meaning the derivative of β with respect to α, (2) the exterior derivative in a differential geometry context as a unified notation for the gradient, the curl as well as the divergence or (3) the distance between a receive and a transmit antenna.
$\circ$	the vector inner product, also denoted as $<\cdot,\cdot>$
$\star$	the Hodge star operator
$\Im$	the imaginary part of a complex number
$\jmath$	the imaginary unit, with $\jmath^2 = -1$
∇	the nabla operator, with ∇x, $\nabla \times \boldsymbol{x}$ and $\nabla \circ \boldsymbol{x}$ the gradient, curl and divergence, respectively
∂	depending on the context, this is (1) a regular partial derivative, noted as $\partial_\alpha\gamma(\alpha,\beta)$ meaning the partial derivative of γ with respect to α or (2) the boundary operator in a differential geometry context
$\Re$	the real part of a complex number
$\overline{\overline{\boldsymbol{X}}}$	a matrix or tensor X
$\cdot^T$	the transpose of a vector (or matrix)
$\boldsymbol{x}$	a vector x
$\wedge$	the wedge product or exterior product

Electromagnetic symbols

$\boldsymbol{B}$	magnetic flux density [T]
c	the speed of light in a vacuum, $c = 299\,792\,458\,\mathrm{m/s}$

$\boldsymbol{D}$	electric displacement field or electric flux density [C/m^2]
$\boldsymbol{E}$	electric field strength [V/m]
ε	the permittivity of a medium, it is the product of the relative permittivity ε_r and the permittivity of free space $\varepsilon_0 = \left(c^2\mu_0\right)^{-1} = 8.854 \times 10^{-12}$ F/m
f	frequency [Hz]
$\boldsymbol{H}$	magnetic field strength [A/m]
η	impedance of free space, if accompanied by a subscript, it indicates the impedance of another medium
$\boldsymbol{j}$	electric current density [A/m^2]
k	wavenumber, $2\pi/\lambda$ [rad/m]
λ	wavelength [m]
μ	the permeability of a medium, it is the product of the relative permeability μ_r and the permeability of free space $\mu_0 = 4\pi \cdot 10^{-7} = 1.256 \times 10^{-6}$ H/m
R_A	$\Re Z_A$, the real part of the impedance related to entity A
ρ	electric charge density [C/m^3]
t	time [s], Δt indicates a change in time, a time step
τ	ct [m], speed of light multiplied by the time variable, $\Delta\tau$ indicates a change in τ
Z_A	impedance related to entity A

Symbols specific to FDTD (part I)

$\overline{\overline{\boldsymbol{A}}}_k$	restriction matrix of order k
$\overline{\overline{\boldsymbol{C}}}$	or $\overline{\overline{\boldsymbol{C}}}_1$, the discrete curl matrix, if accompanied by another subscript, it is the discrete representation of the exterior derivative. In a differential geometry context, it is denoted by C or C_1
$\overline{\overline{\boldsymbol{\Lambda}}}$	UPML stretching matrix
$s(\alpha, \sigma, \kappa)$	the PML stretching function, consisting of three functions α, κ and σ, all dependent on the distance to the PML/grid interface
up_B	the update equation of an B-field

up_E	the update equation of an E-field
$\boldsymbol{W}_k$	Whitney form of order k

Symbols specific to UWB (part II)

CH	the channel between transmitter and receiver
Δd	the path length difference
$D(\theta, \phi)$	the directivity of an antenna
ϵ	the radiation efficiency of an antenna
$\boldsymbol{F}(\theta, \phi)$	the far field radiation vector of an antenna
$G(\theta, \phi)$	the gain of an antenna
$\overline{\overline{\boldsymbol{\Gamma}}}$	a full tensor containing the product of an ordered series of transmission and reflection coefficients
$\boldsymbol{H}$	transfer function of an antenna, channel, ...
M	the antenna mismatch factor
PL	path loss, in free space the path loss equals $\left(\frac{4\pi df}{c}\right)^2$
Q_{RT}	the polarisation mismatch factor
$\overline{\overline{\boldsymbol{R}}}$	a full tensor reflection coefficient
RX	receiver/receive antenna
$\overline{\overline{\boldsymbol{T}}}$	a full tensor transmission coefficient
TX	transmitter/transmit antenna
V_o	the open circuit voltage

List of Publications

Articles in International Journals

- T. Cuyckens, H. Rogier, and D. De Zutter, "Numerical assessment of the combination of subgridding and the perfectly matched layer grid termination in the finite difference time domain method", *International Journal of Numerical Modelling: Electronic Networks, Devices and Fields*, vol. 27, no. 3, pp. 527–543, 2014, issn: 1099-1204. [Online]. Available: http://dx.doi.org/10.1002/jnm.1932.

Articles in Conference Proceedings

- T. Cuyckens, H. Rogier, and D. De Zutter, "Numerical assessment of the combination of subgridding and PML grid termination in FDTD", in *9th International Symposium on Electric and Magnetic Fields*, 2013.

Articles submitted to International Journals

- T. Cuyckens and H. Rogier, "Framework for the simulation of Wireless Power Transfer over Ultra Wide Band links in intricate propagation environments", *International Journal of Numerical Modelling: Electronic Networks, Devices and Fields*, 2014.

Electromagnetic Modelling of Wideband Wired and Wireless Interconnections

Introduction

Electromagnetic radiation is ubiquitous. With wavelengths ranging from picometres (gamma-rays) to 100 000 kilometres (Extremely Low Frequency), it is a research field that spans many radiation types with very diverse properties. In practice, this results in applications ranging from the Fermi Gamma-ray Space Telescope to Very Low Frequency submarine communications, but also the omnipresent smart phone, X-ray imaging, light bulbs and leds, lasers and microwave ovens. Nevertheless, their operation can be described by a simple set of equations, known as Maxwell's equations.

1 Maxwell's equations

The single largest milestone in the scientific field of electromagnetism is the work of James Maxwell (1831–1879), a Scottish mathematical physicist. He published a set of ground breaking publications on the unification of electricity, magnetism and optics (also referred to as the 'second great unification in physics', the first being the work of Sir Isaac Newton).

In a first important tetralogy of papers, 'On Physical Lines of force' [1] (1861), Maxwell built on the theoretical work of Michael Faraday and the experiments of Wilhelm Weber and Rudolf Kohlrausch to derive his famous set of equations (although as part of larger set of twenty equations). In his publication 'A Dynamical Theory of the Electromagnetic Field' [2] (1865) he also derived the wave equation from his previously presented equations, thereby showing that electromagnetic waves travel at the speed of light. Maxwell's equations as we know them and as given by (1) below, were written down by Oliver Heaviside in 1884.

$$\nabla \times \boldsymbol{E}(\boldsymbol{r},t) = -\partial_t \boldsymbol{B}(\boldsymbol{r},t) \tag{1a}$$

$$\nabla \times \boldsymbol{H}(\boldsymbol{r},t) = \partial_t \boldsymbol{D}(\boldsymbol{r},t) \tag{1b}$$

$$\nabla \circ \boldsymbol{B}(\boldsymbol{r},t) = 0 \tag{1c}$$

$$\nabla \circ \boldsymbol{D}(\boldsymbol{r},t) = \rho(\boldsymbol{r},t) \tag{1d}$$

$\boldsymbol{B}$, $\boldsymbol{D}$, $\boldsymbol{H}$ and $\boldsymbol{E}$ are vector quantities representing the magnetic and electric flux density and the magnetic end electric field strength, respectively, ρ is the electric charge density, t is the time variable and $\boldsymbol{r}$ is the location vector. The time and location dependence of all involved quantities will most often be suppressed.

These equations are often complemented by what is known as the constitutive equations (2), which formulate a relation between B and H-fields and between

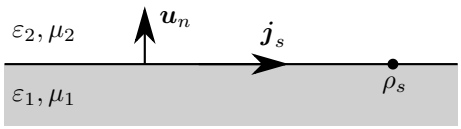

Figure 1: Interface between two media characterized by ε_1, μ_1 and ε_2, μ_2, respectively. On the interface surface currents $\boldsymbol{j}_s$ and surface charges ρ_s may exist. The electric and magnetic fields have to obey the boundary conditions as stated in (3).

D and E-fields.

$$\boldsymbol{B}(\boldsymbol{r}) = \mu \boldsymbol{H}(\boldsymbol{r}) \tag{2a}$$
$$\boldsymbol{D}(\boldsymbol{r}) = \varepsilon \boldsymbol{E}(\boldsymbol{r}) \tag{2b}$$

with $\mu = \mu_r \mu_0$, the permeability of the material as the product of the relative permeability (μ_r) and the permeability of free space ($\mu_0 = 4\pi \times 10^{-7}\,\mathrm{H/m}$) and $\varepsilon = \varepsilon_r \varepsilon_0$, the permittivity of the material as the product of the relative permittivity (μ_r) and the permittivity of free space ($\varepsilon_0 \approx 8.8542 \times 10^{-7}\,\mathrm{F/m}$). The differential formulation, presented in (1), tacitly assumes that on the interface between two media, illustrated by Fig. 1 some boundary conditions are met. More specifically

$$\boldsymbol{u}_n \times (\boldsymbol{E}_1 - \boldsymbol{E}_2) = 0 \tag{3a}$$
$$\boldsymbol{u}_n \times (\boldsymbol{H}_1 - \boldsymbol{H}_2) = \boldsymbol{j}_s \tag{3b}$$
$$\boldsymbol{u}_n \circ (\boldsymbol{D}_1 - \boldsymbol{D}_2) = \rho_s \tag{3c}$$
$$\boldsymbol{u}_n \circ (\boldsymbol{B}_1 - \boldsymbol{B}_2) = 0 \tag{3d}$$

where $\boldsymbol{j}_s$ and ρ_s are the surface current density and the surface charge density, respectively.

Throughout the years, a lot of new formulations have been presented. Notable is the formulation using the differential geometry framework, as briefly introduced in chapter 2. Throughout this dissertation two different formulations will be used. In part I, a normalized version of Maxwell's equations will be used, as opposed to part II, where the above presented formulation is used. The normalization will be clearly expressed at the appropriate time. The physical quantities together with their units, found in the 'List of Symbols', refer to unnormalized physical quantities. Their normalized versions are not included in that list. On the more practical side, Maxwell's equations are too complex to solve analytically in a straightforward way. Therefore, some numerical approach is used to approximate the exact solution as close as possible. Three major approaches exist, the Finite Difference Time Domain method (FDTD), the Finite Element method (FE) and the Method of Moments (MoM). Neither of them is generally better than the others. The method of choice is largely dependent on

the type of problem one wants to solve (and secondary on the available software). These all-purpose solutions perform well, but are usually expensive in terms of time, resources, and more literally in the purchase of hardware and software. It needs no saying that plenty of specialist applications have been developed that are only useful for specific problems. These applications reduce costs by making thoughtful assumptions and simplifications to the interpretation of Maxwell's equations. This second type of applications, although less generally applicable, will provide (almost) equally accurate results at a fraction of the cost (regarding time and resources). Trying to get the best of both worlds, hybrid methods, combining both approaches, are developed as well. A very specific example is the use of the Friis transmission formula [3] to calculate the power received at one end of an antenna link given the antenna characteristics, the free space channel and the power transmitted at the other end. This quantity can be perfectly calculated using Maxwell's coupled vectorial differential equations, but a much faster accurate solution is obtained by the above mentioned formula.

2 Outline

This thesis consists of two major parts. The first part is dedicated to enhancements of the FDTD method. The first chapter provides an introduction to the mathematical concepts of finite differences and applies them to Maxwell's equations, in order to derive the conventional FDTD scheme. Some insights into to the stability of the method and the dispersion errors introduced by it, are given. The second chapter provides a concise introduction to differential geometry, because the subgridding of FDTD can be very elegantly expressed in this formalism. In the third chapter, an extended subgridding technique is presented. This technique allows for the use of non-uniform cells. A separate section is dedicated to the influence of these mesh irregularities on the excitation of spurious reflections. Additionally, the subgridding is extended towards Perfectly Matched Layers (PMLs) and again the excitation of spurious reflections is investigated. Although theoretically possible, subgridded PML corner regions are not extensively researched. Subgridding corner regions must be carried out with great care, in order not to suffer from too large spurious reflections. Finally this chapter concludes with the simulation of a microstrip and a differential stripline pair to verify the accuracy of the method as well as to quantify the time and memory gains that can be achieved.

The second part starts with an introductory chapter on antenna characteristics, Ultra Wide Band terminology and the Friis transmission formula, the most important formula in far field Wireless Power Transmission (WPT). The second chapter in this part, extends the previously introduced concepts towards WPT over Ultra Wide Band (UWB) antenna links, taking into account shadowing by the human body and multipath propagation. In this chapter, far field WPT is numerically evaluated for these environments, while introducing a framework that performs these calculations on a modular basis. The framework

allows the use of datasets obtained from various sources, such as measurements, simulations and/or models. This chapter concludes with the calculation of the most interesting position for receiving wireless power in a free space and a multipath environment.

A final chapter in this thesis highlights possible extensions to the presented work and plausible future research paths.

References

[1] J. C. Maxwell, "On Physical Lines of Force", *The London, Edinburgh, and Dublin Philosophical Magazine and Journal of Science*, vol. 21, no. 4, pp. 161–175, 281–291, 338–348, 1861.

[2] J. C. Maxwell, "A Dynamical Theory of the Electromagnetic Field", *Philosophical Transactions of the Royal Society of London*, vol. 155, pp. 459–512, 1865. [Online]. Available: `http://rstl.royalsocietypublishing.org/content/155/459.short`.

[3] H. Friis, "A Note on a Simple Transmission Formula", *Proceedings of the IRE*, vol. 34, no. 5, pp. 254–256, May 1946, issn: 0096-8390.

Part I

Arbitrary subgridding in the Finite Difference Time Domain method

The Finite Difference Time Domain method is one of the major mathematical techniques to simulate full wave electromagnetic problems. Since it has been introduced in 1966 by Kane Yee, the number of contributions related to this topic has been increasing year by year. It's straightforwardness, explicitness and the fact that it's easily parallelizable, made it a popular choice in many research fields including electromagnetism. Unfortunately, the mandatory use of uniform cells has been an impediment on its expanding use. The presented contribution to the vast literature on the Finite Difference Time Domain method removes the stringent requirement on cell dimensions by allowing very general, almost arbitrary subgridding of mesh cells, thereby opening up the use of the Finite Difference Time Domain method to whole new problem sets.

1

Introduction to the Finite Difference Time Domain method

★ ★ ★

The Finite Difference Time Domain method is an algorithm used to accurately discretize differential equations. Within the field of electromagnetism it is an often used algorithm for full wave simulation. Unsurprisingly, it is part of renown software suites as Computer Simulation Technology's Microwave Studio® and Keysight Technology's EMPro 3D EM Simulation Software®. Its straightforward mathematical principles are most easily explained using a vector calculus notation. In this chapter an introduction to all necessary concepts will be provided as well as to the interpretation of Maxwell's equation within this framework. Furthermore a summary listing of the important properties of the Finite Difference Time Domain method will be discussed.

1.1 Introduction

Maxwell's equations, as presented in section 1 of the introductory chapter, are a set of coupled differential equations. In general they cannot be solved analytically, not by a simple computer nor by a computing cluster, let alone by pen and paper. The remaining approach is to numerically approximate this set of very intricate equations. If the approximation is fine enough, and consequently the introduced errors are small and/or negligible, the supplied solution will be a good enough representation of the reality.

Three major techniques exist to approximate Maxwell's equations: the Finite Element method (FE), the Method of Moments (MoM) and the Finite Difference Time Domain method (FDTD). All these techniques exist in many a colour and flavour, and they all have specific problem types they solve best. Nevertheless, these techniques are all suited to solve full wave 3D electromagnetic problems and are part of many commercial software packages.

FDTD, the method of choice in this thesis, is a numerical method first described by Kane Yee in 1966 [1]. Contrary to its competitors, FDTD is exceptionally well suited to simulate very large structures because the method does not involve taking the inverse of a (large) matrix (which scales badly with increasing matrix size). This lack of a matrix inversion, together with the relative independence of the mesh cells, allows for massively parallelization of the FDTD calculations. This is another reason to use this method for the simulation of large problems. A third major advantage of FDTD is that it runs in the time domain (TD). This means that it does not rely on the linear Fourier transform and, therefore, can simulate non-linear devices without making linear approximations.

On the downside, FDTD uses a uniform mesh of cuboidal cells. This does not allow for the accurate modelling of structures that are not aligned with the mesh, such as cylinders and other curved objects. Attempting to simulate such ill-suited structures results in so called staircasing errors. To reduce this type of error, the cell size has to be reduced at the cost of an exploding number of cells (the number of cells scales with $\mathcal{O}(N^3)$ with respect to the 1D cell size). Another consequence of the obligatory use of uniform cells is the conflict introduced when simulating electrically small devices in large domains. In order to achieve a certain accuracy, the mesh cells have to be adequately small to accurately model the small devices. On the other hand, to limit the computation time and the computational resources, the number of cells needed to fill the large domain has to be kept to a minimum. Hence, the trade-off between larger and smaller cells. Additionally, if a mesh cell's dimension is scaled down by a factor two, so is the time step. Therefore, the computation time scales with $\mathcal{O}(N^4)$ relative to the 1D cell dimension.

Most of the scaling problems can be handled by introducing arbitrary subgridding into the method. Not only does this reduce the number of cells significantly when simulating small devices in large domains, it also allows for using optimized cells that best approximate the elements to be modelled. This arbitrary subgridding will be subject of the research in this thesis and will be tackled in chapter 3.

FDTD as presented by Yee builds upon some mathematical techniques, which will be introduced shortly. These techniques will then be applied to Maxwell's equations.

1.2 Normalized Maxwell's curl equations

In this part of this dissertation, a normalized version of Maxwell's equation is used. To do so, we introduce

$$\hat{E} = \sqrt{\varepsilon_0} E \qquad \hat{D} = (\sqrt{\varepsilon_0})^{-1} D \tag{1.1a}$$

$$\hat{H} = \sqrt{\mu_0} H \qquad \hat{B} = (\sqrt{\mu_0})^{-1} B \tag{1.1b}$$

resulting in altered constitutive relations, given below

$$\hat{D} = \varepsilon_r \hat{E} \tag{1.2a}$$

$$\hat{B} = \mu_r \hat{H} \tag{1.2b}$$

Consequently, Maxwell's curl equations can be rewritten as

$$-\partial_t \hat{B} = \frac{1}{c} \nabla \times \hat{E} \tag{1.3a}$$

$$\partial_t \hat{D} = \frac{1}{c} \nabla \times \hat{H} \tag{1.3b}$$

with $c = \left(\sqrt{\varepsilon_0 \mu_0}\right)^{-1}$ the speed of light in free space. Now, replace the partial time derivative with a partial derivative with respect to $\tau = ct$, to obtain

$$-\partial_\tau \hat{B} = \nabla \times \hat{E} \tag{1.4a}$$

$$\partial_\tau \hat{E} = \frac{1}{\varepsilon_r \mu_r} \nabla \times \hat{B} \ , \tag{1.4b}$$

the normalized version of Maxwell's curl equations as used throughout part I. From here on the hat will be dropped from the notation.

1.3 Finite differences

In order to numerically simulate the continuous Maxwell equations, they have to be discretized. FDTD outlines a procedure to do exactly this. First, the computational domain is divided into cuboids. The (discrete) samples of the E and B-fields are positioned on the edges and the faces of the cuboids, respectively. Next, one has to define a discrete variant of the curl that can operate on the discrete field samples. Finally, E and B-fields are updated on (distinct) time instances alternately, until an external stop condition is met.

1.3.1 Central differencing

The continuous curl $(\nabla \times \cdot)$ is constructed from a set of partial spatial derivatives. Each derivative $(\mathrm{d}y(x)/\,\mathrm{d}x)$ is approximated by taking the relative difference between two points, $\Delta y / 2\Delta x$, as illustrated by Fig. 1.1. The discrete derivative

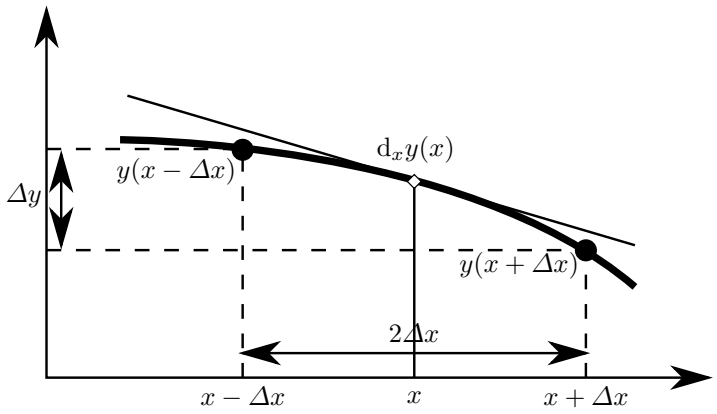

Figure 1.1: central differencing approximation of the derivative $\mathrm{d}_x y(x)$, by taking the ratio $\Delta y/2\Delta x$ (see (1.7)

is located at the midpoint of the two points. A more rigorous definition and derivation is given below.

Starting from a second order Taylor series expansion of the continuous function y at location $x + \Delta x$ and $x - \Delta x$ with corresponding errors term ϵ^+ and ϵ^- as given by

$$y(x + \Delta x) = y(x) + \mathrm{d}_x y(x) \cdot \Delta x + 0.5\, \mathrm{d}_{xx} y(x) \cdot (\Delta x)^2 + \epsilon^+ \tag{1.5a}$$

$$y(x - \Delta x) = y(x) - \mathrm{d}_x y(x) \cdot \Delta x + 0.5\, \mathrm{d}_{xx} y(x) \cdot (\Delta x)^2 + \epsilon^- \tag{1.5b}$$

and after subtracting the second equation from the first, this results in

$$y(x + \Delta x) - y(x - \Delta x) = 2\, \mathrm{d}_x y(x) \cdot \Delta x + \epsilon^+ - \epsilon^- \tag{1.6}$$

Rearranging the terms and discarding the error terms yields the discrete central differencing approximation of the continuous derivative.

$$\mathrm{d}_x y(x) = \frac{y(x + \Delta x) - y(x - \Delta x)}{2\Delta x} = \frac{\Delta y}{2\Delta x} \tag{1.7}$$

Typically, this last equation is applied with $\Delta x/2$ instead of Δx. This means that the derivative calculated from sample points at locations $i\Delta x$ and $(i + 1)\Delta x$ is located in between at location $(i + 0.5)\Delta x$. Following the popular choice of collocating the E-fields with the edges of the cuboidal mesh, implies, because of the use of central differencing, that the B-fields are located at the centre of the faces of the cuboidal mesh. This means that E and B-fields are always separated by half a cell as is illustrated by Fig. 1.2. Note also that in (1.6) the second order derivative has disappeared. Therefore this technique is second order accurate. Now, this knowledge will be applied to Maxwell's curl equations,

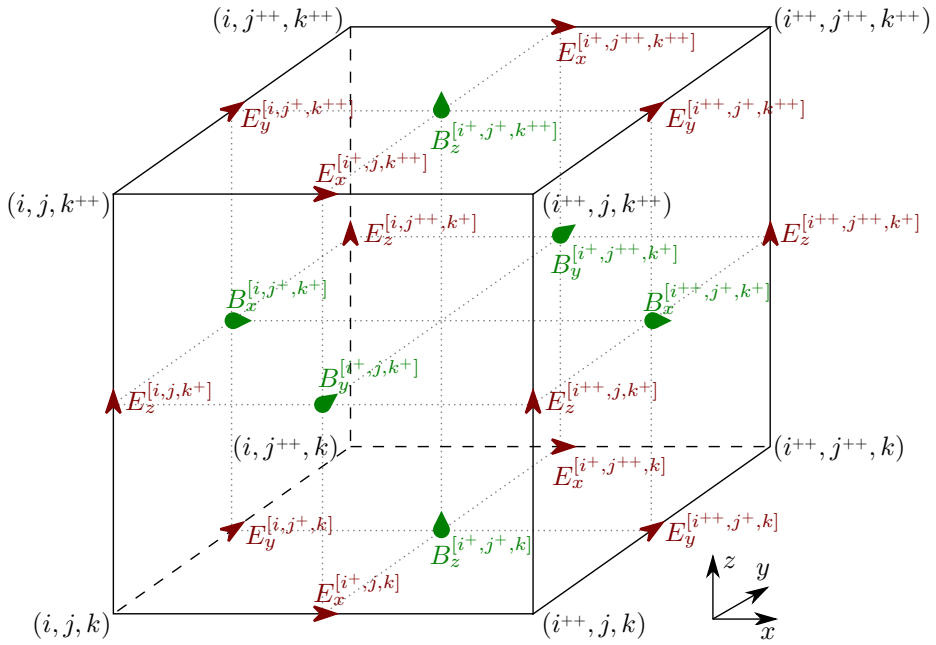

Figure 1.2: a standard Yee cell, with indicated positions of the nodes, E-fields (red) on the edges and B-fields (green) on the faces. Abstraction is made of the cell dimensions and superscript $^+$ indicates an increase of the corresponding index with 0.5. Thus $[i^+, j, k^{++}]$ is the concise form of $[(i+0.5)\Delta x, j\Delta y, (k+1)\Delta z]$.

repeated below for convenience,

$$-\partial_\tau \boldsymbol{B}(\boldsymbol{r},t) = \nabla \times \boldsymbol{E}(\boldsymbol{r},t) \tag{1.8a}$$

$$\partial_\tau \boldsymbol{E}(\boldsymbol{r},t) = \frac{1}{\varepsilon_r \mu_r} \nabla \times \boldsymbol{B}(\boldsymbol{r},t) \tag{1.8b}$$

with $\tau = ct$, the product of the speed of light and the time variable t, and ε_r and μ_r the relative permittivity and the relative permeability of the background medium, respectively. Remember, although τ represents a distance rather than a time variable, it will often be referred to as a time variable since it replaces 't' and people are used to a time derivative in Maxwell's equation.

Next, central differencing is applied to the x-component of both the E and B-fields

$$-\partial_\tau B_x^{[ij^+k^+]} = \left(\frac{E_z^{[ij^{++}k^+]} - E_z^{[ijk^+]}}{\Delta y} - \frac{E_y^{[ij^+k^{++}]} - E_y^{[ij^+k]}}{\Delta z} \right) \tag{1.9a}$$

$$\partial_\tau E_x^{[i^+jk]} = \frac{1}{\varepsilon_r \mu_r} \left(\frac{B_z^{[i^+j^+k]} - B_z^{[i^+j^-k]}}{\Delta y} - \frac{B_y^{[i^+jk^+]} - B_y^{[i^+jk^-]}}{\Delta z} \right) \tag{1.9b}$$

The location indices of the E and B-fields are counted as multiples of Δx, Δy and Δz. The superscript $^+$ is used to indicate a shift with 0.5, thus i^+ is short hand for $(i+0.5)\Delta x$ and j^{++} is short hand for $(j+1)\Delta y$. Analogously, a superscript $^-$ is used for a shift with -0.5. One can clearly see that the update of an E-field requires the value of its four neighbouring B-fields and vice versa.

The equations in (1.9) are called semi-discrete, because only the spatial component is discretized, while the temporal component remains continuous. The expressions for the i^{th}-component of the curl (between large brackets in (1.9)) above will often be written as $(\nabla \times \boldsymbol{E})_i$ and $(\nabla \times \boldsymbol{B})_i$, allowing for a much compacter notation. At the same time the spatial indices for the τ-derivative are also suppressed.

1.3.2 Leapfrogging

To discretize the partial time derivative, an approach similar to the one in (1.7) is used, as illustrated below.

$$\partial_\tau f(\tau) \approx \frac{f(n^{++}) - f(n)}{\Delta\tau} \tag{1.10}$$

The use of central differencing, implies that the derivative is located at time instance n^+. (1.10) can be used to calculate the field value at time instance n^{++}, when it is rearranged as follows

$$f(n^{++}) = f(n) + \Delta\tau\left(\partial_\tau^{n^+} f(\tau)\right) \tag{1.11}$$

Although the update equation was derived using central differencing, leapfrogging itself is a numerical integration method, where a future value is calculated from past values. The major advantages of leapfrogging are 'time-reversibility' (this allowed for the derivation of the method using central differencing) and its 'symplectic' nature (implying the energy [1] conservation of the system [2], [3]). Note that the continuous τ-derivative is on the right-hand side of the equation. It is needed to calculate future values of $f(n)$. This value will be obtained from the semi-discrete Maxwell's equations, which feature the exact same continuous τ-derivative.

1.4 Fully discrete Maxwell's equations

Applying leapfrogging to the semi-discrete Maxwell's equations is done, as mentioned before, by plugging the τ-derivative from (1.9) into the right hand side of (1.11). This results in

[1] FDTD preserves a modified definition of the energy $^1/_2\left(\boldsymbol{E}(n^+) \circ \boldsymbol{D}\left(n^-\right) + \boldsymbol{H}(n) \circ \boldsymbol{B}(n)\right)$ rather than $^1/_2\left(\boldsymbol{E}(n) \circ \boldsymbol{D}(n) + \boldsymbol{H}(n) \circ \boldsymbol{B}(n)\right)$, all taken at time instance n, which oscillates around a stationary value.

$$\boldsymbol{E}(n^{++}) = \boldsymbol{E}(n) + \underbrace{(\mu_r \varepsilon_r)^{-1} \Delta\tau(\nabla \times \boldsymbol{B}(n^{+}))}_{\mathrm{up}_E} \tag{1.12a}$$

$$\boldsymbol{B}(n^{+}) = \boldsymbol{B}(n^{-}) - \underbrace{\Delta\tau(\nabla \times \boldsymbol{E}(n))}_{\mathrm{up}_B} \tag{1.12b}$$

where the expansion of the curl in its components has been shortened to its symbolic notation. The terms up_E and up_B refer to the amount added to the previous field value. up_E and up_B will recur later on and are given a name for future convenience.

As can be seen from the equations above, not only are the E and B-fields not collocated in space they are also not sampled at the same time instance. This observation leads to an update scheme that operates as follows:

```
int main = 0 {
  double* fieldsE = new double[nrEfields];
  double* fieldsB = new double[nrBfields];
  double n = 0.0;
  bool stopCondition = false;

  initFields(fieldsE,distributionE);
  initFields(fieldsB,distributionB);

  while(!stopCondition) {
    // update E-fields
    for (int i = 0; i < nrEfields; i++) {
      fieldsE[i] += updateE(i,n,fieldsB);
    }
    n += 0.5;

    // update B-fields
    for (int i = 0; i < nrBfields; i++) {
      fieldsB[i] += updateB(i,n,fieldsE);
    }
    n += 0.5;

    stopCondition = evalStopCond(n,fieldsE,fieldsB);
  }
  exit 0;
}
```

Stability

The stability of the whole algorithm depends on the choice of $\Delta\tau$. Following the stability analysis of [4], $\Delta\tau$ has to be chosen as follows

$$\Delta\tau \leq \left(\sqrt{(\Delta x)^{-2} + (\Delta y)^{-2} + (\Delta z)^{-2}}\right)^{-1}$$

This is also known as the 'Courant-Friedrichs-Lewy'-limit or shorter the Courant-limit or even the CFL-limit. For cubical cells of size Δ this simplifies to $\Delta\tau \leq \Delta/\sqrt{3}$.

Grid dispersion

Consider a point source in a two dimensional grid at a certain location $E_z^{[x,y]}$ generating a Dirac pulse at time instance $n = 0$. One time step later, the field points at $E_z^{[x^{--},y]}$, $E_z^{[x^{++},y]}$, $E_z^{[x,y^{--}]}$ and $E_z^{[x,y^{++}]}$ are reached by the travelling wave and their field values are thus different from 0. Advancing one more time step, not only the field points $E_z^{[x-2,y]}$, $E_z^{[x+2,y]}$, $E_z^{[x,y-2]}$ and $E_z^{[x,y+2]}$ will be excited, but also the field points at $E_z^{[x^{--},y^{--}]}$, $E_z^{[x^{++},y^{--}]}$, $E_z^{[x^{--},y^{++}]}$ and $E_z^{[x^{++},y^{++}]}$. Physically, a circular wave front is expected, but numerically the wave front is diamond shaped. This means that in FDTD, the numerical wave does not propagate at the same pace in every direction. Mathematically, this is described as follows [4].

Construct a composite quantity $\boldsymbol{F} = \boldsymbol{B} + \jmath\boldsymbol{E}$. Maxwell's curl equations can be condensed to

$$\jmath\nabla \times \boldsymbol{F} = \partial_\tau \boldsymbol{F} \tag{1.13}$$

Substitute for $\boldsymbol{F}$ the travelling wave expression

$$F^{[x,y,z]}(n) = F_0 \mathrm{e}^{-\jmath(xk_x\Delta x + yk_y\Delta y + zk_z\Delta z)} \mathrm{e}^{\jmath kn\Delta\tau} \tag{1.14}$$

and apply the space and time discretization of (1.13), as discussed before. Solve the obtained equation system as outlined in [4]. This results in the dispersion relation

$$\left(\frac{1}{\Delta\tau}\sin\frac{\pi\Delta\tau}{\lambda}\right)^2 = \sum_{i\in\{x,y,z\}}\left(\frac{1}{\Delta i}\sin\frac{k_i\Delta i}{2}\right)^2, \tag{1.15}$$

which simplifies to

$$\left(\frac{1}{\alpha}\sin\frac{\pi\alpha}{N}\right)^2 = \sum_{i\in\{x,y,z\}}\left(\sin\frac{k_i\Delta i}{2}\right)^2 \tag{1.16}$$

for a cubical mesh with $\Delta = \Delta x = \Delta y = \Delta z$, $\Delta\tau = \alpha\Delta/\sqrt{3}$, with α a fraction of the CFL and N the mesh density in number of cells per wavelength.

(1.16) shows that the dispersion relation is dependent on both the propagation direction of the wave and the sampling density of the mesh, through $k_i(\theta, \phi)$ and $\sin \frac{\pi\alpha}{N}$. Ideally, physically, the dispersion relation looks like

$$\left(\frac{2\pi f}{c}\right)^2 = \sum_i (k_i)^2 \qquad i \in \{x, y, z\} \tag{1.17}$$

One can prove that (1.16) equals (1.17) for a wave propagating along the diagonal of a cubical mesh, if $\alpha = 1$, or equivalently $\Delta\tau = \Delta/\sqrt{3}$.

Important to note is that dispersion related errors are cumulative. Meaning that, the further a wave travels the larger the error becomes. For very large computation domains, one has to verify that the dispersion induced errors do not exceed an acceptable threshold.

To reduce dispersion errors [4], one can use higher order spatial derivatives, calculate the spatial derivatives using the Discrete Fourier Transform (DFT), use hexagonal grids, use more cells per wavelength or decrease α to a smaller fraction of the CFL. The use of subgridding, as will be explored in chapter 3, will locally reduce dispersion errors by locally increasing the mesh density, as was shown in [5].

1.5 Perfectly Matched Layer

As is clear now, FDTD works by alternately updating all E and B-fields in the computational domain. However, at the borders some anomalies occur. An E-field at the edge of the mesh misses (at least) one B-field neighbour to be properly updated. Assuming the missing B-field is zero, actually imposes a Dirichlet Boundary Condition on the computational domain. If one, however, wants to simulate a structure in free space, a Dirichlet Boundary Condition will not suffice. Because the result will be distorted by unwanted reflections from the Dirichlet Boundary Condition. As a solution, one can place the structure under test 'far away' from all boundaries, but this will result in a very large computational domain that either takes ages to simulate or is practically not simulatable at all. Moreover, the configuration still suffers from late spurious reflections.

Solutions to this unworkable situation were provided by Gerrit Mur [6] and Zhen-Feng Liao [7]. Mur's boundary condition provided a computational cheap way to absorb impinging fields at the mesh boundary by using samples of the 3D scalar wave equation. Later, Liao proposed a new technique that outperformed Mur's. It uses extrapolation in space and time to counter impinging fields on the mesh boundary. In 1994, Jean-Pierre Bérenger introduced the Perfectly Matched Layer (PML) [8]–[10], a novel boundary condition that outperformed Mur's and Liao's boundary condition by orders of magnitude. It became the de facto standard ever since its introduction. A PML is deployed by adding

a few layers of PML cells at the outside of the computational domain. In order to create PML cells, Bérenger's split the field components of the mesh in two contributions, updating them separately with an altered update equation. Later on, different versions of the PML were developed. Specifically, a Uniaxial Perfectly Matched Layer (UPML) [11], being a material based PML, a Complex Frequency Shifted Perfectly Matched Layer (CFS-PML) [12], which has proven to be better at absorbing evanescent waves and a Convolution Perfectly Matched Layer (CPML) [13], being a variation on CFS-PML as used i.a. by Computer Simulation Technology's Microwave Studio® (CST-MWS®). It has been shown that a PML, in theory, is completely reflection-free. However, in practice, the discretization of the PML material and the finite number of PML layers introduce new, small, reflections. A PML is typically terminated by a Perfect Electric Conductor (PEC), although combinations with Mur's boundary condition have been made [14]. A note has to be made regarding PML corner regions (especially in 3D). Corner regions are notorious sources of reflections, even with uniform meshes. Jumping the gun a little, using non-uniform PML meshes does not solve this problem. On the contrary, using corner regions that are not perfectly matched (in terms of discretization) with their neighbouring PMLs is technically possible, but should be executed with great care, in order not to introduce too large reflection errors.

1.5.1 Complex coordinate transformation

In its simplest form, a PML is a variation on the standard FDTD cell that absorbs almost all electromagnetic waves. The transition from the standard mesh to the PML mesh is governed by the reflection coefficient

$$\Gamma = \frac{\eta_{std} - \eta_{pml}}{\eta_{std} + \eta_{pml}} \tag{1.18}$$

with $\eta = \sqrt{\mu/\varepsilon}$ the impedance of a medium. The transition is reflection-free if $\eta_{std} = \eta_{pml}$. However, to absorb the electromagnetic waves ε_{pml} and μ_{pml} are made complex valued. From here on, a more general approach will be used.

The different PML formalisms as listed above have been unified in [15], [16]. From there, it follows that a PML can be written as a complex coordinate transformation of the form

$$u_i \to \tilde{u}_i = \int_0^{u_i} s_i(\eta)\,\mathrm{d}\eta \qquad\qquad i \in \{0,1,2\} \tag{1.19}$$

PML theory relies partially on index rotation, which can be more easily written using $i \mod 3$ with $i \in \{0,1,2\}$ rather than using $i \in \{x,y,z\}$ as index. s_i is

the PML stretching function defined by

$$s_i(d) = \begin{cases} \kappa_i(d) + \dfrac{\sigma_i(d)}{\alpha_i(d) + \jmath\omega\varepsilon_0} & \text{PML absorbs in the } u_i\text{-direction} \\ 1 & \text{PML does not absorb in the } u_i\text{-direction} \end{cases} \tag{1.20}$$

The stretching function itself is built based on three functions κ (≥ 1), σ (≥ 0) and α (≥ 0) and d the distance to the grid/PML interface. There is no well-defined definition for these, only heuristic propositions. In [4], both a geometric and a polynomial profile for κ and σ are proposed ($\alpha = 0$).

$$\kappa_{\text{geom}}(d) = g^d \qquad \sigma_{\text{geom}}(d) = g^d\sigma_0 \tag{1.21}$$

$$\kappa_{\text{poly}}(d) = 1 + (\kappa_{max} - 1)d^m \qquad \sigma_{\text{poly}}(d) = d^m\sigma_{max} \tag{1.22}$$

where d is the distance to the mesh/PML interface expressed in number of cells and g, σ_0, m, σ_{max} and κ_{max} are parameters that can be tweaked to obtain optimal performance. Heuristics for a good choice for a wide range of problems exist. m is mostly chosen as $3 \leq m \leq 4$ and g as $2 \leq m \leq 3$. From a reflection analysis then follows that

$$\sigma_{max} = -\frac{(m+1)\ln R_0}{2\eta\delta} \tag{1.23a}$$

$$\sigma_0 = -\frac{\ln g \ln R_0}{2\eta\Delta\left(g^{\delta/\Delta} - 1\right)} \tag{1.23b}$$

with R_0 the amount of reflection allowed, η the impedance of the medium and δ the thickness of the PML and Δ the cell size. Usually $R_0 = \mathrm{e}^{-8}$ for a five cell thick PML and $R_0 = \mathrm{e}^{-16}$ for a ten layer thick PML. The profile of $\alpha(d)$ is usually chosen a constant (often 0) or a linear function with a small slope. In more recent literature, other profiles for κ and σ, such as hyperbolic profiles [17], [18], have been proposed.

Based on the analysis in [16] and mentioned in more detail in section 2.3, two types of PML, the Maxwellian and the non-Maxwellian PML, can be distinguished.

Maxwellian PML

The Maxwellian PML redefines the constitutive relations slightly, but leaves Maxwell's equations intact (hence the name). The new relations are given by

$$\boldsymbol{D} = \varepsilon_r\overline{\boldsymbol{\Lambda}}\boldsymbol{E} \tag{1.24a}$$

$$\boldsymbol{H} = \mu_r^{-1}\overline{\boldsymbol{\Lambda}}\boldsymbol{B} \tag{1.24b}$$

with

$$\overline{\boldsymbol{\Lambda}} = \operatorname{diag}\left(\frac{s_1 s_2}{s_0}, \frac{s_2 s_0}{s_1}, \frac{s_0 s_1}{s_2}\right) \tag{1.25}$$

with s_i given in both the frequency domain (FD) and the TD by

$$\begin{aligned} s_i(d) &\overset{\text{FD}}{=} \kappa_i(d) + \frac{\sigma_i(d)}{\jmath\omega\varepsilon_0} \\ &\overset{\text{TD}}{=} \kappa_i(d) + \frac{\sigma_i(d)\eta}{\partial_\tau} \end{aligned} \tag{1.26}$$

with η the impedance of free space. Maxwell's curl equations now look as follows

$$-\partial_\tau \overline{\overline{\boldsymbol{\Lambda}}}\boldsymbol{B} = \nabla \times \boldsymbol{E} \tag{1.27a}$$

$$\partial_\tau \varepsilon_r \overline{\overline{\boldsymbol{\Lambda}}}\boldsymbol{E} = \nabla \times \mu_r^{-1}\boldsymbol{B} \tag{1.27b}$$

Discretization of these equations needs an additional step compared to section 1.3.2. First split the diagonal elements in (1.25) in $\Lambda_i^{'} = s_{i+1}/s_i$ and $\Lambda_i^{''} = s_{i+2}$ ($i+1$ and $i+2$ are taken modulo 3 to obtain the correct index). Next split the curl equations as shown below for (1.27a)

$$\begin{aligned} Q_i &= \Lambda_i^{'} B_i \\ -\partial_\tau \Lambda_i^{''} Q_i &= \Big(\nabla \times \boldsymbol{E}\Big)_i \end{aligned} \tag{1.28}$$

Use the TD definition of (1.26) in the expansion of the equations above, substitute $(\sigma_i\eta)/(2\kappa_i)$ for ψ_i and rearrange the terms to get

$$\kappa_i\big(\partial_\tau Q_i^B + \psi_i Q_i^B\big) = \kappa_{i+1}(\partial_\tau B_i + \psi_{i+1} B_i) \tag{1.29a}$$

$$\kappa_{i+2}\big(\partial_\tau Q_i^B + \psi_{i+2} Q_i^B\big) = \Big(\nabla \times \boldsymbol{E}\Big)_i \tag{1.29b}$$

Using the central differencing theorem on the τ-derivative and solving for Q_i^{B,n^+} and $B_i^{n^+}$, results in

$$Q_i^{B,n^+} = \frac{1-\Delta\tau\psi_{i+2}}{1+\Delta\tau\psi_{i+2}} Q_i^{B,^-} - \frac{1}{\kappa_{i+2}} \frac{1}{1+\Delta\tau\psi_{i+2}} \Delta\tau \Big(\nabla \times \boldsymbol{E}\Big)_i^n \tag{1.30a}$$

$$\begin{aligned} B_i^{n^+} &= \frac{1-\Delta\tau\psi_{i+1}}{1+\Delta\tau\psi_{i+1}} B_i^{n^-} + \frac{\kappa_i}{\kappa_{i+1}} \left(\frac{1+\Delta\tau\psi_i}{1+\Delta\tau\psi_{i+1}} Q_i^{B,^+} - \frac{1-\Delta\tau\psi_i}{1+\Delta\tau\psi_{i+1}} Q_i^{B,n^-} \right) \\ &= \frac{1-\Delta\tau\psi_{i+1}}{1+\Delta\tau\psi_{i+1}} B_i^{n^-} + \frac{\kappa_i}{\kappa_{i+1}} \frac{\Delta Q_i^B + \Delta\tau\psi_i \left\langle Q_i^B \right\rangle}{1+\Delta\tau\psi_{i+1}} \end{aligned} \tag{1.30b}$$

with $\Delta Q_i^B = \left(Q_i^{B,n^+} - Q_i^{B,n^-}\right)$ and $\left\langle Q_i^B \right\rangle = \left(Q_i^{B,n^+} + Q_i^{B,n^-}\right)$. Note the occurrence of up_B as defined in (1.12b). This means that the PML update equation is just an alteration of the original update equation. This allows for

some efficient code refactoring during implementation. Analogously, one gets

$$Q_i^{E,n^{++}} = \frac{1-\Delta\tau\psi_{i+2}}{1+\Delta\tau\psi_{i+2}} Q_i^{E,n} + \frac{1}{\kappa_{i+2}} \frac{1}{1+\tau\psi_{i+2}} \Delta\tau(\varepsilon_r\mu_r)^{-1} \Big(\nabla \times \boldsymbol{B}\Big)_i^{n^+} \tag{1.31a}$$

$$E_i^{n^{++}} = \frac{1-\Delta\tau\psi_{i+1}}{1+\Delta\tau\psi_{i+1}} E_i^{n} + \frac{\kappa_i}{\kappa_{i+1}} \frac{\Delta Q_i^E + \Delta\tau\psi_i \left\langle Q_i^E \right\rangle}{1+\Delta\tau\psi_{i+1}} \tag{1.31b}$$

with $\Delta Q_i^E = \Big(Q_i^{E,n^{++}} - Q_i^{E,n}\Big)$ and $\left\langle Q_i^E \right\rangle = \Big(Q_i^{E,n^{++}} + Q_i^{E,n}\Big)$. Again, up_E can be recognized.

non-Maxwellian PML

To construct a non-Maxwellian PML, Maxwell's equations are slightly altered. In the example below (following [12]), the definition of the curl is adapted to include the stretching function $s(d)$ as defined below

$$\begin{aligned} s_i(d) &\overset{FD}{=} \kappa_i(d) + \frac{\sigma_i(d)}{\alpha_i(d) + \jmath\omega\varepsilon_0} \\ &\overset{TD}{=} \kappa_i(d) + \frac{\sigma_i(d)}{\alpha_i(d) + \frac{\partial_\tau}{\eta}} \end{aligned} \tag{1.32}$$

Redefine ∇ as

$$\nabla_s = \sum_{i=0}^{2} \boldsymbol{u}_i \frac{1}{s_i} \partial_i \tag{1.33}$$

And use this in Maxwell's curl equations to get

$$-\partial_\tau \boldsymbol{B} = \nabla_s \times \boldsymbol{E} \tag{1.34a}$$

$$\partial_\tau \varepsilon_r \boldsymbol{E} = \nabla_s \times \mu_r^{-1} \boldsymbol{B} \tag{1.34b}$$

Now, start by rewriting s_i as

$$\frac{1}{s_i} = \frac{1}{\kappa_i} - \frac{1}{\kappa_i B_i} \tag{1.35}$$

with

$$B_i = 1 + \frac{1}{\psi_i}(\beta_i + \partial_\tau) \tag{1.36}$$

where $\psi_i = \sigma_i\eta/\kappa_i$ and $\beta_i = \eta\alpha_i$

The stretched curl consists of two spatial derivatives. Each of them can be written as

$$\frac{1}{s_i}\partial_i E_j = \frac{1}{\kappa_i}\partial_i E_j + \frac{Q_{ij}^E}{\Delta\tau} = \tilde{\partial}_i E_j + \frac{Q_{ij}^E}{\Delta\tau} \tag{1.37a}$$

$$Q_{ij}^E = -\frac{\Delta\tau}{\kappa_i B_i}\partial_i E_j = -\frac{\Delta\tau}{B_i}\tilde{\partial}_i E_j \tag{1.37b}$$

where $\tilde{\partial}_i$ indicates a scaling of ∂_i by κ_i. Grouping the different $\tilde{\partial}_i$ results in a scaled rotor, indicated by $\tilde{\nabla}$. This basically means, that within the PML, all cells have a length $\kappa_i \Delta i$. Note that, due to the length difference between standard cells and PML cells, a good subgridding algorithm is needed to describe this interface.

Equation (1.37b) has to be transformed to the time-domain and can be rewritten as

$$\partial_\tau Q_{ij}^E + (\psi_i + \beta_i) Q_{ij}^E = -\Delta\tau \psi_i \tilde{\partial}_i E_j \tag{1.38}$$

After discretizing the time derivative, equations (2.30b) and (1.38) look as follows

$$\boldsymbol{B}^{n^+} = \boldsymbol{B}^{n^-} - \Delta\tau \big(\tilde{\nabla} \times \boldsymbol{E}\big)^n + \Delta \boldsymbol{Q}^{E,n^+} \tag{1.39a}$$

$$Q_{ij}^{E,n^+} = \frac{1}{1 + \Delta\tau(\psi_i + \beta_i)} \Big(Q_{ij}^{E,n^-} - \Delta\tau \psi_i \Delta\tau \tilde{\partial}_i E_j^n \Big) \tag{1.39b}$$

with

$$\Delta \boldsymbol{Q}^{\xi,\nu} = \sum_{k=0}^{2} \Big(Q_{ij}^{\xi,\nu} - Q_{ji}^{\xi,\nu} \Big) \qquad \text{with} \begin{cases} i = (k+1) \bmod 3 \\ j = (k+2) \bmod 3 \end{cases} \tag{1.40}$$

defined at time instance ν for $\xi \in \{E, B\}$. Note that for stability reasons the transition from (1.38) to (1.39b) $Q_{ij}^E = Q_{ij}^{E,n^+}$ is applied instead of $Q_{ij}^E = (Q_{ij}^{E,n^+} + Q_{ij}^{E,n^-})/2$, as is usual in FDTD. Also remark that both equations above use $\Delta\tau\tilde{\partial}_i E_j^n$ and $\Delta\tau\tilde{\partial}_j E_i^n$, so this quantity only needs to be calculated once. Again, up_B is recovered, but applied to cells of size $\kappa_x \Delta x \times \kappa_y \Delta y \times \kappa_z \Delta z$. This again allows some code refactoring. For the E-fields the following analogous equations hold

$$\boldsymbol{E}^{n^{++}} = \boldsymbol{E}^n + \Delta\tau(\varepsilon_r \mu_r)^{-1} \Big(\tilde{\nabla} \times \boldsymbol{B}^{n^+} \Big) + \Delta \boldsymbol{Q}^{B,n^{++}} \tag{1.41a}$$

$$Q_{ij}^{B,^{++}} = \frac{1}{1 + \Delta\tau(\psi_i + \beta_i)} \left(Q_{ij}^{B,n} - \Delta\tau \psi_i \frac{\Delta\tau}{\varepsilon_r \mu_r} \tilde{\partial}_i B_j^{n^+} \right) \tag{1.41b}$$

References

[1] K. S. Yee, "Numerical solution of initial boundary value problems involving maxwell's equations in isotropic media", *IEEE Transactions on Antennas and Propagation*, vol. 14, no. 3, pp. 302–307, May 1966, issn: 0018-926X.

[2] R. A. Chilton and R. Lee, "Conservative and Provably Stable FDTD Subgridding", *IEEE Transactions on Antennas and Propagation*, vol. 55, no. 9, pp. 2537–2549, Sep. 2007, issn: 0018-926X.

[3] R. A. Chilton, "H-, P-, And T-Refinement Strategies For The Finite-Difference-Time-Domain (FDTD) Method Development Via Finite-Element (FE) Principles", PhD thesis, Ohio State University, 2008.

[4] A. Taflove and S. C. Hagness, *Computational Electrodynamics: The Finite-Difference-Time-Domain Method*, 2nd. Artech House, 2000, ISBN 1-58053-076-1.

[5] W. Tierens and D. De Zutter, "BOR-FDTD subgridding based on finite element principles", *Journal of Computational Physics*, vol. 230, no. 12, pp. 4519–4535, Jun. 2011, issn: 0021-9991.

[6] G. Mur, "Absorbing Boundary Conditions for the Finite-Difference Approximation of the Time-Domain Electromagnetic-Field Equations", *IEEE Transactions on Electomagnetic Compatibility*, vol. 23, no. 4, pp. 377–382, Nov. 1981.

[7] Z.-F. Liao, K.-L. Huang, B.-P. Yang, and Y.-F. Yuan, "A transmitting boundary for transient wave analyses", *SCIENCE CHINA Mathematics*, vol. 27, no. 10, 1063, p. 1063, 1984. [Online]. Available: `http://math.scichina.com:8081/sciAe/EN/Y1984/V27/I10/1063`.

[8] J.-P. Bérenger, "A Perfectly Matched Layer for the Absorption of Electromagnetic Waves", *Journal of Computational Physics*, vol. 114, pp. 185–200, Oct. 1994.

[9] J.-P. Bérenger, "Perfectly matched layer for the FDTD solution of wave-structure interaction problems", *IEEE Transactions on Antennas and Propagation*, vol. 44, no. 1, pp. 110–117, Jan. 1996, issn: 0018-926X.

[10] J.-P. Bérenger, "Three-Dimensional Perfectly Matched Layer for the Absorption of Electromagnetic Waves", *Journal of Computational Physics*, vol. 127, no. 2, pp. 363–379, 1996, issn: 0021-9991.

[11] S. D. Gedney, "An anisotropic perfectly matched layer-absorbing medium for the truncation of FDTD lattices", *IEEE Transactions on Antennas and Propagation*, vol. 44, no. 12, pp. 1630–1639, Dec. 1996, issn: 0018-926X.

[12] S. D. Gedney and B. Zhao, "An Auxiliary Differential Equation Formulation for the Complex-Frequency Shifted PML", *IEEE Transactions on Antennas and Propagation*, vol. 58, no. 3, pp. 838–847, Mar. 2010, issn: 0018-926X.

[13] J. A. Roden and S. D. Gedney, "Convolution PML (CPML): An efficient FDTD implementation of the CFS–PML for arbitrary media", *Microwave and Optical Technology Letters*, vol. 27, no. 5, pp. 334–339, Dec. 2000, issn: 1098-2760.

[14] C. Peng and F. Shao-Jun, "A novel mixed FDTD absorbing boundary condition based on mur and PML", in *Antennas Propagation and EM Theory (ISAPE), 2010 9th International Symposium on*, Nov. 2010, pp. 791–793.

[15] W. C. Chew, J.-M. Jin, and E. Michielssen, "Complex coordinate stretching as a generalized absorbing boundary condition", *Microwave and Optical Technology Letters*, vol. 15, no. 6, pp. 363–369, Aug. 1997, issn: 1098-2760.

[16] F. L. Teixeira and W. C. Chew, "Differential Forms, Metrics, and the Reflectionless Absorption of Electromagnetic Waves", *Journal of Electromagnetic Waves and Applications*, vol. 13, no. 5, pp. 665–686, 1999.

[17] A. Bermúdez, L. Hervella-Nieto, A. Prieto, and R. Rodrígez, "An Exact Bounded Perfectly Matched Layer for Time-Harmonic Scattering Problems", *SIAM Journal on Scientific Computing*, vol. 30, no. 1, pp. 312–338, 2008. [Online]. Available: `http://epubs.siam.org/doi/abs/10.1137/060670912`.

[18] A. Modave, A. Kameni, J. Lambrechts, E. Delhez, n. Lionel Pichon, and C. Geuzaine, "An optimum PML for scattering problems in time-domain", *The European Physical Journal Applied Physics*, Jul. 2013, issn: 1286-0050. [Online]. Available: `http://www.epjap.org/article_S1286004213304479`.

2

Introduction to differential geometry

★ ★ ★

The mathematical base of differential geometry provides an excellent framework for the description of the subgridding of mesh cells in the Finite Difference Time Domain method. In this chapter an introduction to some continuous and discrete concepts will be given. This introduction is neither extensive nor complete, but just touches those topics on which will be built later to describe subgridding. Special care is given to the description of electromagnetic concepts in general and Maxwell's equations in particular. Most concepts are introduced for an arbitrary dimension n, in practice, for the description of Maxwell's equations, $n = 3$. More information can be found in the relevant literature, e.g. [1]–[3]

Differential geometry is a branch of mathematics in which a combination of differential calculus, integral calculus, linear algebra and multilinear algebra is used to solve geometrical problems. This specific branch is well suited to solve the subgridding problem in the Finite Difference Time Domain method (FDTD). Therefore, Maxwell's equations need to be expressed in this format.

In this section, first, a concise introduction to the notation format and basics of (discrete) differential geometry will be presented. Next, Maxwell's equations will be expressed so they can be used further on in the derivation of FDTD subgridding.

2.1 Continuous differential geometry

Differential geometry uses differential forms, a representation of multivariable calculus that is independent of coordinates. Differential forms have a dimension k (and are therefore called k-forms) and are denoted as ω^k. Forms operate in an open region $\mathcal{M} \subset \mathbb{R}^n$ (also called an n-manifold). Denote by $T_x\mathcal{M}$ the vector space containing all vectors in the point $x \in \mathcal{M}$ that are tangential to $\mathcal{M}$. ω^k is thus a multilinear map from $(T_x\mathcal{M})^k$ to $\mathbb{R}$.

$$\omega^k : \overbrace{T_x\mathcal{M} \times \ldots \times T_x\mathcal{M}}^{k} \to \mathbb{R} \tag{2.1}$$

ω^k is a rank-k, anti-symmetric tensor field over $\mathcal{M}$. Informally, a form can be seen as an integrand. A 1-form, then, can be seen as the $\mathrm{d}x$ in $\int \mathrm{d}x$, a 2-form can be seen as $\mathrm{d}x\,\mathrm{d}y$ in $\int \mathrm{d}x\,\mathrm{d}y$, and so on.

For differential forms, seven operators are defined, from which three will be introduced below. The first one is the wedge product or exterior product ($\wedge$). It is used to create higher order forms from lower order forms. The wedge product is the bilinear form

$$\left(\alpha^k \wedge \beta^\ell\right)_x(u, v) = \alpha_x^k(u)\beta_x^\ell(v) - \alpha_x^k(v)\beta_x^\ell(u) \tag{2.2}$$

for $u, v \in T_x\mathcal{M}$. The wedge product of a k-form and a ℓ-form is a $(k+\ell)$-form. The wedge product is also asymmetric

$$\left(\alpha^k \wedge \beta^\ell\right) = (-1)^{k\ell}\left(\beta^\ell \wedge \alpha^k\right) \tag{2.3}$$

The second operator is the exterior derivative (d). The exterior derivative of a k-form ω^k is a $(k+1)$-form $\mathrm{d}\omega^k$. More correctly, it is the unique mapping from k-forms to $k+1$-forms satisfying

- if f is a smooth function (0-form), then $\mathrm{d}f$ is the differential of f
- $\mathrm{d}(\mathrm{d}\omega) = 0$
- $\mathrm{d}(\alpha^p \wedge \beta^q) = \mathrm{d}\alpha^p \wedge \beta^q + (-1)^p \alpha^p \wedge \mathrm{d}\beta^q$

Integrating an exterior derivative, satisfies Stoke's theorem

$$\int_{\mathcal{M}} \mathrm{d}\omega^k = \int_{\partial\mathcal{M}} \omega^k \tag{2.4}$$

Note that the exterior derivative represents the gradient, the curl as well as the divergence in vector calculus. Therefore the second property above translates to both $\nabla \times (\nabla\phi) = 0$ and $\nabla \circ (\nabla \times \boldsymbol{A}) = 0$.

Before the third operator can be introduced, a metric needs to be defined. This is done by an order-n tensor $\overline{\overline{\boldsymbol{g}}}$ (an Euclidean three dimensional space would

have $\overline{\overline{\boldsymbol{g}}} = \overline{\mathbf{1}}_{3\times3}$). With a metric defined, a volume n-form ν^n can be constructed as

$$\nu^n = \sqrt{\det \overline{\overline{\boldsymbol{g}}}}\, \mathrm{d}x^1 \wedge \ldots \wedge \mathrm{d}x^n \tag{2.5}$$

Given a metric, an inner product ($\langle\cdot,\cdot\rangle$) can be introduced as a way to measure the projection of one form onto another. With the metric in place, the third operator, the Hodge star ($\star$), can be introduced. The Hodge-star operator maps a k-form to a $(n-k)$-form, with n the order of the manifold. It is defined as

$$\alpha^k \wedge \star\beta^k = \langle \alpha^k, \beta^k \rangle \nu^n \tag{2.6}$$

An important property of this operator is $\star\star\,\omega^k = (-1)^{(n-k)k}\omega^k$

2.1.1 Maxwell's equations

In the physical three dimensional world the maximum order of forms will be restricted to $n = 3$. The different electromagnetic quantities are represented by different order of forms. H and E-fields are represented by 1-forms, D and B-fields are represented by 2-forms. The electric current density j and charge density ρ are represented by 2-forms and 3-forms, respectively. As can be seen from the proposed mapping between physical quantities and k-forms, 1 and 2-forms are vector functions, whereas 0 and 3-forms are scalar functions.

The curl and divergence in Maxwell's equations are, as mentioned before, both represented by the exterior derivative. Note that Maxwell's equations (excluding the constitutive equations) do not need any metric defined on the system to be expressed using differential forms. The constitutive equations on the other hand, do need a metric since they are expressed by means of a scaled (indicated by ε and μ) Hodge star operator.

$$\begin{aligned} \mathrm{d}E &= -\partial_\tau B & \qquad \mathrm{d}H &= \partial_\tau D + j \\ \mathrm{d}D &= \rho & \qquad \mathrm{d}B &= 0 \\ D &= \star_{\varepsilon_r} E & \qquad H &= \star_{\mu_r^{-1}} B \end{aligned} \tag{2.7}$$

2.2 Discrete Whitney forms [4]

To obtain a discrete differential representation of Maxwell's equations, the concepts above need to be discretized on a conformal mesh (= discrete manifold $\mathcal{C}$). For any two cells in a conformal mesh the following holds: the intersection of the two cells contains either an entire face, edge, node or nothing. The cells, faces, edges and nodes of the mesh are all simplices of different order. A k-simplex, σ^k, is defined as the convex hull of $k+1$ geometrically distinct points $\{v_0, v_1, \ldots, v_k\} \in \mathbb{R}^n$

The mapping from the continuous k-form ω^k to the discrete form (also called k-co-chain) $\omega^k[i]$ is done as follows

$$\omega^k[i] = \int_{\partial\sigma_i} \omega^k \tag{2.8}$$

$\partial\sigma$ is the boundary operator working on simplex σ. The boundary operator is defined as

$$\partial\{v_0 \dots v_k\} = \sum_{j=0}^{k} (-1)^j \{v_0, \dots, v_{j-1}, v_{j+1}, \dots, v_k\} \tag{2.9}$$

The definition of a discrete exterior derivative can be done by means of Stoke's theorem

$$\int_{\sigma^k} \mathrm{d}\omega^k = \int_{\partial\sigma^k} \omega^k \tag{2.10}$$

Finally a discrete Hodge star operator needs to be defined. In order to do so, the notion of a (circumcentric) dual mesh needs to be introduced. With the circumcentre of a k-simplex being the centre of the unique k-sphere going trough all $k+1$ points of σ^k. The dual mesh is constructed by correctly connecting those circumcentres. The dual of a k-simplex is a $(n-k)$-simplex. More specifically, the dual of a n-simplex is the circumcentre itself. The Hodge star transforms from the primal to the dual mesh with an appropriate scaling defined by

$$\frac{1}{|\sigma^k|} \int_{\sigma^k} \omega^k = \frac{1}{|{*\sigma^k}|} \int_{*\sigma^k} {*\omega^k} \tag{2.11}$$

where $*$ indicates the duality.

In practice, n equals 3. This means that a 0-simplex is a point, a 1-simplex an edge, a 2-simplex a face and a 3-simplex is a tetrahedron. In an electromagnetic context, E and B-fields are 1-simplices and 2-simplices, respectively, on the primal mesh (i.e. primal edges and primal faces, respectively). H and D-fields are 1-simplices and 2-simplices, respectively, on the dual mesh. This is explicitly expressed by the constitutive equations. The appropriate scaling between primal and dual mesh is expressed by μ_r and ε_r. This concept of primal and dual meshes gives rise to the staggered grid typical to FDTD.

For FDTD, a point wise evaluation of the discrete k-forms is necessary. Some interpolation is needed between the k-forms. Simple linear interpolation can be used for 0-forms. Define a basis function ϕ_i for each point v_i, which equals 1 at exactly v_i and 0 elsewhere. These functions form a basis of discrete 0-forms. They are called Whitney forms of order 0 (W_0), because in [4] Whitney derived the expressions for bases of higher order forms.

$$\phi_{\sigma_{i_0,\dots,i_k}} = k! \sum_{j=0}^{k} (-1)^j \phi_{i_j} \, \mathrm{d}\phi_{i_0} \wedge \dots \wedge \mathrm{d}\phi_{i_{j-1}} \wedge \mathrm{d}\phi_{i_{j+1}} \wedge \dots \wedge \mathrm{d}\phi_{i_k} \tag{2.12}$$

All theory above can be extended towards rectangular cuboidal 3-simplices (cuboids from here on) instead of tetrahedral 3-simplices, which is necessary for the typical cuboidal FDTD mesh. Below explicit equations for the cuboidal Whitney forms will be derived. In that regard, two base functions need to be defined

$$f^i(u) = \begin{cases} 1 - i + \frac{u}{\Delta u} & if \quad i-1 \leqslant \frac{u}{\Delta u} \leq i \\ 1 + i - \frac{u}{\Delta u} & if \quad i \leqslant \frac{u}{\Delta u} \leq i+1 \\ 0 & otherwise \end{cases} \tag{2.13}$$

$$g^{i+\frac{1}{2}}(u) = \begin{cases} 1 & if \quad i \leqslant \frac{u}{\Delta u} \leq i+1 \\ 0 & otherwise \end{cases} \tag{2.14}$$

Note that

$$\frac{\partial}{\partial u}\begin{bmatrix} f^0(u) \\ f^1(u) \end{bmatrix} = \frac{1}{\Delta u}\begin{bmatrix} -1 \\ +1 \end{bmatrix} g^{\frac{1}{2}}(u) \tag{2.15}$$

With the equations (2.12) and (2.13) the definition of the Whitney forms is as follows (with $\boldsymbol{r} = [x, y, z]$)

$$\begin{aligned} W_0^{i,j,k}(\boldsymbol{r}) &= f^i(x) \cdot f^j(y) \cdot f^k(z) \\ \boldsymbol{W}_1^{\frac{1}{2},j,k}(\boldsymbol{r}) &= \boldsymbol{x}^0 \cdot g^{\frac{1}{2}}(x) \cdot f^j(y) \cdot f^k(z) \\ \boldsymbol{W}_2^{i,\frac{1}{2},\frac{1}{2}}(\boldsymbol{r}) &= \boldsymbol{x}^0 \cdot f^i(x) \cdot g^{\frac{1}{2}}(y) \cdot g^{\frac{1}{2}}(z) \\ W_3^{\frac{1}{2},\frac{1}{2},\frac{1}{2}}(\boldsymbol{r}) &= g^{\frac{1}{2}}(x) \cdot g^{\frac{1}{2}}(y) \cdot g^{\frac{1}{2}}(z) \end{aligned} \tag{2.16}$$

with $i, j, k \in \{0, 1\}$. The coefficients ± 1 from (2.15) can be cast in a matrix $\overline{\boldsymbol{C}}_k$, which will function as the discrete representation of the discrete exterior derivative operator of order k. In practice, $\overline{\boldsymbol{C}}_k$ will be the incidence matrix of $k+1$-forms with k-forms. As mentioned before the exterior derivative is the representation of the gradient, the curl as well as the divergence in vectorial calculus. d_1 is the curl and therefore $\overline{\overline{\boldsymbol{C}}}_1$ is its discrete representation. The $\overline{\overline{\boldsymbol{C}}}_1$ of the Yee-cell in Fig. 1.2 looks as follows (where the order of fields is taken from x to z, from left to right, from bottom to top and from front to back)

$$\overline{\overline{\boldsymbol{C}}}_1 = \begin{array}{c} \begin{matrix} E_x^1 & E_x^2 & E_x^3 & E_x^4 & E_y^1 & E_y^2 & E_y^3 & E_y^4 & E_z^1 & E_z^2 & E_z^3 & E_z^4 \end{matrix} \\ \begin{bmatrix} 0 & 0 & 0 & 0 & -1 & 0 & 1 & 0 & -1 & 0 & 1 & 0 \\ 0 & 0 & 0 & 0 & 0 & -1 & 0 & 1 & 0 & -1 & 0 & 1 \\ -1 & 1 & 0 & 0 & 0 & 0 & 0 & 0 & -1 & 1 & 0 & 0 \\ 0 & 0 & -1 & 1 & 0 & 0 & 0 & 0 & 0 & 0 & -1 & 1 \\ -1 & 0 & 1 & 0 & -1 & 1 & 0 & 0 & 0 & 0 & 0 & 0 \\ 0 & -1 & 0 & 1 & 0 & 0 & -1 & 1 & 0 & 0 & 0 & 0 \end{bmatrix} \begin{matrix} B_x^1 \\ B_x^2 \\ B_y^1 \\ B_y^2 \\ B_z^1 \\ B_z^2 \end{matrix} \end{array} \tag{2.17}$$

2.3 Perfectly Matched Layer

As mentioned in section 1.5, to simulate free space, an absorbing boundary condition is needed. The best formulation available is the Perfectly Matched Layer (PML). A PML can be constructed by using a complex coordinate transformation. This calls again for the use of a metric. Assuming a coordinate system with three orthogonal axes (meaning the metric tensor is diagonal) the metric tensor can be written, using Einstein's notation, as

$$(\mathrm{d}s)^2 = \overline{\overline{\boldsymbol{g}}} = \sum_{i=0}^{2} \big(h_i \,\mathrm{d}x^i\big)\big(h_i \,\mathrm{d}x^i\big) = \sum_{i=0}^{2} h_i^2 \,\mathrm{d}x^i \,\mathrm{d}x^i = \sum_{i=0}^{2} g_{ii} \,\mathrm{d}x^i \,\mathrm{d}x^i \tag{2.18}$$

with h_i some scaling coefficients and $\overline{\overline{\boldsymbol{g}}}$ as used in (2.5). The transformation is governed by

$$\mathrm{d}x^i \to \mathrm{d}\tilde{x}^i = \frac{\tilde{h}_i}{h_i} \,\mathrm{d}x^i \tag{2.19}$$

and therefore

$$(\mathrm{d}s)^2 \to (\mathrm{d}\tilde{s})^2 = \sum_{i=0}^{2} g_{ii} \,\mathrm{d}\tilde{x}^i \,\mathrm{d}\tilde{x}^i = \sum_{i=0}^{2} g_{ii} \frac{\tilde{h}_i^2}{h_i^2} \,\mathrm{d}x^i \,\mathrm{d}x^i = \sum_{i=0}^{2} \tilde{g}_{ii} \,\mathrm{d}x^i \,\mathrm{d}x^i \tag{2.20}$$

The coordinate mapping from Cartesian to 'PML-coordinates' is governed by

$$\boldsymbol{x}^i \to \tilde{\boldsymbol{x}}^i = \int_0^{x^i} s_i(\xi) \,\mathrm{d}\xi \tag{2.21}$$

This means that $h_i = 1$ and $\tilde{h}_i = s_i$ if the PML absorbs in the x^i-direction and $h_i = \tilde{h}_i = 1$ if it does not.

Because there are two equivalent expressions for $(\mathrm{d}\tilde{s})^2$, two PML formalisms can be expressed, one based on $(\mathrm{d}\tilde{s})^2\big(\mathrm{d}x^0, \mathrm{d}x^1, \mathrm{d}x^2\big)$ and the other based on $(\mathrm{d}\tilde{s})^2\big(\mathrm{d}\tilde{x}^0, \mathrm{d}\tilde{x}^1, \mathrm{d}\tilde{x}^2\big)$.

$$\widetilde{\overline{\overline{\boldsymbol{g}}}} = s_0^2 \boldsymbol{x}^0 \boldsymbol{x}^0 + s_1^2 \boldsymbol{x}^1 \boldsymbol{x}^1 + s_2^2 \boldsymbol{x}^2 \boldsymbol{x}^2 \tag{2.22}$$

$$= 1\tilde{\boldsymbol{x}}^0 \tilde{\boldsymbol{x}}^0 + 1\tilde{\boldsymbol{x}}^1 \tilde{\boldsymbol{x}}^1 + 1\tilde{\boldsymbol{x}}^2 \tilde{\boldsymbol{x}}^2 \tag{2.23}$$

They are called the Maxwellian and the non-Maxwellian PML, respectively.

2.3.1 Maxwellian Perfectly Matched Layer

The Maxwellian PML uses the formalism in (2.22), meaning that E and D-fields (and H and B-fields accordingly) are given in differential form and mapped to

vectors by

$$\begin{aligned}
\tilde{E} =& \sum_{i=0}^{2} \tilde{E}_i \tilde{h}_i \,\mathrm{d}x^i && \xrightarrow{g} \quad \boldsymbol{E} = \sum_{i=0}^{2} \frac{\tilde{h}_i}{h_i} \tilde{E}_i \boldsymbol{x}^i \\
\tilde{D} =& \sum_{i,j=0}^{2} \varepsilon_{ij} \tilde{E}_j \tilde{h}_{i+1} \tilde{h}_{i+2} \,\mathrm{d}x^{i+1} \,\mathrm{d}x^{i+2} && \xrightarrow{g} \quad \boldsymbol{D} = \sum_{i,j=0}^{2} \varepsilon_{ij} \tilde{E}_j \frac{\tilde{h}_{i+1} \tilde{h}_{i+2}}{h_{i+1} h_{i+2}} \boldsymbol{x}^i
\end{aligned} \tag{2.24}$$

The mapping above retains the form of the Maxwell's equations, but changes the form of the constitutive equations. In this formula substitute $\tilde{h}_i = s_i$ and write down the constitutive equation for the PML

$$\begin{aligned}
\tilde{D} =& \tilde{\varepsilon}_r \tilde{E} && \text{with } \tilde{\varepsilon}_{ij} = \frac{\tilde{h}_{i+1} \tilde{h}_{i+2}}{\tilde{h}_j} \varepsilon_{ij} = \frac{s_{i+1} s_{i+2}}{s_j} \varepsilon_{ij} \\
\boldsymbol{D} =& \tilde{\varepsilon}_r \boldsymbol{E} && \text{with } \tilde{\varepsilon}_{ij} = \frac{\tilde{h}_{i+1} \tilde{h}_{i+2} h_j}{h_{i+1} h_{i+2} \tilde{h}_j} \varepsilon_{ij}
\end{aligned} \tag{2.25}$$

For an orthogonal base, this results in using Λ

$$\tilde{\boldsymbol{D}} = \overline{\boldsymbol{\Lambda}} \varepsilon_r \tilde{\boldsymbol{E}} \tag{2.26a}$$

$$\tilde{\boldsymbol{B}} = \overline{\boldsymbol{\Lambda}} \mu_r \tilde{\boldsymbol{H}} \tag{2.26b}$$

with

$$\overline{\boldsymbol{\Lambda}} = \frac{s_1 s_2}{s_0} \boldsymbol{x}^0 \boldsymbol{x}^0 + \frac{s_2 s_0}{s_1} \boldsymbol{x}^1 \boldsymbol{x}^1 + \frac{s_0 s_1}{s_2} \boldsymbol{x}^2 \boldsymbol{x}^2 \tag{2.27}$$

This can be discretized as in section 1.5.1

2.3.2 non-Maxwellian Perfectly Matched Layer

To construct the non-Maxwellian PML the metric $\tilde{g}$ (2.23) is used to map forms to vectors

$$\begin{aligned}
\tilde{E} =& \sum_{i=0}^{2} \tilde{E}_i \tilde{h}_i \,\mathrm{d}x^i && \xrightarrow{\tilde{g}} \quad \boldsymbol{E} = \sum_{i=0}^{2} \tilde{E}_i \boldsymbol{x}^i \\
\tilde{D} =& \sum_{i,j=0}^{2} \varepsilon_{ij} \tilde{E}_j \tilde{h}_{i+1} \tilde{h}_{i+2} \,\mathrm{d}x^{i+1} \,\mathrm{d}x^{i+2} && \xrightarrow{\tilde{g}} \quad \boldsymbol{D} = \sum_{i,j=0}^{2} \varepsilon_{ij} \tilde{E}_j \boldsymbol{x}^i
\end{aligned} \tag{2.28}$$

With this formalism the constitutive equation remain unaltered, but Maxwell's equations are changed slightly. The alteration can be caught into the curl operator

$$\nabla_s \times \cdot = \sum_{i=0}^{2} \boldsymbol{x}^i \frac{1}{s_i} \partial_{x^i} \cdot \tag{2.29}$$

And thus

$$-\partial_\tau \boldsymbol{B} = \nabla_s \times \boldsymbol{E} \tag{2.30a}$$

$$\partial_\tau \varepsilon_r \boldsymbol{E} = \nabla_s \times \mu_r^{-1} \boldsymbol{B} \tag{2.30b}$$

This can be discretized using section 1.5.1

References

[1] K. F. Warnick, R. H. Selfridge, and D. V. Arnold, "Teaching electromagnetic field theory using differential forms", *IEEE Transactions on Education*, vol. 40, no. 1, pp. 53–68, Feb. 1997, issn: 0018-9359.

[2] S. C. Preston, *An Introduction to Differential Geometry*, Feb. 2011.

[3] J. W. Robbin and D. A. Salamon, *Introduction to Differential Geometry*, Jan. 2011.

[4] H. Whitney, *Geometric Integration Theory*, M. Morse and A. W. Tucker, Eds. Princeton University Press, 1957.

3

Numerical assessment of the combination of subgridding and the Perfectly Matched Layer grid termination in the Finite Difference Time Domain method

based on the article published in the International Journal of Numerical Modelling: Electronic Networks, Devices and Fields, 2014 [1] and presented during EMF 2013 [2]

★ ★ ★

We present a unified framework that includes the subgridding of Perfectly Matched Layers (PMLs). Next, the interaction between the problem space and the (subgridded) PMLs is studied. Therefore, different (geometrical) subgridding strategies for the PML are considered. We numerically investigate the effect of these strategies by determining the reflection of a point source caused by the PML. It becomes possible to not only determine the general reflection level, but also to pinpoint the precise source of the reflections. The conclusion of this study is that, as expected, important reflections are found originating from the corner points of the PML, but that these reflections worsen when grid non-uniformities are present due to subgridding. Hence, the combination of subgridding and PMLs should be handled with great care.

3.1 Introduction

Together with the Finite Element method (FE) and integral equation techniques solved by the Method of Moments (MoM), the Finite Difference Time Domain method (FDTD) [3]), is a well-established numerical method for the full-wave simulation of electromagnetic problems. Amongst others, its advantages over its competitors are: the vastly larger number of unknowns it can solve for, the possibilities to include non-linearities and its suitability to be massively parallelised. On the downside, however, in its basic form, the mesh has to be kept strictly uniform in order to maintain an explicit formulation. Therefore, the inclusion of electrically small design components in a large computational domain leads to either huge memory requirements and unacceptable simulation times, or inaccurate results.

To overcome this problem, many different schemes for (spatial) subgridding of the FDTD mesh were proposed. From those, only a few were passive, stable and reciprocal. And from those, none offered the freedom to choose different refinement factors along different mesh directions. Yet, flexible subgridding would not only provide a far better possibility to design certain structures in FDTD, it also reduces calculation time by not forcing the designer to use the finest cell size everywhere within the simulation domain. This leads to more precise simulation results obtained in a more efficient way.

For open structures, such as, for example, antennas, FDTD implementations require a form of mesh termination that mimics free space. The Perfectly Matched Layer (PML) introduced by Jean-Pierre Bérenger in 1994 [4] has become the de facto standard for absorbing boundary conditions in FDTD. Although the PML is reflection-free in theory, in practice, after discretization, reflections are introduced in the calculation domain. To minimize these errors, a PML discretization that matches the mesh topology everywhere would be preferable. Up to now, the most optimal combination in terms of memory requirements and computation time of suitable subgridding schemes combined with adequate PML termination strategies is still an important open research issue.

When embedding a finer mesh within a coarser one, special care has to be taken to adapt the update equations for the fields at the interface of the two meshes. To address this problem, various techniques were developed, such as equivalent circuits of grid discontinuities [5], digital filtering [6], recessed interfaces [7], and Huygens subgridding [8]–[10]. These techniques have drawbacks such as, allowing only odd refinement factors, the need of overlapping meshes or transition regions, requiring the inversion of matrices, as well as late time instability issues or non-symmetrical update equations. Next to those problems, most schemes do not provide a lot of flexibility in terms of refinements nor mesh forms. This often results in mesh specific algorithms and complex update equations.

The work of Peter Monk [11] introduced a scheme with several interesting features: meshes of different resolution only share their boundaries, discrete reciprocity and proven stability. A main restriction is that it only allows a 1:2 refinement. In [12], a finite element approach is used to achieve subgridding, laying out an interesting mathematical framework for subgridding, applicable to a whole range of configurations. Ryan Chilton combined both concepts to one subgridding algorithm [13] with refinement factors $1{:}N$ and later $M{:}N$ ($M, N \in \mathbb{N}_0$). This approach was extended to Body of Revolution FDTD (BOR-FDTD) in [14].

PMLs have been expressed in all kinds of ways. Originally, they were formulated in terms of split-field equations [4]. Later, unsplit formulations were put forward, such as the Maxwellian or Uniaxial Perfectly Matched Layer (UPML) [15] and the non-Maxwellian or Complex Frequency Shifted Perfectly Matched Layer (CFS-PML) [16]. The PML equations have also been expressed in different coordinate systems [17] and even in a coordinate independent way [18]. This last formulation made use of differential forms [19], exactly the foundation of the subgridding algorithm used here.

Other methods, such as the 'Multiresolution Finite Difference' [20] and 'Pseudo Spectral Time Domain' [21] yield longer simulation times and have boundary implementation problems, respectively, and are therefore less suited in the pursuit of a general fast and efficient simulation tool.

In this paper, we present a generalized FDTD subgridding technique for an open simulation domain with the following new features:

- The limited refinement freedom of [13] is extended to allow (almost) arbitrary mesh refinements that are mesh direction independent and this without losing any of the desirable properties such as reciprocity, passivity and stability.
- As (almost) arbitrary mesh refinements are possible, the influences of normal and tangential (both will be defined later on) subgridding can be studied independently of one another.
- To reduce reflections, avoid undesirable side effects such as standing waves and maximize design freedom, mesh refinements are extended towards PMLs. The subgridding possibility will also lead to some new insights into PML implementations.

In a first part, Maxwell's equations in differential geometry form and the corresponding vector representation are briefly repeated. Next, the introduced concepts are expanded to allow subgridding. In a last part, these concepts will be broadened again to include subgridding of a PML.

3.2 Generalized subgridded the Finite Difference Time Domain method for open regions

3.2.1 Discrete differential representation of Maxwell's equations

In absence of sources, the homogeneous Maxwell equations together with the constitutive laws (with $\tau = ct$ and $\Delta\tau = c\Delta t$) are formulated in differential form as

$$-\partial_\tau B = \mathrm{d}E \qquad \partial_\tau D = \mathrm{d}H \tag{3.1a}$$

$$\mathrm{d}B = 0 \qquad \mathrm{d}D = 0 \tag{3.1b}$$

$$H = \star_{\mu_r^{-1}} B \qquad D = \star_{\varepsilon_r} E \tag{3.1c}$$

where d is the exterior derivative operating on a k-form. $\star_{\varepsilon_r}$ and $\star_{\mu_r^{-1}}$ denote the by the permittivity ε_r and permeability μ_r^{-1} scaled version of the hodge-star operator, respectively. E and H are 1-forms whereas B and D are 2-forms. The discretization of the exterior derivative d operating on 1-forms in (3.1a) (corresponding to the curl operator in classical vector notation) results in the curl stencil matrix $\overline{\overline{\boldsymbol{C}}}$, which represents the signed, scaled incidence matrix of the faces in the calculation domain Ω. Scaled, in this context, means that every entry, which correspond to a specific edge and face in $\overline{\overline{\boldsymbol{C}}}$, is divided by that dimension of the cell that does not correspond with the edge or face orientation. This means that if $\overline{\overline{\boldsymbol{C}}}$ is arranged such that the rows correspond first with the B_x, then the B_y and finally with the B_z and that the columns are arranged analogously with the E_x, E_y and E_z. Then nine areas can be distinguished, which are depicted with their scaling factor below

$$\begin{array}{c} \\ B_x \\ B_y \\ B_z \end{array} \begin{array}{c} \begin{array}{ccc} E_x & E_y & E_z \end{array} \\ \begin{bmatrix} 1 & \frac{1}{\Delta z} & \frac{1}{\Delta y} \\ \frac{1}{\Delta z} & 1 & \frac{1}{\Delta x} \\ \frac{1}{\Delta y} & \frac{1}{\Delta x} & 1 \end{bmatrix} \end{array} \tag{3.2}$$

Therefore, (3.1a) can be rewritten in semi-discrete form as

$$-\partial_\tau \boldsymbol{b} = \overline{\overline{\boldsymbol{C}}}\boldsymbol{e} \tag{3.3a}$$

$$\partial_\tau \boldsymbol{e} = \left[\star_{\varepsilon_r}\right]^{-1} \overline{\overline{\boldsymbol{C}}}^T \left[\star_{\mu_r^{-1}}\right] \boldsymbol{b} \tag{3.3b}$$

with the strictly diagonal mass matrices $\left[\star_{\mu_r^{-1}}\right]$ and $[\star_{\varepsilon_r}]$ a mass lumped [13] version of

$$\widetilde{\left[\star_{\mu_r^{-1}}\right]} = \int_{\Omega} \boldsymbol{W}_2 \mu_r^{-1} \boldsymbol{W}_2^T \, \mathrm{d}\Omega \tag{3.4a}$$

$$\widetilde{[\star_{\varepsilon_r}]} = \int_{\Omega} \boldsymbol{W}_1 \varepsilon_r \boldsymbol{W}_1^T \, \mathrm{d}\Omega \tag{3.4b}$$

with $\boldsymbol{W}_k$ Whitney-forms [22] of order k used to discretely expand E and B into $\boldsymbol{e}$ and $\boldsymbol{b}$ using

$$E = \boldsymbol{W}_1^T \boldsymbol{e}$$
$$B = \boldsymbol{W}_2^T \boldsymbol{b}$$

The explicit fully discrete update equations are obtained by replacing the time derivative in by its discrete counterpart using leap frogging.

3.2.2 Arbitrary mesh refinements

Consider a (coarse) uniform background FDTD mesh consisting of fixed cells with constant dimensions $[\Delta x, \Delta y, \Delta z]$ in the $[x, y, z]$ directions. In order to outline our arbitrary mesh refinement strategy we focus on two locally refined meshes M^p and M^q, characterized by absolute refinement vectors $\boldsymbol{N}^p = \left[N_x^p, N_y^p, N_z^p\right]$ and $\boldsymbol{N}^q = \left[N_x^q, N_y^q, N_z^q\right]$, respectively. Hence, the absolute cells sizes in meshes M^p and M^q were reduced to $\left(\Delta x/N_x^p, \Delta y/N_y^p, \Delta z/N_z^p\right)$ and $\left(\Delta x/N_x^q, \Delta y/N_y^q, \Delta z/N_z^q\right)$, respectively. To connect the two meshes at their interface, we introduce a local coordinate system (n, t_1, t_2), with n the normal direction along which the meshes are stitched together, and t_1 and t_2 two tangential orthogonal unit vectors spanning the plane of the interface. The relative mesh refinement when joining M^p and M^q at their interface is characterized by the relative mesh refinement vector $\boldsymbol{\nu}$, defined by

$$\boldsymbol{\nu} = [\nu_n, \nu_{t_1}, \nu_{t_2}] = \left[\max\left(\frac{N_n^p}{N_n^q}, \frac{N_n^q}{N_n^p}\right), \max\left(\frac{N_{t_1}^p}{N_{t_1}^q}, \frac{N_{t_1}^q}{N_{t_1}^p}\right) \max\left(\frac{N_{t_2}^p}{N_{t_2}^q}, \frac{N_{t_2}^q}{N_{t_2}^p}\right)\right]$$

where $\max(x, y)$ represents the maximum of the two arguments x and y. In addition, we introduce $\vartheta = [\{\arg\max(x_i, y_i)\}]$, as the index of the largest of the two elements, for $i \in \{n, t_1, t_2\}$. Now, we outline the general procedure to stitch together M^p and M^q, provided the following two restrictions apply:

1. $\nu_{t_1}, \nu_{t_2} \in \mathbb{N}_0$
2. $\vartheta_{t_1} = \vartheta_{t_2}$

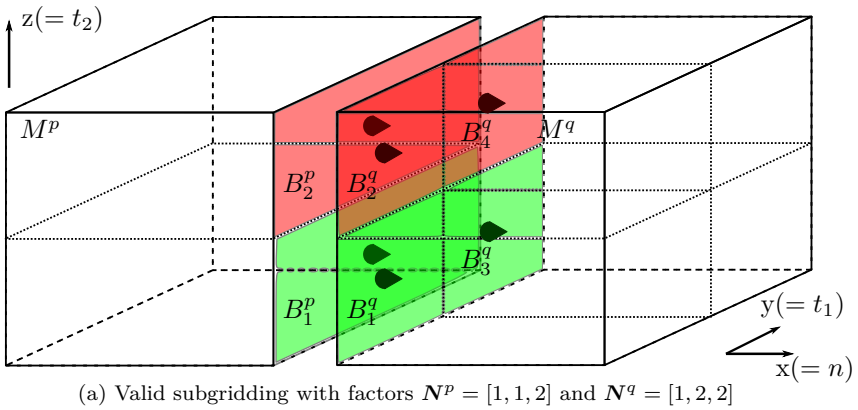

(a) Valid subgridding with factors $\boldsymbol{N}^p = [1, 1, 2]$ and $\boldsymbol{N}^q = [1, 2, 2]$

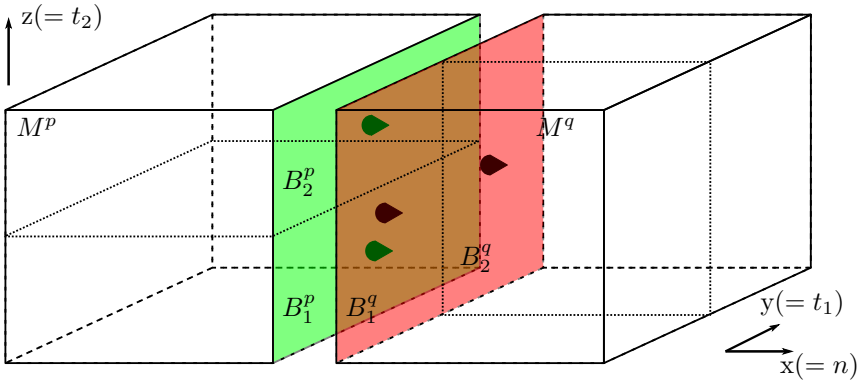

(b) Invalid subgridding with factors $\boldsymbol{N}^p = [1, 1, 2]$ and $\boldsymbol{N}^q = [1, 2, 1]$

Figure 3.1

The first condition can be relaxed to $\mathbb{Q}_0$, as shown in [13]. To better understand the second restriction, consider Fig. 3.1, illustrating a valid (a) and an invalid (b) subgridding scheme. On the one hand, for case (a), meshes M^p, with absolute refinement vector $\boldsymbol{N}^p = [1, 1, 2]$, and M^q, with absolute refinement vector $\boldsymbol{N}^q = [1, 2, 2]$, can be joined, as their relative refinement vector is given by $\boldsymbol{\nu} = [1, 2, 1]$ whereas the index vector is found to be $\boldsymbol{\vartheta} = [\vartheta_n, \vartheta_{t_1}, \vartheta_{t_2}] = [1 \text{ or } 2, 2, 1 \text{ or } 2]$, such that $\vartheta_{t_1} = \vartheta_{t_2} = 2$. The last condition in general implies that each normal B-field of M^p that lies in the subgridding interface has to be a sum of normal B-fields of M^q in the subgridding interface or vice versa. The configuration in Fig. 3.1(a) is valid, because $B_1^p = B_1^q + B_3^q$ and $B_2^p = B_2^q + B_4^q$. On the other hand, for case (b), meshes M^p, with absolute refinement vector $\boldsymbol{N}^p = [1, 1, 2]$, and M^q, with absolute refinement vector $\boldsymbol{N}^q = [1, 2, 1]$, may not be joined, as their relative refinement vector is given by $\boldsymbol{\nu} = [1, 2, 2]$ whereas the index vector is found to be $\boldsymbol{\vartheta} = [\vartheta_n, \vartheta_{t_1}, \vartheta_{t_2}] = [1 \text{ or } 2, 2, 1]$, such that $\vartheta_{t_1} = 2 \neq \vartheta_{t_2} = 1$. Hence, the set-up of Fig. 3.1(b) is not allowed since

$B_1^p \neq B_1^q + B_2^q$ and $B_1^q \neq B_1^p + B_2^p$.

Consider a coarse mesh M^p and a fine mesh M^q. To join both meshes, tangential edges and normal faces that occur twice at the subgridding interface must be eliminated. In particular, the field/induction components occurring at the interface of the fine mesh will be removed. Associate with the edges corresponding to the normal n-, tangential t_1- and tangential t_2-components of the electric field in the meshes M^p and M^q the expansion coefficient vectors $\boldsymbol{e}_n^p$, $\boldsymbol{e}_{t_1}^p$, $\boldsymbol{e}_{t_2}^p$ and $\boldsymbol{e}_n^q$, $\boldsymbol{e}_{t_1}^q$, $\boldsymbol{e}_{t_2}^q$, respectively, and with the faces corresponding to the normal n-, tangential t_1- and tangential t_2-components of the magnetic induction in the meshes M^p and M^q the expansion coefficient vectors $\boldsymbol{b}_n^p$, $\boldsymbol{b}_{t_1}^p$, $\boldsymbol{b}_{t_2}^p$ and $\boldsymbol{b}_n^q$, $\boldsymbol{b}_{t_1}^q$, $\boldsymbol{b}_{t_2}^q$, respectively. The elimination of the fine forms is performed by means of restriction matrices $\overline{\boldsymbol{A}}_e$ and $\overline{\boldsymbol{A}}_b$ (associated with electric fields or magnetic induction components, respectively). Each restriction matrix is a diagonal block matrix, composed by restriction matrices acting on one particular component, hence $\overline{\boldsymbol{A}}_e = \operatorname{diag}\left(\overline{\boldsymbol{A}}_{e,n}, \overline{\boldsymbol{A}}_{e,t_1}, \overline{\boldsymbol{A}}_{e,t_2}\right)$ and $\overline{\boldsymbol{A}}_b = \operatorname{diag}\left(\overline{\boldsymbol{A}}_{b,n}, \overline{\boldsymbol{A}}_{b,t_1}, \overline{\boldsymbol{A}}_{b,t_2}\right)$. Each restriction matrix composing $\boldsymbol{A}_e$ or $\boldsymbol{A}_b$ is constructed in an identical fashion. Let $\boldsymbol{A}_{x,y}$ denote one such matrix for component $y \in \{n, t_1, t_2\}$ of field $x \in \{e, b\}$. Its construction is implemented by means of the following steps:

(i) Let $x_{y,i}^p$ denote the i^{th} expansion coefficient in field/induction component vector $\boldsymbol{x}_y^p$ and $x_{y,j}^q$ the j^{th} expansion coefficient in field/induction component vector $\boldsymbol{x}_y^q$.

(ii) Create a block matrix $\overline{\boldsymbol{A}}'_x = \operatorname{diag}\left(\overline{\mathbf{1}}_{\alpha\times\alpha}, \overline{\mathbf{1}}_{\beta\times\beta}\right)$ with $\overline{\mathbf{1}}_{\alpha\times\alpha}$ and $\overline{\mathbf{1}}_{\beta\times\beta}$ unit matrices of order $\alpha = i_{max}$, equal to the total number of y-oriented edges/faces in M^p, and $\beta = j_{max}$ corresponding to the total number of y-oriented edges/faces in M^q, respectively.

(iii) $\overline{\boldsymbol{A}}'_x[i, i_{max} + j_m] = 1$, $\exists\ \left\{x_{y,j_m}^q\right\} : x_{y,i}^p = \sum\limits_m x_{y,j_m}^q$

(iv) $\overline{\boldsymbol{A}}'_x[i_1, i_{max} + j] = \gamma$, $\overline{\boldsymbol{A}}'_x[i_2, i_{max} + j] = 1-\gamma$, $\exists\ x_{y,i_1}^p, x_{y,i_2}^p \in \left\{\mathrm{nb}_c\left(x_{y,j}^q\right)\right\}$

(v) delete all rows $(i_{max} + j)$ that satisfied either (iii) or (iv).

(vi) now $\overline{\boldsymbol{A}}_x = \overline{\boldsymbol{A}}'_x$

where γ is inversely proportional to the distance between x_{y,i_1}^p and $x_{y,j}^q$ and $\left\{\mathrm{nb}_c\left(x_{y,j}^p\right)\right\}$ is the set containing the coarse form neighbours of fine form $x_{y,j}^q$. Steps (iii) and (iv) are illustrated by Fig. 3.2 and Fig. 3.3, which focus on the discretization of the tangential electric fields at the interface. The labelling is done from top to bottom and left to right (thus $0 \leq i \leq 1$ and $0 \leq j \leq 5$).

The block structure of $\overline{\boldsymbol{A}}_{x,y}$ is explicitly indicated by the dashed subdivisions applied to the matrices below. The construction of $\overline{\boldsymbol{A}}_{e,t_1}$, given the expansion

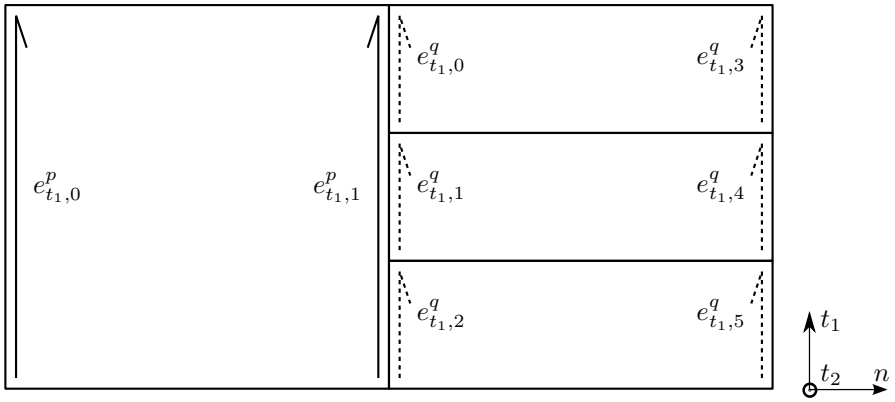

Figure 3.2: Illustration of step (iii): $e^p_{t_1,1} = e^q_{t_1,0} + e^q_{t_1,1} + e^q_{t_1,2}$ (see $\overline{\boldsymbol{A}}_{e,t_1}$)

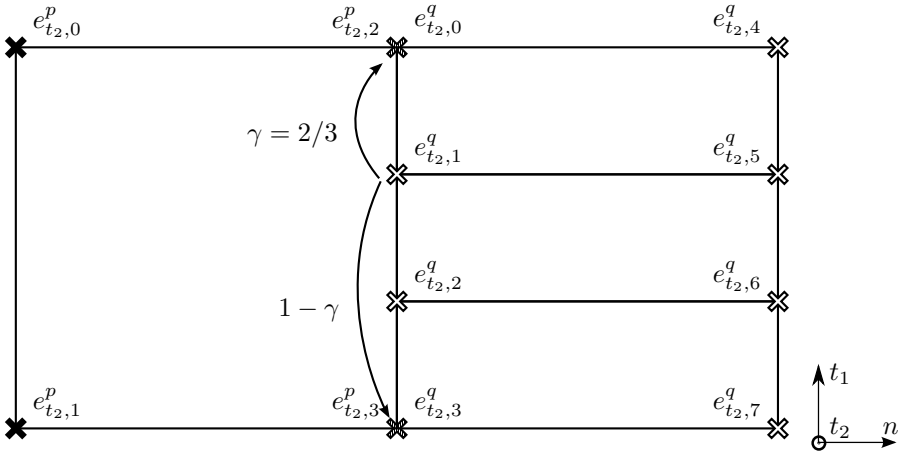

Figure 3.3: Illustration of step (iv): $e^p_{t_2,2}, e^p_{t_2,3} \in \{\mathrm{nb}_c(e^q_{t_2,1})\}$ (see $\overline{\boldsymbol{A}}_{e,t_2}$)

coefficient vectors $\boldsymbol{e}^p_{t_1}$ and $\boldsymbol{e}^q_{t_1}$ in Fig. 3.2, proceeds as follows:

$$\overline{\boldsymbol{A}}'_{e,t_1} \overset{(ii)}{=} \left[\begin{array}{c:c} \overline{\mathbf{1}}_{2\times 2} & \overline{\mathbf{0}}_{2\times 6} \\ \hdashline \overline{\mathbf{0}}_{6\times 2} & \overline{\mathbf{1}}_{6\times 6} \end{array}\right] \overset{(iii)}{\rightarrow} \left[\begin{array}{c:c} \overline{\mathbf{1}}_{2\times 2} & \begin{matrix} 0 & 0 & 0 \\ 1 & 1 & 1 \end{matrix} \quad \overline{\mathbf{0}}_{2\times 3} \\ \hdashline \overline{\mathbf{0}}_{6\times 2} & \begin{matrix} \overline{\mathbf{1}}_{3\times 3} & \overline{\mathbf{0}}_{3\times 3} \\ \overline{\mathbf{0}}_{3\times 3} & \overline{\mathbf{1}}_{3\times 3} \end{matrix} \end{array}\right] \leftarrow \text{delete}$$

$$\overset{(v)}{\rightarrow} \left[\begin{array}{c:cccc} \overline{\mathbf{1}}_{2\times 2} & 0 & 0 & 0 & \overline{\mathbf{0}}_{2\times 3} \\ & 1 & 1 & 1 & \\ \hdashline \overline{\mathbf{0}}_{3\times 2} & \multicolumn{3}{c}{\overline{\mathbf{0}}_{3\times 3}} & \overline{\mathbf{1}}_{3\times 3} \end{array}\right] \overset{(vi)}{=} \overline{\boldsymbol{A}}_{e,t_1}$$

The resulting matrix removes three fine edges, resulting in a mesh with five edges (two coarse ($e^p_{t_1,0}$ and $e^p_{t_1,1}$) and three fine ($e^q_{t_1,3}$ to $e^q_{t_1,5}$)), hence $\overline{\overline{\boldsymbol{A}}}_{e,t_1}$ is a five by eight matrix.

Next, $\overline{\boldsymbol{A}}_{e,t_2}$ is constructed by considering the expansion vectors containing the t_2-oriented electric fields $\boldsymbol{e}^p_{t_2}$ and $\boldsymbol{e}^q_{t_2}$ in Fig. 3.3. The labelling is done again in a top-down/left-right fashion (thus $0 \leq i \leq 3$ and $0 \leq j \leq 7$. Therefore

$$\overline{\boldsymbol{A}}'_{e,t_2} \overset{(ii)}{=} \left[\begin{array}{c:c} \overline{\mathbf{1}}_{4\times 4} & \overline{\mathbf{0}}_{4\times 8} \\ \hdashline \overline{\mathbf{0}}_{8\times 4} & \overline{\mathbf{1}}_{8\times 8} \end{array}\right] \overset{(iv)}{\rightarrow} \left[\begin{array}{c:cccc:c} & 0 & 0 & 0 & 0 & \\ & 0 & 0 & 0 & 0 & \\ \overline{\mathbf{1}}_{4\times 4} & 1 & {}^2\!/_3 & {}^1\!/_3 & 0 & \overline{\mathbf{0}}_{4\times 4} \\ & 0 & {}^1\!/_3 & {}^2\!/_3 & 1 & \\ \hdashline & \multicolumn{4}{c}{\overline{\mathbf{1}}_{4\times 4}} & \overline{\mathbf{0}}_{4\times 4} \\ \overline{\mathbf{0}}_{8\times 4} & & & & & \\ & \multicolumn{4}{c}{\overline{\mathbf{0}}_{4\times 4}} & \overline{\mathbf{1}}_{4\times 4} \end{array}\right] \leftarrow \text{delete}$$

$$\overset{(v)}{\rightarrow} \left[\begin{array}{c:cccc:c} & 0 & 0 & 0 & 0 & \\ & 0 & 0 & 0 & 0 & \\ \overline{\mathbf{1}}_{4\times 4} & 1 & {}^2\!/_3 & {}^1\!/_3 & 0 & \overline{\mathbf{0}}_{4\times 4} \\ & 0 & {}^1\!/_3 & {}^2\!/_3 & 1 & \\ \hdashline \overline{\mathbf{0}}_{4\times 4} & \multicolumn{4}{c}{\overline{\mathbf{0}}_{4\times 4}} & \overline{\mathbf{1}}_{4\times 4} \end{array}\right] \overset{(vi)}{=} \overline{\boldsymbol{A}}_{e,t_2}$$

The resulting eight by twelve matrix illustrates that the restriction operator reduced the number of redundant edges from twelve to eight (four coarse ($e^p_{t_2,0}$ to $e^p_{t_2,3}$) and four fine edges ($e^q_{t_2,4}$ to $e^q_{t_2,7}$)).

At this point both meshes M^p and M^q have their own tailored discrete version of the discrete derivative, $\overline{\overline{\boldsymbol{C}}}_p$ and $\overline{\overline{\boldsymbol{C}}}_q$. To connect both meshes a single matrix $\overline{\overline{\boldsymbol{C}}}$ has to be constructed that operates as the discrete derivative for the combined mesh.

First construct a block matrix $\overline{\overline{\boldsymbol{C}}}_{pq}$ as below

$$\overline{\overline{\boldsymbol{C}}}_{pq} = \begin{bmatrix} \overline{\overline{\boldsymbol{C}}}_p & 0 \\ 0 & \overline{\overline{\boldsymbol{C}}}_q \end{bmatrix}$$

(3.3) may still be used, provided that $\overline{\overline{\boldsymbol{C}}}$ is redefined as

$$\overline{\overline{\boldsymbol{C}}} = \overline{\overline{\boldsymbol{A}}}_2^{+} \overline{\overline{\boldsymbol{C}}}_{pq} \overline{\overline{\boldsymbol{A}}}_1^{T}$$

which can be proven, using the fact that $\overline{\boldsymbol{A}}_1\overline{\boldsymbol{C}}_{pq}^T = \overline{\boldsymbol{C}}^T\overline{\boldsymbol{A}}_2$ and where $\overline{\boldsymbol{A}}^+$ is the Moore-Penrose (or pseudo) inverse of $\overline{\boldsymbol{A}}$. Moreover, as a result of introducing $\overline{\boldsymbol{A}}_1$ and $\overline{\boldsymbol{A}}_2$, (3.4) changes to

$$\widetilde{\left[\star_{\mu_r^{-1}}\right]} = \overline{\boldsymbol{A}}_2\left(\int_\Omega \boldsymbol{W}_2\mu_r^{-1}\boldsymbol{W}_2^T\,\mathrm{d}\Omega\right)\overline{\boldsymbol{A}}_2^T \tag{3.5a}$$

$$\widetilde{[\star_{\varepsilon_r}]} = \overline{\boldsymbol{A}}_1\left(\int_\Omega \boldsymbol{W}_1\varepsilon_r\boldsymbol{W}_1^T\,\mathrm{d}\Omega\right)\overline{\boldsymbol{A}}_1^T \tag{3.5b}$$

3.3 A subgridded Uniaxial Perfectly Matched Layer

In case of a UPML, the semi-discrete Maxwell equations (3.3) are modified corresponding to [23]:

$$-\partial_\tau\overline{\boldsymbol{\Lambda}}_2\boldsymbol{b} = \overline{\overline{\boldsymbol{C}}}\boldsymbol{e} \tag{3.6a}$$

$$\partial_\tau\overline{\boldsymbol{\Lambda}}_1\boldsymbol{e} = [\star_{\varepsilon_r}]^{-1}\overline{\boldsymbol{C}}^T\left[\star_{\mu_r^{-1}}\right]\boldsymbol{b} \tag{3.6b}$$

where matrices $\overline{\boldsymbol{\Lambda}}_1$ and $\overline{\boldsymbol{\Lambda}}_2$ were introduced as the result of a complex coordinate transformation of the field variables explained in section 1.5.1, section 2.3.1 and [24].

$$\boldsymbol{u}_i \to \tilde{\boldsymbol{u}}_i = \int_0^{\boldsymbol{u}_i} s_i(\eta)\,\mathrm{d}\eta \qquad\qquad i \in \{0,1,2\}, \tag{3.7}$$

with $\boldsymbol{u}^i$ the i^{th}component of the base spanning the space. Following [16] s_i is defined by

$$s_i = \begin{cases} \kappa_i + \frac{\sigma_i}{j\omega\varepsilon_0} & \text{PML absorbs in } i\text{-direction} \\ 1 & \text{PML does not absorbs in } i\text{-direction} \end{cases} \tag{3.8}$$

The stretching matrices are then constructed as follows:

$$\tilde{\Lambda}_1[m,r] = \sum_\ell\ \hat{y}[m]\cdot\overline{\boldsymbol{\phi}}(\ell)\cdot\hat{y}[r]\int_{\Omega_\ell}\boldsymbol{W}_1[m]\boldsymbol{W}_1^T[r]\,\mathrm{d}\Omega \tag{3.9}$$

$$\tilde{\Lambda}_2[m,r] = \sum_\ell\ \hat{y}[m]\cdot\overline{\boldsymbol{\phi}}(\ell)\cdot\hat{y}[r]\int_{\Omega_\ell}\boldsymbol{W}_2[m]\boldsymbol{W}_2^T[r]\,\mathrm{d}\Omega \tag{3.10}$$

where the sum extends over all cells ℓ of the simulation domain, with $\{\Omega_\ell\}$ the volume of cell ℓ and $\hat{y}[m]$ the unit vector pointing in the direction of the edge associated to the Whitney form of first order $\boldsymbol{W}_1[m]$ or of second order $\boldsymbol{W}_2[m]$. The diagonal matrix $\overline{\overline{\boldsymbol{\phi}}}$ is defined by

$$\overline{\overline{\boldsymbol{\phi}}}(\ell) = \begin{bmatrix} \frac{s_1(\ell)\, s_2(\ell)}{s_0(\ell)} & 0 & 0 \\ 0 & \frac{s_2(\ell)\, s_0(\ell)}{s_1(\ell)} & 0 \\ 0 & 0 & \frac{s_0(\ell)\, s_1(\ell)}{s_2(\ell)} \end{bmatrix} \tag{3.11}$$

which is the typical constitutive law of a uniaxial anisotropic medium representing the UPML.

We can now apply the general subgridding scheme of section 3.2.2 in a straightforward manner. By applying the same approach that lead to (3.5b) starting from $[\star_{\varepsilon_r}]$, the stretching matrices $\overline{\overline{\boldsymbol{\Lambda}}}_1$ and $\overline{\overline{\boldsymbol{\Lambda}}}_2$ in case of subgridding are transformed into

$$\Lambda_1[j,k] = \sum_r \sum_m A_1[j,m] \tilde{\Lambda}_1[m,r] A_1^T[r,k] \tag{3.12}$$

$$\Lambda_2[j,k] = \sum_r \sum_m A_2[j,m] \tilde{\Lambda}_2[m,r] A_2^T[r,k] \tag{3.13}$$

If necessary mass lumping can be used to make the resulting matrices diagonal. In the PML regions, normal subgridding can now be embedded in the standard PML equations. From this point on, the classical discretization of the time derivative as in section 2.3.1, [25], [26].

3.4 Numerical results

We now carefully test the theory previously outlined in section 3.2. First, we evaluate the generalized subgridding scheme of section 3.2.2 for a closed simulation domain, terminated by Perfect Electric Conductor (PEC) walls. Ideally, the subgridding should not cause any reflections at interfaces between meshes with different densities. A wave should travel from one submesh to another as if the refinement of the meshes did not matter. In practice, different refinement factors results in different grid densities and, hence, a different dispersion relation. Therefore, non-physical reflections may occur at the mesh interface. Second, we move to the open regions terminated by PMLs. We again study the reflection caused by the combination of the PML discretization and the subgridding of the PML region. Finally, the technique is put to the test in two realistic configurations: a differential stripline pair and a differential microstrip interconnect.

3.4.1 Spurious reflections caused by subgridding

Although the theory is formulated in 3D, we will study reflection at a subgridding interface in a 2D configuration (the z-dimension will be invariable), in order to reduce calculation times and memory requirements. Two meshes M^1 and M^2 consisting of 330×420 and 90×420 coarse cells, respectively (Fig. 3.4(a)), are stitched together, with the x-direction being the normal direction and the y-direction being the tangential direction. The coarse discretization length equals $\Delta x = \Delta y = \Delta = 0.001\,\text{mm}$ whereas $\Delta\tau(= c\Delta t)$ is chosen to be $288.675\,\mu\text{m}$, 90 % of the Courant-Friedrichs-Lewy-limit for a with $\boldsymbol{\nu} = [2, 2, 2]$ subgridded mesh. The configuration is excited by a soft Gaussian pulse (GP) line source in the z-direction. The source is located in M^1, in the middle of the simulation domain, at coarse position $E_z^{[210,210]}$. Its time dependent definition is

$$GP(t) = A_0 \nu_x \nu_y e^{-\frac{2(t-t_0 2)}{\sigma^2}}$$

with $A_0 = 0.25$, $t_0 = 200\,\Delta t$ and $\sigma = 66\,\Delta t$. ν_x and ν_y are needed to scale the pulse's amplitude correctly in the fine mesh, as otherwise the amplitude of the soft source depends on the mesh discretization. The parameters are chosen in such a way that most of the frequency content of the GP lies below 10 GHz. At this upper frequency, the chosen discretization still provides 30 samples per wavelength. An observer is placed one coarse cell next to the source, co-located with the field $E_z^{[211,210]}$

Two sets of four different set-ups are considered (Fig. 3.4). For each set, a uniform reference configuration is defined. On the one hand, grid refinement (Fig. 3.4(a-d)) is studied, starting from a fully coarse mesh 'cRef' (Fig. 3.4(a)). On the other hand, grid unrefinement (Fig. 3.4(e-h)) is evaluated, using a fully fine mesh with $\boldsymbol{\nu} = [2, 2, 1]$, 'fRef' (Fig. 3.4(e)), as a starting point. We investigate the reflections induced by refining or unrefining the mesh in the normal ((b) and (f)), tangential ((c) and (g)) or both ((d) and (h)) directions.

Time domain results

First, a simulation over a very large number of time steps $100\,000\,\Delta t$ is performed, while the energy as a function of time is stored, to test for instabilities. All tests resulted in constant energy, proving the stability of the proposed scheme. A formal proof can be derived, based on the theory outlined in [13].

Next, the results of subgridding are investigated in more detail. To do so, the solution of the corresponding coarse (Fig. 3.4(a)) or fine (Fig. 3.4(e)) reference configuration is subtracted from the simulation results of the refined or unrefined configuration in the normal (cases (b) and (f)), tangential (cases (c) and (g)) or both (cases (d) and (h)) directions. Afterwards the logarithm is taken to emphasize the differences. By subtracting the reference solution, any reflection on the PEC-walls is removed. Around $800\,\Delta t$ a first spurious signal, caused by the reflection at the subgridding interface between M^1 and M^2, is observed.

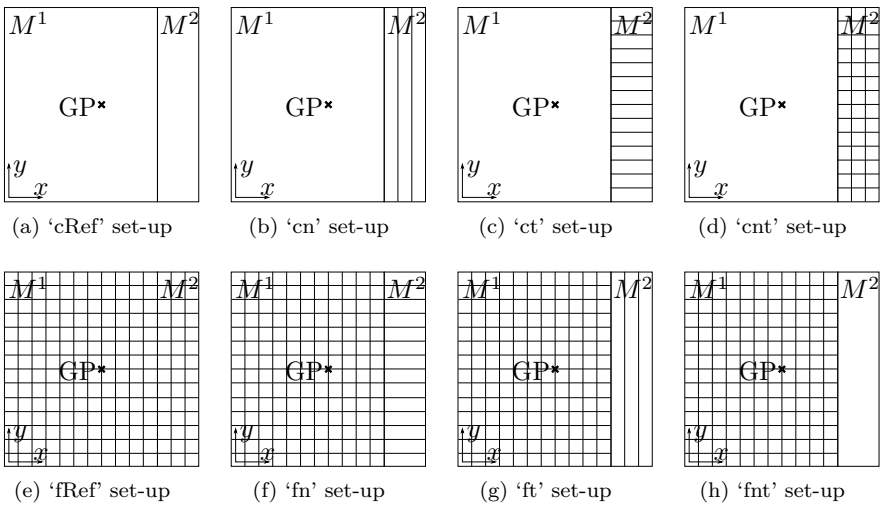

(a) 'cRef' set-up (b) 'cn' set-up (c) 'ct' set-up (d) 'cnt' set-up

(e) 'fRef' set-up (f) 'fn' set-up (g) 'ft' set-up (h) 'fnt' set-up

Figure 3.4: Different subgridding schemes for meshes M^1 and M^2 consisting of 330×420 and 90×420 coarse cells, respectively. M^1 has a fixed coarse (cases (a) to (d)) or fine (cases (e) to (h)) discretization. M^2 is (un)refined in either the normal (cases (b) and (f)), tangential (cases (c) and (g)) or both (cases (d) and (h)) directions.

One can clearly see in Fig. 3.5 that the tangential subgridding introduces a significantly smaller error than normal subgridding. The spurious signals around $1455\,\Delta t$ (second reflection) are caused by the errors from the first subgridding interface crossing, followed by a reflection at the PEC-wall and then a second subgridding interface crossing. This explains why the second reflection is larger than the first. Note first that, overall, the errors are extremely small and second, the peak of the second reflection of the tangential subgridding is reached only $\approx 300\,\Delta t$ after the peak of normal subgridding.

Frequency domain results

First, to convert the time domain (TD) signal to the frequency domain (FD), a 4096 point Discrete Fourier Transform (DFT) is calculated, but only the first 1400 data points are used, to ensure the effect of only one subgridding interface crossing is taken into account. Next, a cut-off frequency f_c is set at 15 GHz. Frequencies above f_c are not of interest given the increasing grid dispersion error and, hence, will not be shown in the graphs. Finally, the error is normalized to A_0, (the amplitude of the GP), to remove the influence of the input amplitude.

A quick look at the errors in the frequency domain confirms the TD result of section 3.4.1. It is clear from Fig. 3.6 that tangential subgridding introduces

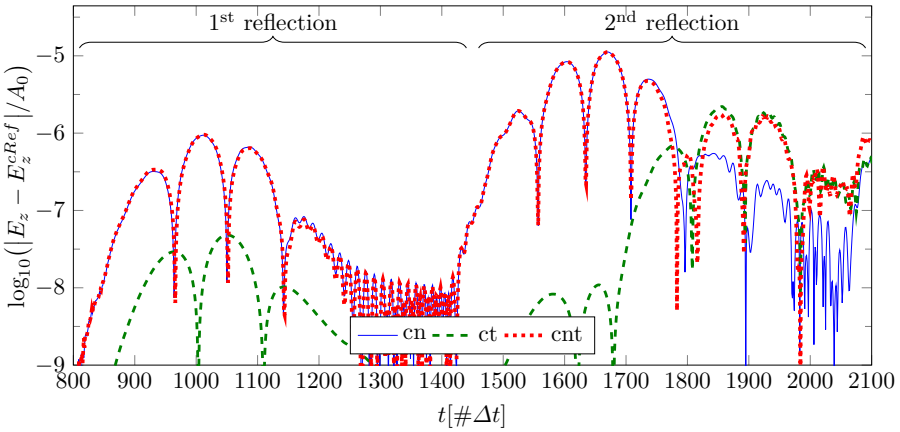

(a) wave travelling from coarse mesh M^1 ($\boldsymbol{N}^1 = [1, 1, 1]$) to a refined mesh M^2

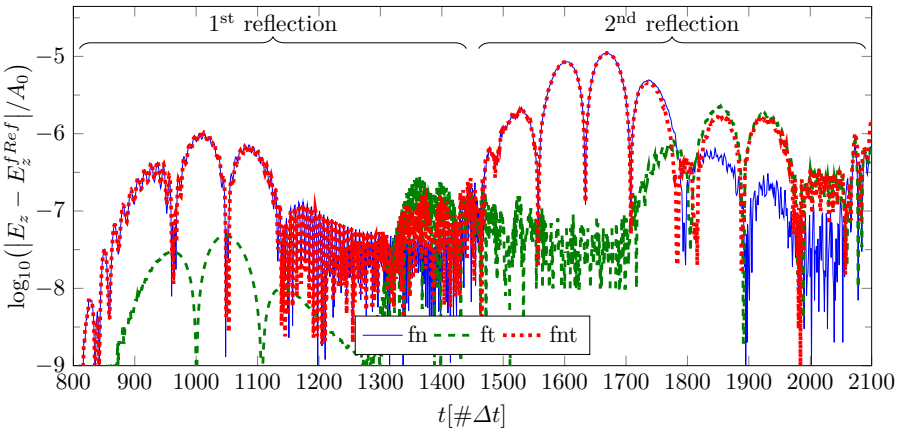

(b) wave travelling from a fine mesh M^1 ($\boldsymbol{N}^1 = [2, 2, 1]$) to an unrefined mesh M^2

Figure 3.5: Errors normalized to A_0 (the amplitude of the GP) in the time domain due to reflections of a wave at the interface of a uniform mesh (M^1) and a subgridded mesh (M^2), (un)refined in the normal (label 'n'), tangential (label 't') or (label 'nt') both directions.

significantly less errors than normal subgridding.

One can almost observe no difference between the absolute error induced by refining a coarse mesh (Fig. 3.6(a)) and the error induced by unrefining a fine mesh (Fig. 3.6(b)). This indicates that the used method is reciproque. Only around 10 GHz, the error induced by unrefining a fine mesh (Fig. 3.6(b)) in the tangential direction is significantly larger than the error seen when refining a

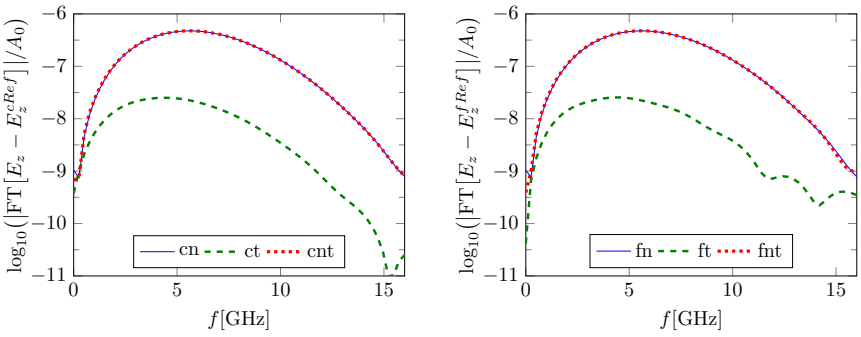

(a) Coarse reference mesh

(b) Fine reference mesh

Figure 3.6: Error normalized to A_0 (the amplitude of the GP) as a function of frequency when a wave travels from a uniform mesh (M^1) to a subgridded mesh (M^2), in case of (un)refining M^2 in the normal ('n'), tangential ('t') or both ('nt') directions.

coarse mesh (Fig. 3.6(a)). This occurs because at higher frequencies the fine mesh suffers from less grid dispersion than the coarse mesh. In the coarse mesh, these higher frequencies experience a dispersion relation that differs from the free space one and, therefore, additional errors occur. Note also that adding tangential subgridding to normal subgridding has almost no influence on the value of the error.

In general, we conclude that the subgridding algorithm is found to be stable and only introduces very small errors into the calculation domain. If the configuration under study allows for it, only using tangential subgridding results in smaller errors.

3.4.2 Spurious reflections introduced by PMLs combined with subgridding

Although not as perfect as predicted by the theory [27], in practice, PMLs give nowadays the best numerical approximation of free space for FDTD algorithms. Known advantages as low reflections, close application to scatterers, ... come with two major disadvantages, the calculation and storage cost. The PML update equation is computationally much more expensive than a standard update equation and a PML-field needs more storage than a standard field, next to the fact that extra layers of cells have to be added to the simulation domain. This means, on the one hand, that for small problems, relatively, a rather large part of the calculation time is spent within the PML. On the other hand, for large problems, the relative calculation effort decreases, but calculation time nevertheless increases noticeably as does the needed memory.

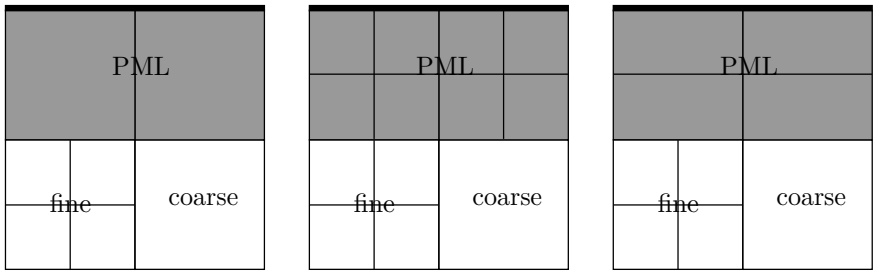

(a) Coarse PML (b) Fine PML (c) PML that is unrefined in tangential direction

Figure 3.7: Schematic representation of different ways to terminate a non-uniform mesh (consisting of a fine and coarse submesh) at the top by applying a combination of refined and coarse PEC-backed PMLs (grey).

So far, PMLs have only been applied to uniform meshes. Therefore, the origin of reflections is the numerically imperfectly matched PML and, as a consequence, a part of the incident wave that is not totally absorbed. Applying a PML to a non-uniform mesh opens up some opportunities to reduce simulation time and memory consumption. First, one could add a uniform PML directly to the non-uniform mesh (Fig. 3.7(a) and Fig. 3.7(b)). This means that at points, the PML will be well matched to the mesh, but at other points additional mismatch will be introduced by the difference between the mesh and the PML discretization. Next, one could add a (few) uniform layer(s) of cells to the non-uniform mesh and then apply a PML. This means that reflections caused by subgridding and reflections caused by the PML are spatially separated, but this also means that additional storage and calculation efforts are needed. Finally one could apply a non-uniform PML (Fig. 3.7(c)), tailored to be less resource consuming.

We consider two configurations to investigate the termination by a PML when using a non-uniform mesh. Consider a 2D simulation geometry, discretized by a coarse mesh consisting of 420×240 cells in the middle and two fine meshes, both consisting of 420×90 coarse cells refined by a factor $\boldsymbol{\nu} = [2, 2, 1]$, on top and below this centre region, as depicted in Fig. 3.8. The same GP as in section 3.4.1 is used to excite the configuration at its centre and again the observer is placed one coarse cell away from the source. We now create two kinds of open simulation domains by extending the configuration of Fig. 3.8 by means of PMLs. The first simulation domain is closed at the bottom and top by PEC plates and open at the side walls, by extending the mesh of these walls with a one-dimensional PML that only absorbs in the x-direction. For the second configuration, PMLs are added at all four walls, providing absorption in both the x and y-direction. To terminate the open regions, we apply a 5-layer

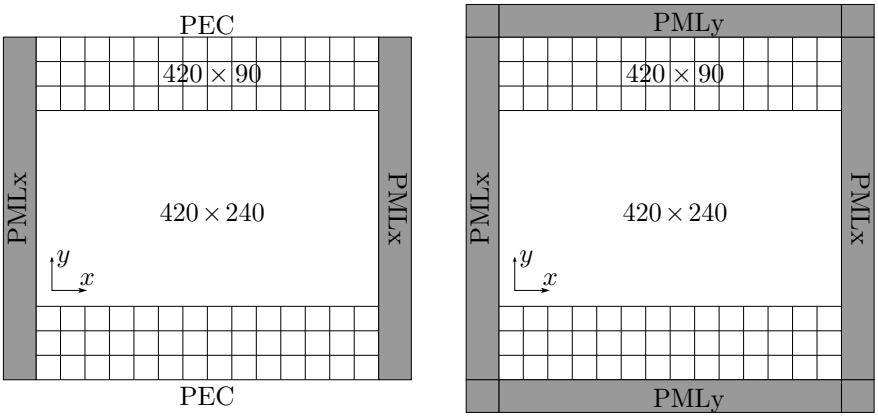

(a) mesh with a PML in one direction (b) mesh with a PML in two directions

Figure 3.8: Subgridded mesh with overall size 420×420, consisting of a coarse inner mesh of size 420×240 and two outer meshes of size 420×90. All dimensions are expressed in coarse cells.

PML, implemented as a UPML [15], with σ-profile as in (1.22) and with

$$\sigma_{opt} = \frac{-(m+1)\ln R(0)}{2\eta \cdot 5\Delta}$$

where $R(0) = \mathrm{e}^{-8}$ is the round-trip reflection for normal incidence and η is the impedance of free space. Each PML layer spans a single coarse mesh cell. In order to clearly isolate the effect of the subgridding, the same profile with $R(0) = \mathrm{e}^{-8}$ is preserved also in case of a refined PML. The following types of subgridded PML are tested: a coarse-cell PML ($\boldsymbol{\nu} = [1, 1, 1]$, labelled [111]), a fine-cell PML ($\boldsymbol{\nu} = [2, 2, 1]$, labelled [221]) and a mixed-cell PML (labelled [dyn], having refinement factors $\boldsymbol{\nu} = [2, 1, 1]$ when absorbing in the x-direction, $\boldsymbol{\nu} = [1, 2, 1]$ when absorbing in the y-direction and $\boldsymbol{\nu} = [2, 2, 1]$ when absorbing in both directions in corner regions). Note that the PML is unrefined in the tangential direction with respect to the fine mesh it interfaces with and that the discretization of the corner regions is refined in the normal direction with respect to the PMLs only absorbing in one single direction.

A reference solution is computed by enlarging the mesh in such a way that no reflections will enter the initial mesh for at least $3000\,\Delta t$.

PML in one direction

Consider Fig. 3.8(a), where the mesh is terminated by a coarse-cell ([111], Fig. 3.7(a)), fine-cell ([221], Fig. 3.7(b)) and mixed-cell ([dyn], Fig. 3.7(c)) PML. The error signals with respect to the reference solution are plotted in

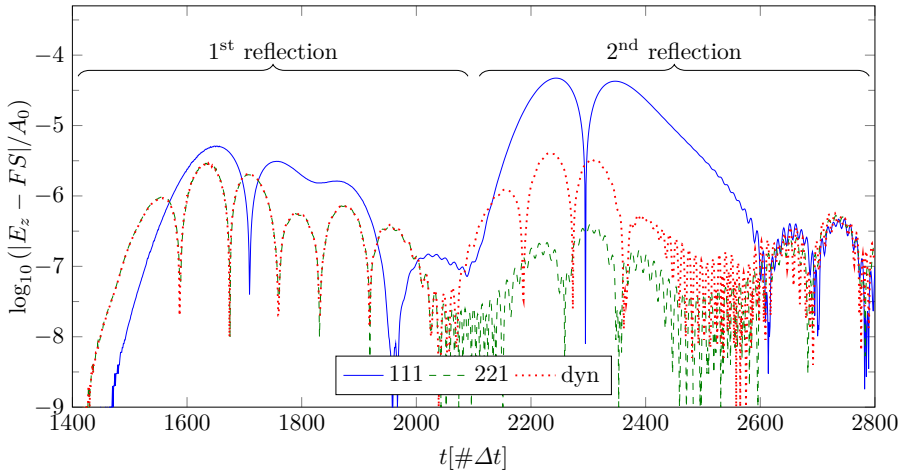

Figure 3.9: Errors normalized to A_0 (the amplitude of the Gaussian pulse) as a function of time in a slab-like mesh (Fig. 3.8(a)), terminated by differently discretized PMLs absorbing in one direction. The first reflection starts at $\pm 1450\,\Delta t$, the second at $\pm 2100\,\Delta t$.

Fig. 3.9. One can distinguish two main reflections. The first reflection occurs between $1450\,\Delta t$–$2000\,\Delta t$, the time required for the wave to travel one round trip distance of $d \approx 420\,\Delta$ between the source/observer and the PML. One notices that the fine-cell ([221]) and mixed-cell ([dyn]) PMLs exhibit the same level of error, clearly outperforming the coarse-cell ([111]) PML. The second reflection, taking place between $2100\,\Delta t$–$2700\,\Delta t$ ($d \approx 595\,\Delta \approx 420 \cdot \sqrt{2}\,\Delta$) is caused by reflections at the corner points of the mesh, where the wave penetrated the PMLs under a much more oblique angle. For this reflection, the fine-cell ([221]) PML performs best, followed by the mixed-cell ([dyn]) and coarse-cell ([111]) PMLs. After the second reflection, all subgridded PMLs settle for the same error level.

PML in two directions

In this section the mesh is terminated by the same PMLs, but now in both x and y-direction (Fig. 3.8(b)). The errors generated by the different subgridded PML terminations with respect to the reference solution are shown in Fig. 3.10. The first reflection from both the x- and y-directed PML reach the observer at the same time instant and will add up. The second reflection from the corners should, ideally, be absent, since it should be absorbed by the corner PML. Given the results obtained for a 1D PML, this is clearly expected for a fine-cell PML ([221]) and since all configurations in this section have fine-cell corner regions, we obtain very small second reflections for the PML configurations considered

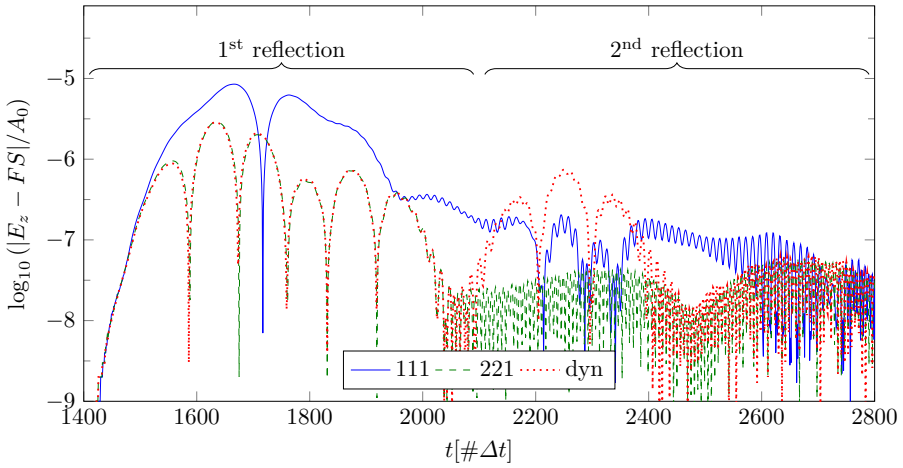

Figure 3.10: Errors normalized to A_0 (the amplitude of the GP) as a function of time in a slab-like mesh (Fig. 3.8(b)), terminated by differently discretized PMLs absorbing in two directions. The first reflection starts at $\pm 1450\,\Delta t$, the second at $\pm 2100\,\Delta t$.

here. Fine-cell PMLs ([221]) outperform coarse-cell ones ([111]), as the latter additionally suffer from subgridding errors, but no relevant second reflection is observed. The mixed-cell PMLs ([dyn]) exhibit a similar performance as the fine-cell PMLs ([221]), yet they suffer from higher reflections from the corner regions. This is due to the fact that for the mixed-cell PMLs, the corner region is differently subgridded with respect to the x- and y-directed PML.

We conclude that coarse-cell PMLs ([111]) use the least resources, but suffers from additional subgridding errors at the interface between the fine mesh and the PML. The fine-cell PMLs ([221]) perform best at the cost of a significant increase in computation time and memory resources. The mixed-cell PML ([dyn]) provides a good balance between accuracy and computational cost and is, therefore, the PML of our choice.

3.4.3 Application example: differential stripline pair and microstrip interconnects

Finally, we simulate an asymmetric differential stripline pair (Fig. 3.11(a)) and a differential microstrip (Fig. 3.11(b)) as realistic application examples that make use of both subgridding of the mesh and a PML as absorbing boundary condition. The interconnects were designed on a lossless *Nelco® N4000-13 SI* High-Speed Multifunctional Epoxy Laminate with relative permittivity $\varepsilon_r = 3.2$. All conductors are assumed to be perfect electrically conducting.

First, we test the convergence of the solution in terms of the applied uniform

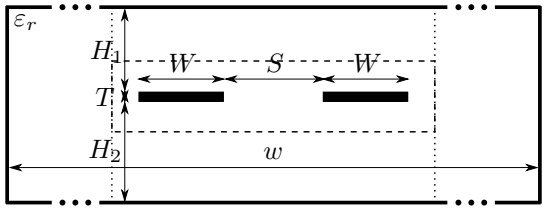

(a) Asymmetric differential stripline pair

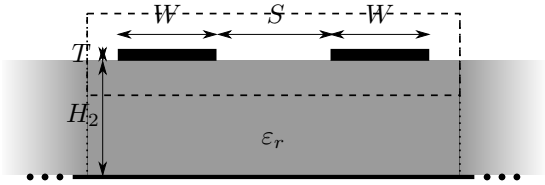

(b) differential microstrip

Figure 3.11: Asymmetric differential stripline pair and differential microstrip with dimensions $H_1 = 150\,\mu m$, $H_2 = 180\,\mu m$, $T = 18\,\mu m$, $W = 151\,\mu m$, $S = 175\,\mu m$, $w = 2477\,\mu m$, in/on a *Nelco® N4000-13 SI* substrate with permittivity $\varepsilon_r = 3.2$.

discretization, by simulating the configurations once with discretization vector $\Delta_1 = [15.1\,\mu m, 507.8\,\mu m, 9.0\,\mu m]$ and once with $\Delta_2 = [12.6\,\mu m, 507.8\,\mu m, 6.0\,\mu m]$. These vectors were chosen such that the inner conductors of the stripline pair and the microstrip consist of an adequate number of cells, as further discussed, and because these discretizations yield an exact representation of the conductors with a minimal error on the spacing between the conductors. For the remainder of this paper, results will be given with respect to Δ_1, since the convergence experiments yielded consistent results for both discretizations. In the experiments, the differential pair is excited by a sinusoidal current with a frequency of 10 GHz. To reduce artefacts in the frequency domain, the sinusoidal excitation is ramped over five periods (or about $21\,000\,\Delta t$, with respect to Δ_1). During the simulations, both the current along and the voltage difference between the two conductors is measured over the full length of the stripline pair. The resulting time-domain vectors were then Fourier-transformed and subsequently matched to standing waves by means of the matrix pencil method [28]. By dividing the voltage by the current, the characteristic impedance of the stripline pair and the microstrip is determined. The obtained value will be compared to the impedance (later referred to as Z_{ref}) as obtained by a dedicated MoM technique [29], [30], developed to derive the modal parameters of high-frequency interconnects with arbitrary cross-sections.

Asymmetric differential stripline pair

The configuration of the stripline pair with uniform discretization Δ_1 yields conductors of size $10 \times y \times 2$ cells, spaced twelve cells apart. Now, a first reference solution is simulated without the use of a PML absorbing boundary conditions. Instead 1 mm (or 66 cells) of substrate material was added to the left and the right of the inner conductor. The calculation domain was then terminated with PEC-walls at both sides. It was verified that terminating with PEC-walls 1 mm away from the conductors has minimal influence on the simulation results. This results in a calculation domain of $164 \times y \times 39$ cells. We now investigate the accuracy, by which the matrix pencil method is able to extract the modal parameters, as a function of the number of cells in the longitudinal direction y. We try to establish a good trade-off between the accuracy and the speed of the method. The initial setting for the reference simulation of the stripline pair corresponds to a length of three wavelengths (or 99 cells) and a duration of $100\,000\,\Delta t$. The robustness of the matrix pencil method then allows for a reduction in the stripline pair length to only $\lambda/4$. Further reducing the length below eight cells, results in rank-deficient matrices in the matrix pencil method. A second set of experiments reduces the number of time steps. Table 3.1 shows that the best results (with respect to Δ_1) are obtained for a simulation time of $50\,000\,\Delta t$, while the worst results were obtained when simulating up to only $12\,500\,\Delta t$. As expected, results deteriorate for shorter stripline pairs simulated for shorter amounts of time. Remarkable is, though, that the results for a quarter wavelength stripline pair are distinctly better than, for example, a stripline pair of a third of a wavelength. Almost all simulations yield characteristic impedances that lie within $2\,\Omega$ of the reference value.

Next we step-wise introduce subgridding and the subgridded PML boundary condition. First, we unrefine the standard (fine) reference solution (referred to as Z_{fine}), by limiting the fine mesh to a selected core region (within the dashed box in Fig. 3.11(a) and corresponding to 'region 1' in Fig. 3.12. The dimensions are indicated in Table 3.2). 'Region 1' extends two and three coarse cells to the sides and to the top and bottom of the conductors, respectively. The remainder of the calculation domain is unrefined with factors $\nu = [4, 1, 3]$ (Z_{sub}), resulting in the mesh dimension listed in Table 3.2. In a second step, all cells left and right of the core region containing the conductors, being left and right of the dotted line in Fig. 3.11(a), are replaced by a five cell PML. The stripline pair was simulated using both a coarse- ($Z_{[111]}$) and mixed-cell ($Z_{[dyn]}$) PML. The dimensions are again tabulated in Table 3.2.

Table 3.3 contains the number of cells, the number of field components, the calculation time as well as the calculated impedances. It can be seen that a distinct reduction in cells (and therefore field components) with a factor 5.8 has resulted in a time reduction with factor 4.8. Table 3.3 shows that all obtained impedances do not deviate much from Z_{ref} and even less from Z_{fine}.

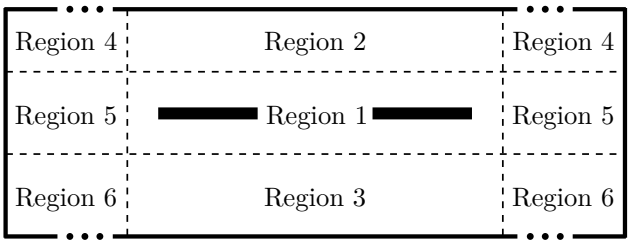

Figure 3.12: Subgridding regions to discretize the differential stripline pair

Differential microstrip

The configuration of the microstrip is identical to the one of the stripline pair with two obvious differences: the conductors are located on top of a *Nelco® N4000-13 SI* substrate with thickness $H_2 = 180\,\mu\text{m}$ and above the conductors there is an open free space region (or a PML in the simulation). This means that PMLs are now applied at the left, the right and above the dotted box (see Fig. 3.11(b)). The distances kept from the conductors is three coarse cells at both the left and right side and five cells at the top. The coarse mesh, when applied, starts two coarse cells below the conductors. Table 3.4 presents a comparison between the impedance obtained by our in-house MoM technique, by the new subgridded FDTD techniques using a uniform fine mesh with matching fine-cell PML (Z_{pml}) and a non-uniform mesh with both coarse-cell and mixed-cell PML ($Z_{[111]}$ and $Z_{[dyn]}$, respectively). All simulations are obtained from a $\lambda/3$-long microstrip simulated for $100\,000\,\Delta t$.

The results presented above clearly demonstrate the stability of the proposed schemes. The obtained results hardly differ from a FDTD reference solution and are in good agreement with the results obtained from the in-house MoM tool. Important here is that equally accurate results are obtained using 5.8 times less field components. This resulted in a significant speed-up (by a factor of 4.6) of the simulations.

3.5 Conclusion

In this paper, a framework for a stable, reciprocal and passive arbitrary subgridding procedure was presented. The consequences in terms of non physical reflections were studied and found to be of minor impact. In addition, a subgridding scheme for PMLs was proposed. It was found that an adequately subgridded PML provides a good balance between accuracy and calculation time. By means of two realistic examples, it was shown that the proposed strategies yield accurate results using significantly less resources both in terms of memory requirements and simulation time.

$Z_{ref} = 49.21\,\Omega$		length [λ] (length [cells])				
		3.0 (99)	1.0 (33)	0.5 (17)	0.3 (10)	0.25 (8)
time [$\#\Delta t$]	100k	48.634	48.572	48.604	48.747	48.394
	50k	49.217	49.266	49.209	49.266	48.817
	25k	47.947	47.035	47.216	45.693	50.130
	12.5k	48.428	44.612	43.183	53.036	49.760
	6.25k	48.430	49.162	44.408	66.089	47.577

Table 3.1: Influence of the stripline pair length and the number of time steps on the calculation of the characteristic impedance Z.

	fine	unrefined	PML $_{[111]}$	PML $_{[dyn]}$
region 1	56×15	56×15	56×15	56×15
region 2	56×12	14×4	14×4	14×4
region 3	56×15	14×5	14×5	14×5
region 4	56×12	13×4	5×4	20×4
region 5	56×15	13×5	5×5	20×5
region 6	56×15	13×5	5×5	20×5

Table 3.2: actual mesh dimension (y-dimension suppressed), of the different simulated configurations

	Z_{ref}	Z_{fine}	Z_{sub}	Z_{pml}	$Z_{[111]}$	$Z_{[dyn]}$
# cells/y		6396	1330	2772	1106	1526
calc. time [s]		120 341	28 626	56 092	25 934	37 734
$\text{gain}_{\text{cells}}$		1.0	4.8	2.3	5.8	4.2
$\text{gain}_{\text{time}}$		1.0	4.2	2.1	4.8	3.2
$Z[\Omega]$	49.21	48.634	47.534	48.645	49.500	49.506
$\text{rel.err}_{Z_{ref}}$ [%]	0	1.17	3.41	1.15	0.59	0.6
$\text{rel.err}_{Z_{fine}}$ [%]	1.18	0	2.26	0.02	1.78	1.79

Table 3.3: Aggregated results for the asymmetric differential stripline pair

	Z_{ref}	Z_{pml}	$Z_{[111]}$	$Z_{[dyn]}$
$Z[\Omega]$	67.85	68.399	67.644	67.328
$\text{rel.err}_{Z_{ref}}$ [%]	0	0.81	0.3	0.77
$\text{rel.err}_{Z_{fine}}$ [%]	0.8	0	1.1	1.57

Table 3.4: Aggregated results for the differential microstrip

References

[1] T. Cuyckens, H. Rogier, and D. De Zutter, "Numerical assessment of the combination of subgridding and the perfectly matched layer grid termination in the finite difference time domain method", *International Journal of Numerical Modelling: Electronic Networks, Devices and Fields*, vol. 27, no. 3, pp. 527–543, 2014, issn: 1099-1204. [Online]. Available: `http://dx.doi.org/10.1002/jnm.1932`.

[2] T. Cuyckens, H. Rogier, and D. De Zutter, "Numerical assessment of the combination of subgridding and PML grid termination in FDTD", in *9th International Symposium on Electric and Magnetic Fields*, 2013.

[3] K. S. Yee, "Numerical solution of initial boundary value problems involving maxwell's equations in isotropic media", *IEEE Transactions on Antennas and Propagation*, vol. 14, no. 3, pp. 302–307, May 1966, issn: 0018-926X.

[4] J.-P. Bérenger, "A Perfectly Matched Layer for the Absorption of Electromagnetic Waves", *Journal of Computational Physics*, vol. 114, pp. 185–200, Oct. 1994.

[5] K. M. Krishnaiah and C. J. Railton, "Passive equivalent circuit of FDTD: an application to subgridding", *Electronics Letters*, vol. 33, no. 15, pp. 1277–1278, Jul. 1997, issn: 0013-5194.

[6] B. Donderici and F. L. Teixeira, "Improved FDTD subgridding algorithms via digital filtering and domain overriding", *IEEE Transactions on Antennas and Propagation*, vol. 53, no. 9, pp. 2938–2951, Sep. 2005, issn: 0018-926X.

[7] K. Xiao, D. J. Pommerenke, and J. L. Drewniak, "A Three-Dimensional FDTD Subgridding Algorithm With Separated Temporal and Spatial Interfaces and Related Stability Analysis", *IEEE Transactions on Antennas and Propagation*, vol. 55, no. 7, pp. 1981–1990, Jul. 2007, issn: 0018-926X.

[8] J.-P. Bérenger, "A Huygens Subgridding for the FDTD Method", *IEEE Transactions on Antennas and Propagation*, vol. 54, no. 12, pp. 3797–3804, Dec. 2006, issn: 0018-926X.

[9] J.-P. Bérenger, "Three dimensional Huygens subgridding for FDTD", in *APSURSI '09. IEEE Antennas and Propagation Society International Symposium, 2009*, Jun. 2009, pp. 1–4.

[10] J.-P. Bérenger, "Extension of the FDTD Huygens Subgridding Algorithm to Two Dimensions", *IEEE Transactions on Antennas and Propagation*, vol. 57, no. 12, pp. 3860–3867, Dec. 2009, issn: 0018-926X.

[11] P. Monk, "Sub-Gridding FDTD Schemes", *Applied Computational Electromagnetics Journal*, vol. 11, no. 1, pp. 37–46, Mar. 1996.

[12] N. V. Venkatarayalu, R. Lee, Y.-B. Gan, and L.-W. Li, "A Stable FDTD Subgridding Method Based on Finite Element Formulation With Hanging Variables", *IEEE Transactions on Antennas and Propagation*, vol. 55, no. 3, pp. 907–915, Mar. 2007, issn: 0018-926X.

[13] R. A. Chilton, "H-, P-, And T-Refinement Strategies For The Finite-Difference-Time-Domain (FDTD) Method Development Via Finite-Element (FE) Principles", PhD thesis, Ohio State University, 2008.

[14] W. Tierens and D. De Zutter, "BOR-FDTD subgridding based on finite element principles", *Journal of Computational Physics*, vol. 230, no. 12, pp. 4519–4535, Jun. 2011, issn: 0021-9991.

[15] Z. S. Sacks, D. M. Kingsland, R. Lee, and J.-F. Lee, "A perfectly matched anisotropic absorber for use as an absorbing boundary condition", *IEEE Transactions on Antennas and Propagation*, vol. 43, no. 12, pp. 1460–1463, Dec. 1995, issn: 0018-926X.

[16] M. Kuzuoglu and R. Mittra, "Frequency dependence of the constitutive parameters of causal perfectly matched anisotropic absorbers", *IEEE Microwave and Guided Wave Letters*, vol. 6, no. 12, pp. 447–449, Dec. 1996, issn: 1051-8207.

[17] F. L. Teixeira and W. C. Chew, "PML-FDTD in cylindrical and spherical grids", *IEEE Microwave and Guided Wave Letters*, vol. 7, no. 9, pp. 285–287, Sep. 1997, issn: 1051-8207.

[18] B. He and F. L. Teixeira, "Differential Forms, Galerkin Duality, and Sparse Inverse Approximations in Finite Element Solutions of Maxwell Equations", *IEEE Transactions on Antennas and Propagation*, vol. 55, no. 5, pp. 1359–1368, May 2007, issn: 0018-926X.

[19] B. Donderici and F. L. Teixeira, "Conformal Perfectly Matched Layer for the Mixed Finite Element Time-Domain Method", *IEEE Transactions on Antennas and Propagation*, vol. 56, no. 4, pp. 1017–1026, Apr. 2008, issn: 0018-926X.

[20] M. Krumpholz and L. P. B. Katehi, "MRTD: new time-domain schemes based on multiresolution analysis", *Microwave Theory and Techniques, IEEE Transactions on*, vol. 44, no. 4, pp. 555–571, Apr. 1996, issn: 0018-9480.

[21] Q. Liu, "The pseudospectral time-domain (PSTD) method: a new algorithm for solutions of Maxwell's equations", in *IEEE Antennas and Propagation Society International Symposium, 1997*, vol. 1, Jul. 1997, pp. 122–125.

[22] H. Whitney, *Geometric Integration Theory*, M. Morse and A. W. Tucker, Eds. Princeton University Press, 1957.

[23] F. L. Teixeira and W. C. Chew, "Differential Forms, Metrics, and the Reflectionless Absorption of Electromagnetic Waves", *Journal of Electromagnetic Waves and Applications*, vol. 13, no. 5, pp. 665–686, 1999.

[24] W. C. Chew, J.-M. Jin, and E. Michielssen, "Complex coordinate stretching as a generalized absorbing boundary condition", *Microwave and Optical Technology Letters*, vol. 15, no. 6, pp. 363–369, Aug. 1997, issn: 1098-2760.

[25] S. D. Gedney, "An anisotropic perfectly matched layer-absorbing medium for the truncation of FDTD lattices", *IEEE Transactions on Antennas and Propagation*, vol. 44, no. 12, pp. 1630–1639, Dec. 1996, issn: 0018-926X.

[26] A. Taflove and S. C. Hagness, *Computational Electrodynamics: The Finite-Difference-Time-Domain Method*, 2nd. Artech House, 2000, ISBN 1-58053-076-1.

[27] J.-P. Bérenger, "Perfectly matched layer for the FDTD solution of wave-structure interaction problems", *IEEE Transactions on Antennas and Propagation*, vol. 44, no. 1, pp. 110–117, Jan. 1996, issn: 0018-926X.

[28] T. K. Sarkar and O. Pereira, "Using the matrix pencil method to estimate the parameters of a sum of complex exponentials", *IEEE Antennas and Propagation Magazine*, vol. 37, no. 1, pp. 48–55, Feb. 1995, issn: 1045-9243.

[29] D. De Zutter and L. Knockaert, "Skin Effect Modeling Based on a Differential Surface Admittance Operator", *IEEE Transactions on Microwave Theory and Techniques*, vol. 53, no. 8, pp. 2526–2538, Aug. 2005, issn: 0018-9480.

[30] D. De Zutter, H. Rogier, L. Knockaert, and J. Sercu, "Surface Current Modelling of the Skin Effect for On-Chip Interconnections", *IEEE Transactions on Advanced Packaging*, vol. 30, no. 2, pp. 342–349, May 2007, issn: 1521-3323.

Part II

Wireless Power Transmission over Ultra Wide Band links

Ultra Wide Band links, antennas, systems, ... are characterized by large bandwidth requirements. They differ from narrow band systems by the fact that the system characteristics cannot be assumed to be frequency independent, i.e. constant within the considered frequency interval. The frequency dependence of involved quantities complicates the description of such systems. Therefore tools to develop or simulate such systems have to take into account these more involved models.
Wireless Power Transmission studies the amount of power available at a receiver given an amount of power sent by a transmitter. In this part, Ultra Wide Band and Wireless Power Transmission are introduced, and a tool to simulate Wireless Power Transmission over Ultra Wide Band links in a multipath environment is presented.

4

Introduction to Ultra Wide Band and Wireless Power Transmission

★ ★ ★

Even though antenna operation is governed by Maxwell's equations, usually there is no need to describe them at such a low level. The behaviour of antenna links can be described based on antenna figures of merit and channel characteristics. This chapter aims to provide an introduction to the necessary terminology, characteristics and equations concerning (Ultra Wide Band) antennas and transmissions. Almost naturally these concepts will lead to Wireless Power Transmission over (wide band) antenna links.

Wireless communications can be characterized by a very simple scheme, consisting of a transmitter, a wireless channel and a receiver (see Fig. 4.1). In the field of electromagnetism, this translates to an antenna system transforming 'electrical data' into electromagnetic waves, which, in turn, are interpreted by a receiving antenna. In order to model and simulate the complete system, it is key to understand and model each component as accurately and as detailed as possible. It is important to note that, from this point, on electromagnetic quantities are used in their conventional (not normalized) form, as first introduced in (1) in the introduction (p. 3) of this dissertation.

4.1 Antenna characteristics

A transmitting antenna can be described based on its electrical equivalent circuit as depicted in Fig. 4.1(a). The antenna is driven by a source voltage V_s and a

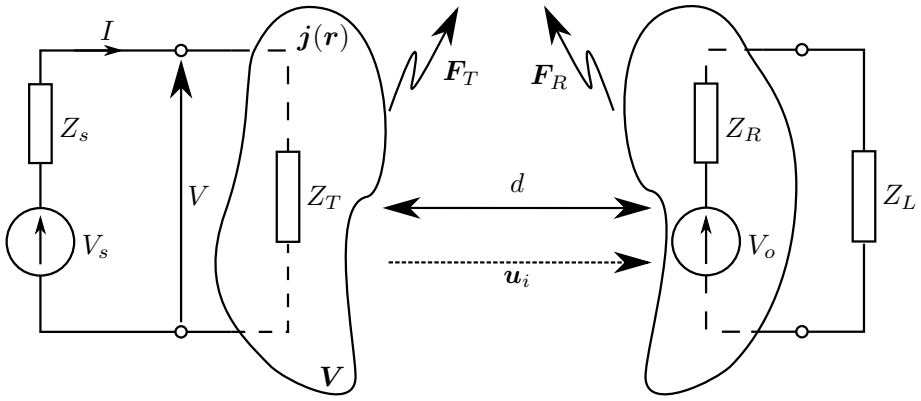

(a) Equivalent electric scheme of an antenna in transmit mode.

(b) Equivalent electric scheme of an antenna in receive mode

Figure 4.1: Antenna link consisting of a transmitting antenna (a) and a receiving antenna (b) separated by a distance d. The transmitting antenna, characterized by its internal impedance Z_T, is driven by a source V_s with internal impedance Z_s, resulting in a current I injected into the terminals of the antenna or a current density $\boldsymbol{j}(\boldsymbol{r})$ in the antenna itself. The receiving antenna, characterized by its internal impedance Z_R, is excited by an electromagnetic wave, resulting in an open circuit voltage V_o, which can be (partially) dissipated in the load Z_L

current I through the antenna terminals. This produces a voltage V over those terminals and induces an electrical current density $\boldsymbol{j}$ in the antenna structure, which then radiates an electrical field into space. If one observes the electric field far enough away from the antenna, being in the far field, at a distance of at least $2d^2/\lambda$ (with d the largest dimension of the antenna), assymptotic behaviour of the electric field in a point $\boldsymbol{r} = r\boldsymbol{u}_r$ can be expressed as

$$\begin{aligned}\lim_{kr\to\infty} \boldsymbol{E}(\boldsymbol{r}) &\sim \jmath 2\pi f \boldsymbol{u}_r \times \Big(\boldsymbol{u}_r \times \boldsymbol{N}(\theta,\phi)\Big)\frac{\mathrm{e}^{-\jmath kr}}{r} \\ &\sim I\boldsymbol{F}(\theta,\phi)\frac{\mathrm{e}^{-\jmath kr}}{r} \end{aligned} \tag{4.1}$$

with $\boldsymbol{F}(\theta,\phi)$ the far field vector for a unit current associated with a specific antenna, I the terminal current and

$$\boldsymbol{N}(\theta,\phi) = \frac{\mu}{4\pi}\int_V \boldsymbol{j}(\boldsymbol{r}')\mathrm{e}^{\jmath \boldsymbol{k}\circ\boldsymbol{r}'}\,\mathrm{d}V' \tag{4.2}$$

with $\boldsymbol{r}'$ as in Fig. 4.2

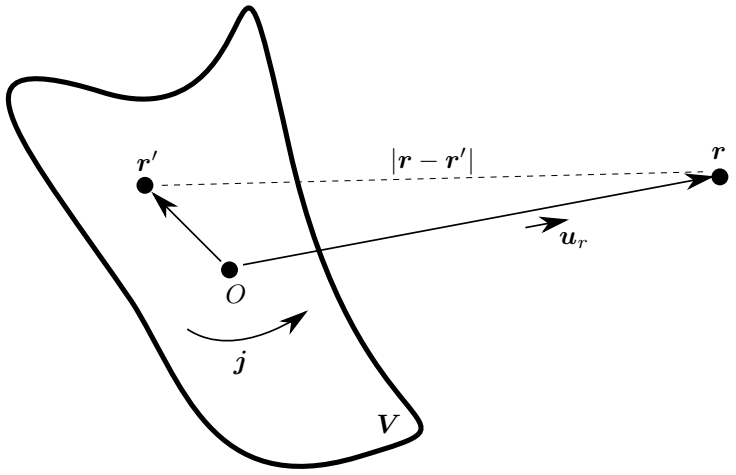

Figure 4.2: Relevant quantities for the calculation of the far field, under the assumption that $|\boldsymbol{r}| \approx |\boldsymbol{r} - \boldsymbol{r}'|$

The antenna itself is characterized by its internal impedance $Z_T = R_T + \jmath X_T$ with

$$R_T = \frac{1}{\eta} \int_{\Omega} \left|\boldsymbol{F}(\theta, \phi)\right|^2 \mathrm{d}\Omega \tag{4.3}$$

$$X_T = -\frac{2\pi f}{|I|^2} \int_{V} \left(\varepsilon |\boldsymbol{E}|^2 - \mu |\boldsymbol{H}|^2\right) \mathrm{d}V \tag{4.4}$$

Based on this far field vector, some antenna characteristics can be defined. Most importantly, the directivity, $D(\theta, \phi)$, and the gain, $G(\theta, \phi)$ are given by

$$D(\theta, \phi) = \frac{4\pi |I|^2 |\boldsymbol{F}(\theta, \phi)|^2}{P_r} = \frac{4\pi |I|^2 |\boldsymbol{F}(\theta, \phi)|^2}{\int\limits_{\Omega} |I\boldsymbol{F}(\theta, \phi)|^2 \,\mathrm{d}\Omega} = \frac{4\pi |\boldsymbol{F}(\theta, \phi)|^2}{\eta R_T}$$

$$G(\theta, \phi) = \frac{4\pi |I|^2 |\boldsymbol{F}(\theta, \phi)|^2}{P_t}$$

They are related through the radiation efficiency ϵ by $G(\theta, \phi) = \epsilon D(\theta, \phi)$ ($P_r = \epsilon P_t$) with P_r the radiated power and P_t the total power.

Analogously, an equivalent circuit can be derived for an antenna in receive mode (see Fig. 4.1(b)). For an antenna in receive mode, the same characteristics with the same definitions as an antenna in transmit mode can be defined. Another important parameter for the receive antenna is the open circuit voltage V_o

$$V_o = \frac{-2\jmath\lambda}{\eta} \boldsymbol{F}_R(-\boldsymbol{u}_i) \circ \boldsymbol{E}^{inc} \tag{4.5}$$

with η the impedance of free space, $-\boldsymbol{u}_i$ the direction of the incident plane wave and $\boldsymbol{E}^{inc}$ the plane wave itself.

4.2 Power transmission between two antennas

In this section, the real part of an impedance $\Re Z_A$ will be denoted as R_A, where $_A$ will be $_R$, $_T$, $_L$ and $_S$ for the impedance of the receive antenna, transmit antenna, the load and the source, respectively. Combining both the transmitting and receiving circuit results in

$$V_L = \frac{Z_L}{Z_L + Z_R} \frac{-2\jmath\lambda}{\eta} \Big(\boldsymbol{F}_R(-\boldsymbol{u}_i) \circ \boldsymbol{F}_T(\boldsymbol{u}_i) \Big) \frac{V_s}{Z_s + Z_T} \tag{4.6}$$

The power dissipated in the load can be derived, based on the equivalent receiving circuit, as

$$P_L = \frac{1}{2} \frac{R_L}{|Z_L + Z_R|^2} |V_o|^2 \tag{4.7}$$

It can be proven that for $Z_L = Z_R^*$ the power dissipated in Z_L is maximised, where β^* denotes the complex conjugate of β. The maximum power is then given by

$$P_{max} = \frac{1}{8} \frac{|V_0|^2}{R_R} \tag{4.8}$$

This means that

$$P_L = M_R P_{max} = \frac{4 R_L R_R}{|Z_L + Z_R|^2} |V_o|^2 \tag{4.9}$$

with M_R the mismatch factor of the receive antenna. Analogously, the maximum power delivered by the source to Z_T equals

$$P_{T,max} = \frac{1}{8} \frac{|V_s|^2}{R_s} \tag{4.10}$$

and

$$P_T = M_T P_{T,max} = \frac{4 R_T R_s}{|Z_s + Z_T|^2} |V_s|^2 \tag{4.11}$$

P_L can be rewritten using (4.1), (4.3), (4.5), (4.10) and (4.11), resulting in

$$P_L = M_T \cdot G_T \left(\frac{c}{4\pi d f} \right)^2 Q_{RT} \cdot G_R \cdot M_R \cdot P_s \tag{4.12}$$

with d the distance between the two antennas and Q_{RT} the polarisation mismatch factor defined as

$$Q_{RT} = \frac{\big| \boldsymbol{F}_T(\boldsymbol{u}) \circ \boldsymbol{F}_R(-\boldsymbol{u}) \big|^2}{\big| \boldsymbol{F}_R(-\boldsymbol{u}) \big|^2 \big| \boldsymbol{F}_T(\boldsymbol{u}) \big|^2} \tag{4.13}$$

(4.12) is called the Friis transmission formula [1]. It is by this formula that far field Wireless Power Transmission (WPT) is largely governed, since it describes the maximum power available at the receiver, given two antennas, a channel set-up and a certain transmit power. Important to notice is the inverse of the free space path loss in Friis' formula. The free space path loss (PL) is defined by

$$\mathrm{PL} = \left(\frac{4\pi df}{c}\right)^2 \tag{4.14}$$

This clearly indicates the spherical spreading of the power with increasing distance as well as the influence of the frequency on the available power.

4.3 Ultra Wide Band systems

As just mentioned before, the Friis transmission formula is already frequency dependent. But when using Ultra Wide Band (UWB) antennas, not only the path loss is frequency dependent, every other quantity involved becomes frequency dependent as well and Friis transmission formula changes to

$$P_L = M_T(f) \cdot G_T(f) \left(\frac{c}{4\pi df}\right)^2 Q_{RT}(f) \cdot G_R(f) \cdot M_R(f) \cdot P_s \tag{4.15}$$

This more general version of Friis' transmission formula, also applies to narrow band antennas. Although with narrow band antennas one assumes the quantities involved do not change (much) over the considered frequency interval, and are thus assumed constant.

The additional frequency dependence in (4.15) is caused by the large bandwidth of UWB antennas, in so far that the narrow band approximation used in (4.12) becomes invalid. To 'officially' qualify as a UWB antenna, according to the Federal Communications Commission (FCC) [2], an antenna has to meet at least one of the following criteria:

- Its absolute bandwidth[1] has to exceed 500 MHz
- Its relative bandwidth[2] has to exceed 20 %

A lot of designs exist for UWB antennas. The following is an incomplete list of well-known, often encountered (classes of) antennas. A special class of UWB antennas consists of the frequency independent antennas such as the log-spiral

[1] the absolute bandwidth is defined as $f_H - f_L$, with f_H, f_L the upper and lower boundary of the antenna's operating range, respectively

[2] the relative bandwidth is defined as $2\dfrac{f_H - f_L}{f_H + f_L}$, with f_H, f_L the upper and lower boundary of the antenna's operating range, respectively

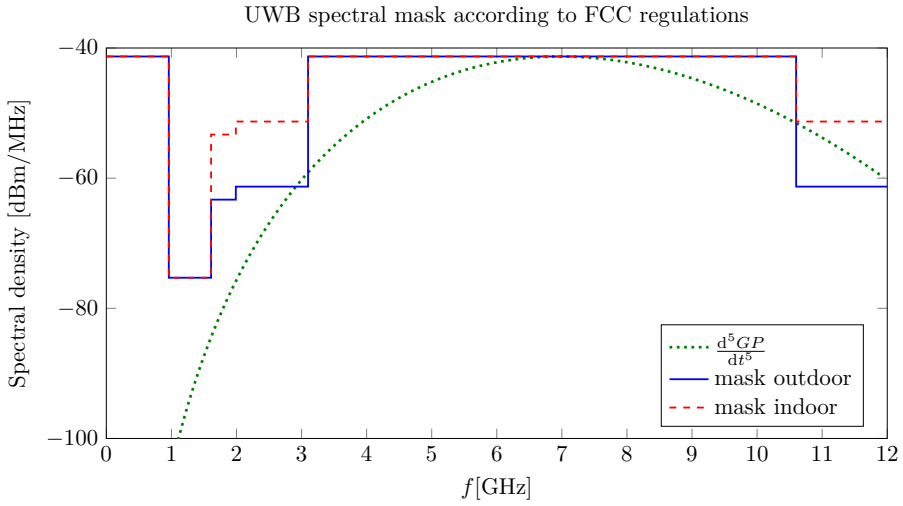

Figure 4.3: UWB spectral mask according to FCC regulations for both indoor (red dashed) and outdoor (blue solid) environments. Within the unlicensed frequency band 3.1 GHz–10.6 GHz, the spectral density is limited to 41.3 dBm/MHz. As an example, the fifth derivative of a Gaussian pulse (GP), which fits the indoor mask very well, is depicted as well

antenna [3], biconical antennas [4] and the almost frequency independent log-periodic antennas [5]. Another class consists of the wide band horns or rigged horns [6]. During our wide band measurements, this type of horn was used as a reference antenna. Finally, some UWB antennas can be described as linear time invariant systems, characterized by their impulse response. Good impulse antennas, have a sharp peak in their response and exhibit no or very limited ringing (i.e. a very short impulse response). Good examples are the Vivaldi antenna [5], [7] and the PulseOn® 200 [8] as used for the measurements and the simulations in this thesis. The use of very short impulses, heavily reduces the chance of pulse overlap in multipath environments, thereby almost eliminating multipath fading. The pulse used in section 5.4 lasts 6.1 ns, with the bulk of the pulse only lasting about 4 ns. Meaning there is no, or almost no interference if the path length difference between the direct and a reflected path is larger than 1.8 m and 1.2 m, respectively.

Regulators have provided an unlicensed frequency band for UWB applications. In 2002, the American FCC [2] approved unlicensed use between 3.1 GHz and 10.3 GHz, with a spectral mask of −41.3 dBm/MHz, as depicted in Fig. 4.3. In 2007, the European Commission [9] followed in the FCC's footsteps by opening the frequency band between 6 GHz and 8.5 GHz for unlicensed use. Because the FCC's band is wider, it allows for more applications, and since it is in place longer, most research is concentrated around it. The enforced low power

requirements result in very limited interference with other systems. It also makes UWB an ideal technology for Body Area Networks (BANs), because of the confined range of the radiation and the limited Specific Absorption Rate (SAR). The spectral mask, mentioned above, also regulates the type of impulse antenna that can be used. For example, the fifth derivative of a Gaussian pulse (GP), defined by

$$\frac{\mathrm{d}^5 GP(t)}{\mathrm{d}t^5} = \frac{A_0}{\sqrt{2\pi}\sigma^6}\left(-\left(\frac{t}{\sigma}\right)^5 + 10\left(\frac{t}{\sigma}\right)^3 - 15\left(\frac{t}{\sigma}\right)\right)\mathrm{e}^{-t^2/2\sigma^2} \tag{4.16}$$

with $\sigma = 51\,\mathrm{ps}$ and A_0 a normalisation constant to fit the mask, approximates the mask very well (Fig. 4.3). Therefore any antenna with this impulse response is well suited for UWB applications under the FCC guidelines.

References

[1] H. Friis, "A Note on a Simple Transmission Formula", *Proceedings of the IRE*, vol. 34, no. 5, pp. 254–256, May 1946, issn: 0096-8390.

[2] Federal Communications Commission, *Revision of Part 15 of the Commission's Rules Regarding Ultra-Wideband Transmission Systems*, 2002. [Online]. Available: http://hraunfoss.fcc.gov/edocs_public/attachmatch/FCC-02-48A1.pdf.

[3] J. Dyson, "The equiangular spiral antenna", *Antennas and Propagation, IRE Transactions on*, vol. 7, no. 2, pp. 181–187, Apr. 1959, issn: 0096-1973.

[4] J. Morrow, "Shorted biconical antenna for ultra-wideband applications", in *Radio and Wireless Conference, 2003. RAWCON '03. Proceedings*, Aug. 2003, pp. 143–146.

[5] W. Sorgel, C. Waldschmidt, and W. Wiesbeck, "Transient responses of a Vivaldi antenna and a logarithmic periodic dipole array for ultra wideband communication", in *Antennas and Propagation Society International Symposium, 2003. IEEE*, vol. 3, Jun. 2003, 592–595 vol.3.

[6] Rhode & Schwartz, *Datasheet double ridged UWB horn HF906*. [Online]. Available: http://cdn.rohde-schwarz.com/pws/dl_downloads/dl_common_library/dl_brochures_and_datasheets/pdf_1/HF906_brief_e.pdf.

[7] P. Gibson, "The Vivaldi Aerial", in *Microwave Conference, 1979. 9th European*, Sep. 1979, pp. 101–105.

[8] Time Domain, *Datasheet PulseOn 200*. [Online]. Available: http://www.timedomain.com/datasheets/TD_Broadspec_Antenna.pdf.

[9] Commission of the European Communities, *Commission Decision of 21/11/2007 on allowing the use of the radio spectrum for equipment using ultra-wideband technology in a harmonized manner in the Community*, 2007. [Online]. Available: http://ec.europa.eu/information_society/policy/%20radio_spectrum/ref_documents.

[10] H. Rogier, *Antenna's en Propagatie*. 2012.

[11] D. De Zutter and F. Olyslager, *Toegepast Elektromagnetisme*. 2005.

[12] J. Hesselbarth and R. Vahldieck, *Advanced Antennas*. 2009.

[13] W. Wiesbeck, G. Adamiuk, and C. Sturm, "Basic Properties and Design Principles of UWB Antennas", *Proceedings of the IEEE*, vol. 97, no. 2, pp. 372–385, Feb. 2009, issn: 0018-9219.

5

Framework for the simulation of Wireless Power Transmission over Ultra Wide Band links in intricate propagation environments

Submitted to International Journal of Numerical Modelling: Electronic Networks, Devices and Fields

★ ★ ★

In this contribution a modular framework for Ultra Wide Band Wireless Power Transmission applications is presented. The goal of this work is to simplify the study of wireless links, including antenna characteristics, and the power transferred over them in body-centric, multipath propagation environments. To achieve this goal, antenna links are partitioned in black box models for all elementary building blocks, such as antenna transfer functions, propagation channels, active components and more. They can afterwards be recombined as one sees fit. The recombination allows for accurate simulation of intricate systems. For small examples, considerable speed and memory gains were observed, when comparing the antenna link simulation to a free standing antenna simulation. The simulation of the recombination using the proposed framework runs semi-instantaneous. For larger examples, the simulated solution is obtained within seconds.

5.1 Introduction

Within the broad field of Wireless Power Transmission (WPT) research, different (overlapping) subdivisions can be identified. Based on the transmitter-receiver distance, a separation can be made into near field and far field WPT. Being independent of transmitter-receiver distance, efficiency is a key specification and therefore a lot of research efforts focus on very efficient rectifier circuits [1] and rectennas [2]. In this manuscript we will focus on far field WPT, especially on the effect of the antennas and the propagation environment.

Historically, research into far field WPT boomed in the *'60s* and *'70s*. Important mile stones were the powering of a remote model helicopter by William Brown using radio waves and space agencies investigating the feasibility of solar power harvesting in space and beaming it back to earth. After a cool down period, research in WPT is booming again with more practical research topics such as the remote powering of hard to reach sensor networks [3], cable-free desks, near field wireless charging standards [4], [5] and (passive) Radio Frequency IDentification (RFID) tags [1].

To
in order not to disturb other transmission systems or to create high power density hot spots. Ultra Wide Band (UWB)[1] systems provide such low power transmission spectral densities. In this respect, the American Federal Communications Commission (FCC) has approved the unlicensed use of the spectrum in the range 3.1 GHz–10.3 GHz. However, since such a large band nullifies the frequency independence assumption, common in small band antenna design, any description of UWB systems will have to inherently include frequency dependence and dispersion effects.

Research into far field WPT is hampered by the fact that full wave electromagnetic solvers are unable to simulate large and complex propagation environments, due to the discretization requirements of such problems. On the one hand, even though some antenna link simulation tools have been developed [6], none of those were able to take into account the inherent frequency dependence of UWB applications. On the other hand, existing UWB link descriptions [7], [8], do not handle intricate propagation environments. Statistical approaches to UWB channels have been used [9], [10], but they do not enable the designer to quantify the exact amount of power harvested for a given WPT system operating in well-known deterministic conditions. Therefore, we present a modular framework in which frequency dependence (as required for UWB) and complex multipath behaviour (e.g. indoor environment) are unified in order to simulate and accurately predict WPT at a low computational cost. The proposed framework constructs frequency-dependent antenna links based on stand-alone blocks. Each of the blocks can be a mathematical description, a

[1] an UWB system has a bandwidth exceeding the lesser of 500 MHz and 20 % of its centre frequency

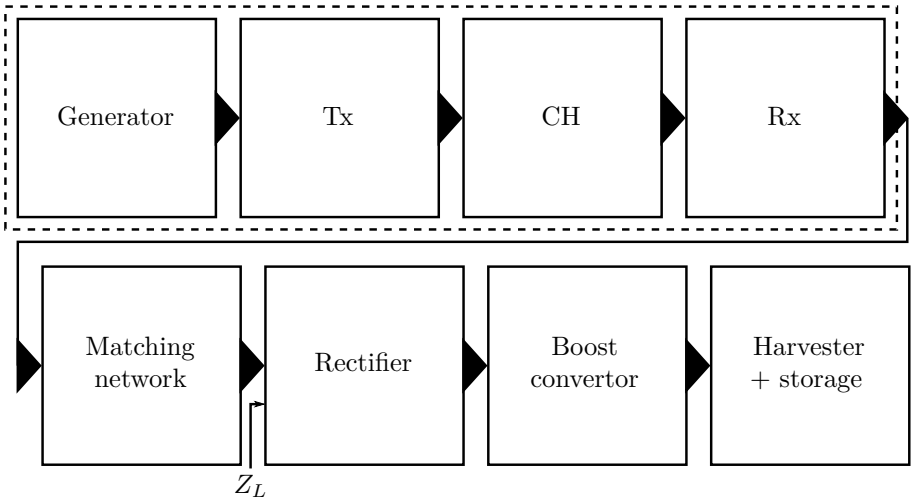

Figure 5.1: A WPT link from generator to harvester (and storage), including a generator, a transmit antenna (Tx), a propagation channel (CH), a receive antenna (Rx), a matching network, a rectifier, a boost converter and a harvester with energy storage.

simulation, a measurement or a third party black box description of an antenna, propagation channel (e.g. the statistical approaches to UWB propagation as mentioned before) or any building blocks forming part of the intricate antenna link. This general approach allows developers to pick the best or most appropriate technique for each part and insert it into the model, but it also allows manufacturers to provide a component description without compromising intellectual property by disclosing a particular design.

5.2 Theory

In Fig. 5.1, a typical WPT link from generator to harvester (and storage) is depicted. It includes a generator, a transmitter (Tx), a propagation channel (CH), a receiver (Rx), a matching network, a rectifier, a boost converter and a harvester with energy storage. Of interest here is the amount of power that can be harvested and stored given a certain amount of generated power. In this chapter, we will analyse and optimize only part of this link, being the antenna link with a complex propagation channel as enclosed by the dashed box in Fig. 5.1. The antenna link, presented in more detail in Fig. 5.2, is assumed to be terminated by a load impedance Z_L ($\Re Z_L = R_L$). We will particularly focus on the ratio between the power harvested at the load (P_L)

$$P_L = \frac{R_L}{2} \frac{|V_o|^2}{|Z_L|^2} \tag{5.1}$$

where V_o is the open circuit voltage of the receive antenna, further defined by (5.6) and the maximum available power (P_s)

$$P_s = \frac{1}{8}\frac{|V_s|^2}{R_s} \ , \tag{5.2}$$

that may be delivered by the source V_s (with impedance Z_s and $\Re Z_s = R_s$) to a transmit antenna in ideal matching conditions. In reality, the transmit antenna has an internal impedance Z_T. Therefore one might want to consider the actual power generated by V_s or the power radiated by Tx.

When the transmitter and the receiver are both free standing antennas located in free space with only a direct path between them, the received power as a function of the maximum power delivered by the source's generator is described by the Friis transmission formula [11]. In case of an UWB context, all quantities involved become frequency dependent, resulting in

$$P_R(f) = M_R(f) \cdot G_R(f) \cdot Q_{RT}(f) \cdot \left(\frac{c}{4\pi f d}\right)^2 \cdot G_T(f) \cdot M_T(f) \cdot P_T(f) \tag{5.3}$$

with M_R, M_T, G_R and G_T the mismatch factor (M) and the power gain (G) of the receive ($_R$) and the transmit ($_T$) antennas, respectively, $(4\pi df/c)^2$ the free space path loss and Q_{RT}, the polarisation mismatch, defined by

$$Q_{RT} = \frac{|\boldsymbol{F}_R(-\boldsymbol{u}) \circ \boldsymbol{F}_T(\boldsymbol{u})|^2}{|\boldsymbol{F}_R(-\boldsymbol{u})|^2 |\boldsymbol{F}_T(\boldsymbol{u})|^2} \tag{5.4}$$

with $\boldsymbol{F}_R(-\boldsymbol{u})$ and $\boldsymbol{F}_T(\boldsymbol{u})$ the far field vector of the receive and transmit antenna, respectively, for a unit current and '$\circ$' the scalar product. The far field vector $\boldsymbol{F}(\boldsymbol{u}) = \left[F^V(\boldsymbol{u}), F^H(\boldsymbol{u})\right]$ consists of a vertical (^{V}) and horizontal (^{H}) polarisation component. The path loss depends on the distance d between transmitter and receiver, c the speed of light and the frequency.

The Friis transmission formula expresses power transmission in an ideal situation and is insufficient to express power transmission in a multipath environment or with antennas placed on the human body, located on or in walls or, in general, in 'complex' environments. In order to describe such a more intricate configuration, one has to derive the power transmission based on the voltages and currents on both antennas.

From Fig. 5.2 one can derive the voltage dissipated in the load (Z_L) as

$$V_2 = \frac{Z_L}{Z_L + Z_R} V_o \tag{5.5}$$

with Z_R the internal impedance of the receiving antenna. The open circuit voltage V_o is given by

$$V_o = \frac{-2\jmath c}{\eta f}\left(\boldsymbol{F}_R(-\boldsymbol{u}) \circ \boldsymbol{E}^{inc}\right) \tag{5.6}$$

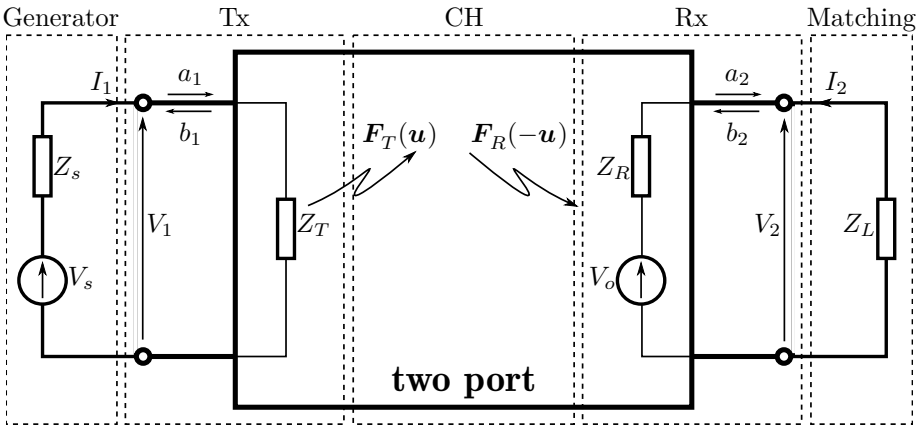

Figure 5.2: Schematics of a two-port network representation of the antenna link. The antenna link consists of a transmit antenna Tx (with internal impedance Z_T and far field vector $\boldsymbol{F}_T(\boldsymbol{u})$) powered by a generator (V_s with impedance Z_s) and a receive antenna Rx (with internal impedance Z_R and far field vector $\boldsymbol{F}_R(-\boldsymbol{u})$) terminated by a load Z_L.

with $\jmath$ the complex unit, η the free space impedance and $\boldsymbol{E}^{inc}$ the electric field of an impinging plane wave. From this point on, all far field vectors will include the effect of all objects in the reactive near field of the antenna, but the notation for the far field vector remains unaltered. Under the far field assumption and in a multipath environment, $\boldsymbol{E}^{inc}$ can be replaced by the electric field generated by the transmit antenna. This means

$$\Big(\boldsymbol{F}_R(-\boldsymbol{u}) \circ \boldsymbol{E}^{inc}\Big) = I_1 \sum_i \frac{\mathrm{e}^{-\jmath k d_i}}{d_i} \Big(\boldsymbol{F}_R(-\boldsymbol{u}_i) \circ \overline{\overline{\boldsymbol{\Gamma}}}_i \circ \boldsymbol{F}_T(\boldsymbol{u}_i)\Big) \tag{5.7}$$

with $k = 2\pi f/c$ the free space wave number, $\boldsymbol{u}_i$ and $-\boldsymbol{u}_i$ the transmit and receive direction of the i^{th} path, respectively, d_i the length of the i^{th} path and $\overline{\overline{\boldsymbol{\Gamma}}}_i$ a full tensor containing the product of the γ reflections and transmissions (numbered 0 to $\gamma - 1$) along the i^{th} path.

$$\overline{\overline{\boldsymbol{\Gamma}}}_i = \prod_{j=0}^{\gamma-1} \begin{cases} \overline{\overline{\boldsymbol{R}}}_{i,\gamma-1-j} & \text{if the } j^{\text{th}} \text{ interaction is a reflection} \\ \overline{\overline{\boldsymbol{T}}}_{i,\gamma-1-j} & \text{if the } j^{\text{th}} \text{ interaction is a transmission} \end{cases} \tag{5.8}$$

The index j 'follows' the i^{th} path from transmitter to receiver as it goes through a series of transmissions and reflections. This means, that if the i^{th} path is first reflected on a surface and then twice transmitted through others, we have that $\overline{\overline{\boldsymbol{\Gamma}}}_i = \overline{\overline{\boldsymbol{T}}}_{i,0}\overline{\overline{\boldsymbol{T}}}_{i,1}\overline{\overline{\boldsymbol{R}}}_{i,2}$.

$\overline{\overline{\boldsymbol{R}}}_{i,j}$ and $\overline{\overline{\boldsymbol{T}}}_{i,j}$ are expressed in the same 'vertical-horizontal' base as the antenna polarisation. They are obtained by rotating the diagonal tensors $\overline{\overline{\boldsymbol{R}}}^{D}_{i,j} =$

diag $\left(R_{i,j}^{\mathrm{TE}}, R_{i,j}^{\mathrm{TM}}\right)$ and $\overline{\overline{\boldsymbol{T}}}_{i,j}^{D} = \mathrm{diag}\left(T_{i,j}^{\mathrm{TE}}, T_{i,j}^{\mathrm{TM}}\right)$ over the correct angle. The components of $\overline{\overline{\boldsymbol{R}}}_{i,j}^{D}$ and $\overline{\overline{\boldsymbol{T}}}_{i,j}^{D}$ are the reflection and transmission coefficients of a wave with a polarisation parallel and perpendicular to the normal of the reflection plane. The reflection coefficients are given by

$$R_{i,j}^{\mathrm{TM}} = \frac{\varepsilon_r \sin\psi_{i,j} - \sqrt{\varepsilon_r - \cos^2\psi_{i,j}}}{\varepsilon_r \sin\psi_{i,j} - \sqrt{\varepsilon_r - \cos^2\psi_{i,j}}} \tag{5.9}$$

$$R_{i,j}^{\mathrm{TE}} = \frac{\sin\psi_{i,j} - \sqrt{\varepsilon_r - \cos^2\psi_{i,j}}}{\sin\psi_{i,j} - \sqrt{\varepsilon_r - \cos^2\psi_{i,j}}} \tag{5.10}$$

with $\psi_{i,j}$ the angle of incidence of i^{th} path at the j^{th} transmission or reflection (see Fig. 5.5) and $\overline{\overline{\boldsymbol{T}}}_{i,j}^{D} = \overline{\overline{\mathbf{1}}} + \overline{\overline{\boldsymbol{R}}}_{i,j}^{D}$, with $\overline{\overline{\mathbf{1}}}$ the unity tensor. Note that the expression for $\overline{\overline{\boldsymbol{\Gamma}}}_i$ will be frequency dependent.

Expressing I_1 in (5.7) as a function of the generator voltage V_s, the generator impedance Z_s and the internal impedance of the transmit antenna Z_T results in

$$V_2 = \frac{Z_L}{Z_L + Z_R} \frac{-2\jmath c}{\eta f} \left[\sum_i \frac{\mathrm{e}^{-\jmath k d_i}}{d_i} \left(\boldsymbol{F}_R(-\boldsymbol{u}_i) \circ \overline{\overline{\boldsymbol{\Gamma}}}_i \circ \boldsymbol{F}_T(\boldsymbol{u}_i) \right) \right] \frac{1}{Z_T + Z_s} V_s \ . \tag{5.11}$$

The polarisation mismatch can be written as q, the cosine of the angle between the far field vectors of the transmitting and the receiving antenna, as given below

$$q = \frac{\boldsymbol{F}_T(\boldsymbol{u}_0) \circ \boldsymbol{F}_R(-\boldsymbol{u}_0)}{|\boldsymbol{F}_T(\boldsymbol{u}_0)||\boldsymbol{F}_R(-\boldsymbol{u}_0)|} \ , \tag{5.12}$$

with $\boldsymbol{F}_R(-\boldsymbol{u}_0)$ and $\boldsymbol{F}_T(\boldsymbol{u}_0)$ associated to the direct path and $Q = |q|^2$.

In order to bring the far field vectors outside of the sum, one can replace $\overline{\overline{\boldsymbol{\Gamma}}}_i$ by

$$\Gamma_i' = \frac{\boldsymbol{F}_R(-\boldsymbol{u}_i) \circ \overline{\overline{\boldsymbol{\Gamma}}}_i \circ \boldsymbol{F}_T(\boldsymbol{u}_i)}{\boldsymbol{F}_R(-\boldsymbol{u}_0) \circ \boldsymbol{F}_T(\boldsymbol{u}_0)} \ , \tag{5.13}$$

and thus

$$\boldsymbol{F}_R(-\boldsymbol{u}_i) \circ \overline{\overline{\boldsymbol{\Gamma}}}_i \circ \boldsymbol{F}_T(\boldsymbol{u}_i) = \left|\boldsymbol{F}_T(\boldsymbol{u}_0)\right| \cdot q \cdot \Gamma_i' \cdot \left|\boldsymbol{F}_R(-\boldsymbol{u}_0)\right| \tag{5.14}$$

Then define H_R and H_T as below

$$\begin{aligned} \frac{V_2}{V_s} &= \underbrace{\left(\frac{|\boldsymbol{F}_R(-\boldsymbol{u}_0)|}{Z_L + Z_R} \right)}_{H_R} \underbrace{\left(\frac{-2\jmath c}{\eta f} Z_L q \sum_i \Gamma_i' \frac{\mathrm{e}^{-\jmath k d_i}}{d_i} \right)}_{H_{CH}} \underbrace{\left(\frac{|\boldsymbol{F}_T(\boldsymbol{u}_0)|}{Z_T + Z_s} \right)}_{H_T} \ . \\ &= \end{aligned} \tag{5.15}$$

(5.15) is written down as a product of transfer functions, which mimics well the block model that was presented in Fig. 5.1. This property will be exploited later on.

Based on (5.15), (5.1) and (5.2), the ratio P_L to P_s is given by

$$\frac{P_L}{P_s} = 4R_L \left| \frac{\boldsymbol{F}_R(-\boldsymbol{u}_0)}{Z_L + Z_R} \right|^2 \left| \frac{-2\jmath c}{\eta f} Z_L q \sum_i \Gamma_i' \frac{\mathrm{e}^{-\jmath k d_i}}{d_i} \right|^2 \left| \frac{\boldsymbol{F}_T(\boldsymbol{u}_0)}{Z_s + Z_T} \right|^2 R_s \ . \tag{5.16}$$

To use the theory above, one has to obtain data for the transfer function of an antenna. This means that for an antenna placed on the human body, the transfer function of the antenna on the body (instead of 'just the transfer function of the stand-alone antenna') should be measured or simulated. When relying on simulations, one uses the expression

$$\boldsymbol{H}_x = \frac{\boldsymbol{F}_x(\boldsymbol{u})}{Z_x + Z_L} \ , \tag{5.17}$$

for antenna x with internal impedance Z_x and terminated by Z_L. To measure the transfer function of an antenna, a full 3D far field vector of the antenna is needed. This quantity is obtained through a three-antenna measurement. Note that the three-antenna measurement has to be performed for the vertical and the horizontal polarisation. The three-antenna measurement consists of measuring the S_{21} between any pair of the three antennas. From two-port theory, one can easily derive an expression for S_{21} as a function of port voltages. Given the two-port in Fig. 5.2, the standard expressions for the S-parameters are given by (5.18)

$$S_{11} = \left.\frac{b_1}{a_1}\right|_{a_2=0} \quad S_{12} = \left.\frac{b_1}{a_2}\right|_{a_1=0} \quad S_{21} = \left.\frac{b_2}{a_1}\right|_{a_2=0} \quad S_{22} = \left.\frac{b_2}{a_2}\right|_{a_1=0} \ . \tag{5.18}$$

and the necessary expressions for the forward and backwards normalized voltage waves given by (5.19) (with '*' the complex conjugate, $V_s = V_1 + Z_s I_1$, $V_2 = -Z_L^* I_2$ and under the assumption that the two-port is terminated by two impedances satisfying $|\Re Z_L| = |\Re Z_s|$).

$$\begin{aligned} a_1 &= \frac{1}{2} \frac{V_1 + Z_s I_1}{\sqrt{|\Re Z_s|}} & b_1 &= \frac{1}{2} \frac{V_1 - Z_s^* I_1}{\sqrt{|\Re Z_s|}} \\ a_2 &= \frac{1}{2} \frac{V_2 + Z_L I_2}{\sqrt{|\Re Z_L|}} & b_2 &= \frac{1}{2} \frac{V_2 - Z_L^* I_2}{\sqrt{|\Re Z_L|}} \end{aligned} \tag{5.19}$$

S_{21} then yields

$$S_{21} = \frac{b_2}{a_1} = \frac{\sqrt{|\Re Z_s|}\left(V_2 - Z_L^* I_2\right)}{\sqrt{|\Re Z_L|}(V_1 + Z_s I_1)} = \frac{2V_2}{V_s} \ . \tag{5.20}$$

Leveraging the block model, one can express S_{21} for the vertical polarisation (the expression for the horizontal polarisation is similar) as

$$S_{21}^V = \frac{2V_2}{V_s} = 2H_R^V \cdot H_{CH}^V \cdot H_T^V \ . \tag{5.21}$$

Given three antennas, labelled x, y and z, one can write down the relation above for every pair of antennas, resulting in a set of three equations (the polarisation indication is suppressed)

$$\begin{cases} S_{21}^{xy} = 2 \cdot H_x \cdot H_{CH}^{xy} \cdot H_y \\ S_{21}^{yz} = 2 \cdot H_y \cdot H_{CH}^{yz} \cdot H_z \\ S_{21}^{zx} = 2 \cdot H_z \cdot H_{CH}^{zx} \cdot H_x \ . \end{cases} \tag{5.22}$$

This can be solved for the different transfer functions. H_x is given by

$$H_x = \sqrt{\frac{1}{2} \frac{S_{21}^{xy}}{H_{CH}^{xy}} \frac{H_{CH}^{yz}}{S_{21}^{yz}} \frac{S_{21}^{zx}}{H_{CH}^{zx}}} \ . \tag{5.23}$$

The expressions for H_y and H_z are the same, a permutation of antenna indices aside. Calculating the above for both the vertical and the horizontal polarisation results in

$$\boldsymbol{H}_x = \left[H_x^V, H_x^H \right] \ . \tag{5.24}$$

5.3 Theory validation

As mentioned before, an antenna link can be described with a block model. In terms of power, the model is given by

$$\frac{P_L}{P_s} = |\boldsymbol{S}_{21}|^2 = 4|\boldsymbol{H}_R|^2 |\boldsymbol{H}_{CH}|^2 |\boldsymbol{H}_T|^2 \ , \tag{5.25}$$

in which the propagation channel can be complex e.g. due to various paths along which the signal can travel.

A commercial, off the shelf, UWB test bed [12] was used to validate the theory. The test bed includes a UWB monopole antenna (see Fig. 5.3, [13]) designed to operate in the frequency range 3.1 GHz–5.3 GHz. However, no accurate physical description of the monopole's geometry and materials was available. To use this antenna in simulations, one has to build a model by measuring the physical dimensions of the antenna and by estimating the dielectric properties of the antenna substrate. In the end, this may result in a decent approximation. On the other hand, this is not really necessary. The proposed framework allows to incorporate a measured far field vector, gain or other antenna figure of merit into the block model instead of approximate simulations. In the light of validating our theory, we apply both approaches.

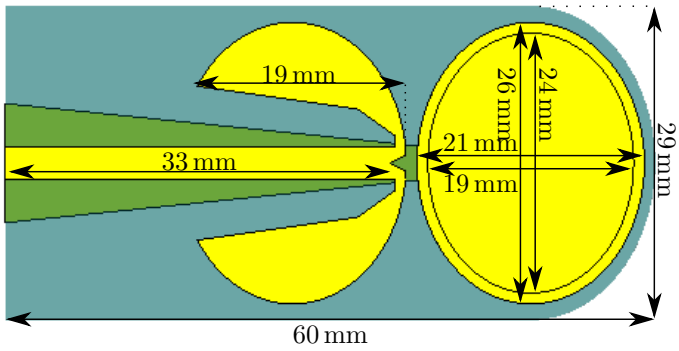

Figure 5.3: UWB monopole as recreated in CST-MWS®

To obtain the antenna transfer function, the suggested three-antenna measurement was performed with the UWB monopole [13], an UWB horn [14] and two standard gain horns[2] (Scientific Atlanta's 12-2.6 and 12-3.9 standard gain horns [15]). The antenna transfer function is then calculated following the procedure in (5.23). The channel transfer function in the anechoic chamber equals

$$\boldsymbol{H}_{CH} = \boldsymbol{H}_{FS} = \frac{-2\jmath f Z_L}{\eta c} \frac{\mathrm{e}^{-\jmath kd}}{d} \,. \tag{5.26}$$

To validate our theory, we would like to simulate the antenna links we measured in the anechoic chamber with the time domain solver of Computer Simulation Technology's Microwave Studio® (CST-MWS®). Unfortunately, this is impossible due to the large antenna spacing (5 m or approximately 51 λ at 3.1 GHz) and the size of the horn antennas. It was, however, possible to simulate a full monopole to monopole link over a distance of 0.5 m ($\approx$5 λ) with CST-MWS®. A distance of 0.5 m does not really correspond to the far field at the considered frequencies. To verify the accuracy of the link simulation at that distance, another CST-MWS® simulation was performed at 0.75 m, applying a less dense mesh. Then, the radiation vector resulting from the electric field observed at 0.75 m was compared to the one calculated at 0.5 m. A reasonably good agreement was found between both results, verifying the far field approximation for a distance of 0.5 m, within a reasonable accuracy.

To reproduce this result with measurement data, the monopole transfer function was extracted from the measurements and the propagation transfer function was replaced by (5.26) for an antenna spacing of $d = 5$ m. In addition, the antenna transfer function of the monopole was also calculated from a stand-alone simulation of the antenna using (5.17). As an extra way of validating the theory, the Friis transmission formula was also used to calculate the power transmitted from the one monopole to the other.

[2] together they completely cover the required frequency range

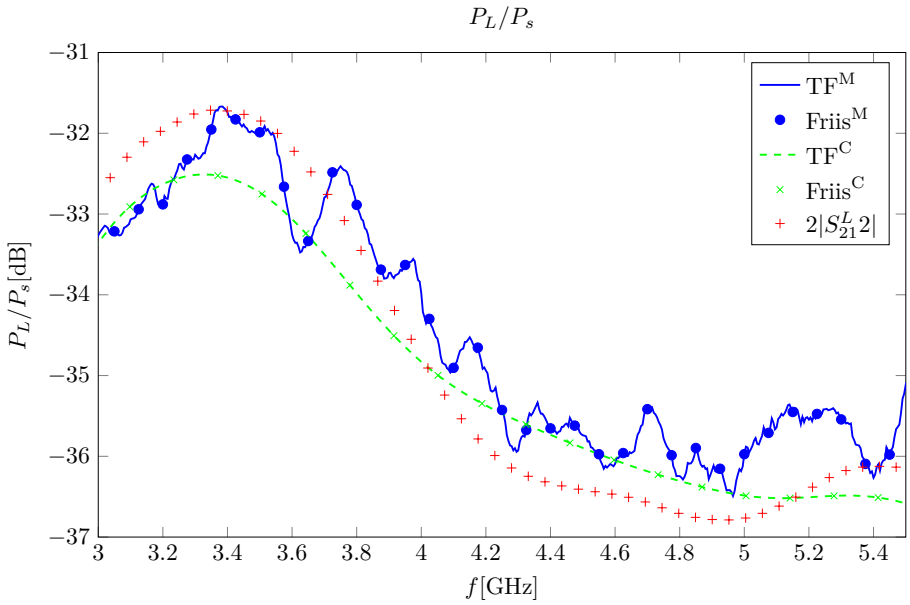

Figure 5.4: The power ratio $\frac{P_L}{P_s}$, calculated in different ways: using the monopole's measured transfer function (TF^M, blue, solid), using the Friis transmission formula based on measurements (Friis^M, blue, dots), using the monopole's simulated (stand-alone) transfer function (TF^C, green, dashed), using the Friis transmission formula based on a stand-alone simulation (Friis^C, green, crosses) and using $|\boldsymbol{S}_{21}|^2$ as directly simulated ($\left|\boldsymbol{S}_{21}^{L}\right|^2$, red, pluses)

Next, all the expressions for the ratio between received and transmitted power are calculated and plotted in Fig. 5.4. First, the power ratio was calculated using the measured monopole's transfer function (TF^M, blue, solid)

$$\frac{P_L}{P_s} = 4\left|\boldsymbol{H}^M\right|^2\left|\boldsymbol{H}_{CH}\right|^2\left|\boldsymbol{H}^M\right|^2 \tag{5.27}$$

and using Friis's formula with measured gain and reflection coefficient (Friis^M, blue, dots)

$$\frac{P_L}{P_s} = G^M \cdot M^M \cdot \mathrm{PL}^{-1} \cdot M^M \cdot G^M \ . \tag{5.28}$$

Second, the power ratio was evaluated using stand-alone simulations of the monopole antenna based on transfer functions, (TF^C, green, dashed)

$$\frac{P_L}{P_s} = 4\left|\boldsymbol{H}^C\right|^2\left|\boldsymbol{H}_{CH}\right|^2\left|\boldsymbol{H}^C\right|^2 \tag{5.29}$$

and based on Friis's formula (Friis^C, green, crosses)

$$\frac{P_L}{P_s} = G^C \cdot M^C \cdot \mathrm{PL}^{-1} \cdot M^C \cdot G^C \ . \tag{5.30}$$

Finally, the power ratio was calculated using the $\boldsymbol{S}_{21}$ as simulated, without the transfer function extraction ($\left|\boldsymbol{S}_{21}^L\right|^2$, red, pluses)

$$\frac{P_L}{P_s} = \left|\boldsymbol{S}_{21}^L\right|^2 \ . \tag{5.31}$$

All antenna figures of merit used above relate to the UWB monopole and PL represents the path loss. The full link simulation in CST-MWS® lasted 4 h4 m14 s on a quad core system and used over 6.5 GB of RAM memory. A stand-alone simulation of the antenna only lasted 39 m25 s on the same system and used 3.7 GB RAM memory. The combination of the correct transfer functions took only seconds.

One can see that all data are in good agreement. Differences between simulated data are due to the different meshes CST-MWS® applied to different set-ups and to the fact that the antenna separation does not really satisfy the far-field conditions.

Allowing for reflections on different surfaces complicates the basic configuration above. Adding a concrete floor 1.7 m below both transmitter and receiver results in one additional propagation path next to the direct path. This second path is indicated as such in Fig. 5.5. This set-up will be called the 'two-path' configuration. Adding a concrete ceiling 4 m above the floor gives raise to a, theoretically, infinite number of additional propagation paths between transmitter and receiver. The first three paths are depicted and labelled in Fig. 5.5. This set-up will be named 'three-path' configuration. The other paths, of which a few are also depicted, reflect twice, thrice and so on, on floor and ceiling. With every additional reflection, the propagation path becomes longer and its contribution to the power at the receiver diminishes. Our extensive simulations have shown that the ratio between received and transmitted power converges when fifteen propagation paths are considered.

The ratio between received and transmitted power as a function of frequency, for the three configurations mentioned above, is shown in Fig. 5.6. The two-path configuration results in predictable fluctuations around the direct path. Peaks and valleys are spaced approximately 141 MHz apart, corresponding with a wavelength of 1.06 m, which is almost equal to Δd between the direct path and the reflected path of 1.05 m. The three-path configuration complicates the result. The fluctuations around the power received via the direct path is less predictable and the relative height and depth of the peaks and valleys increases.

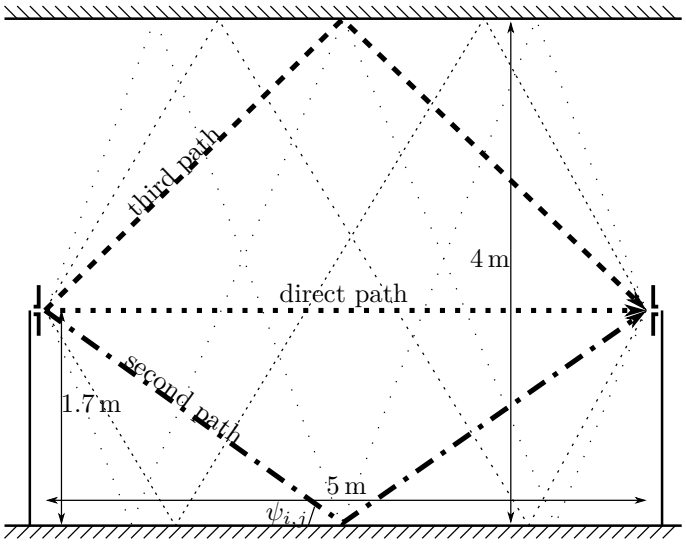

Figure 5.5: Simulation set-up consisting of a receiver and a transmitter 5 m apart both placed at a height of 1.7 m above ground. The direct path is represented by a dotted line, the first additional path by dash-dotted line and the third propagation path by a dashed line. The third propagation path is reflected from a 4 m high ceiling. The ceiling causes more paths to exist. Four additional paths are drawn in fine dashes and fine dots

5.4 Application

In the previous section, it was shown above that the proposed framework yields accurate results. We now apply it to determine the ideal distance between transmitter and receiver to optimize the power transmission. Let us consider the multipath configurations introduced above, where we place the receive antenna on the chest of a test person (1.75 m, 70 kg). The antenna was taped on the shirt of the test person and spacer fabrics were used to increase the spacing between body and antenna. Remark that when no spacer fabric was used, the antenna was deployed 2 to 3 mm (estimate) away from the body, because the antenna was positioned on a loose shirt. The linear UWB monopole was placed on the body in such a way that its polarisation was vertical and aligned with the vertical polarisation of the UWB horn used as transmit antenna in this measurement. Therefore, the horizontal polarised component in the measured $\boldsymbol{S}_{21}$ is very small and is neglected from here on. On-body data will be indicated by a subscript $_b$.

First of all, the system was excited with an UWB pulse, depicted in Fig. 5.7, with a duration of 6.1 ns. The pulse is normalized to have a power of 1 W. 99.95 % of the power of the pulse is concentrated in a time frame between

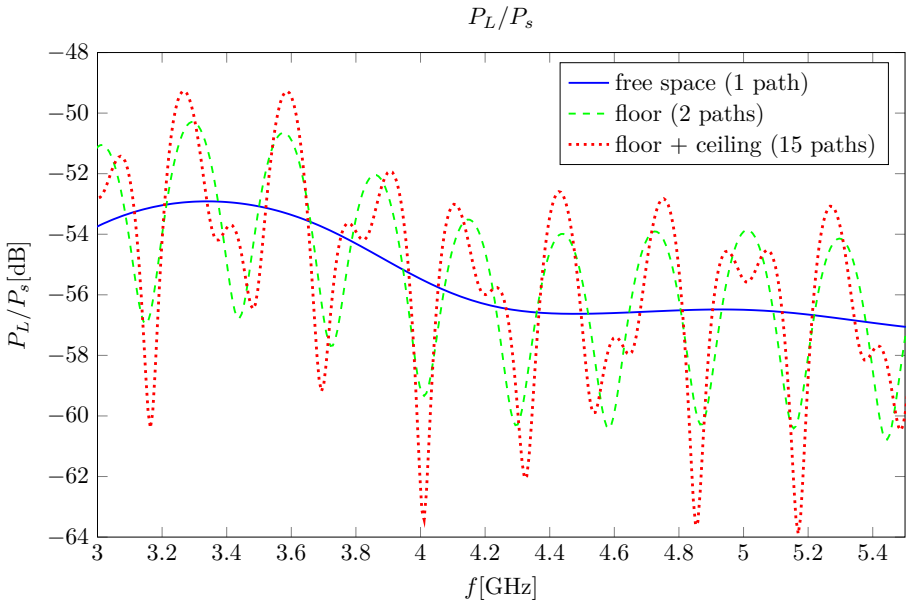

Figure 5.6: Power transfer over three different channels with a length of 5 m: free space propagation (Blue, solid), two-path model, sender and receiver are placed 1.7 m above ground (green, dashed) and a model consisting of the two-path model extended with a ceiling 4 m above ground (red, dotted).

0.47 ns and 4.34 ns, as indicated by red dashes in Fig. 5.7.

Second, the transfer function of the monopole antenna on the human body was measured ($\boldsymbol{H}_b^M$, see Fig. 5.8) for distances varying between 3 mm and 20 mm. Third, the transfer function was also simulated with CST-MWS® ($\boldsymbol{H}_b^C$, see Fig. 5.9). In the simulations, the human body was represented by a three layer ((dry) skin (1 mm), fat (3 mm) and muscle (18 mm)) tissue model of size 150 mm × 150 mm. The frequency dependent dielectric properties of the body tissues were obtained from [16].

Comparing simulations and measurements one can see that (except for the CST-MWS® simulation at a 3 mm spacing) the body acts as a reflector compared to the free-standing scenario and therefore, the amount of power received over the WPT link increases. In general, measurements show larger transfer functions than the simulations do. It also needs to be noted that, for an antenna-body spacing of 20 mm, the monopole's transfer function shows a clear dip at $f = 5.25$ GHz (down to −30 dB). In Fig. 5.9, one can see that, for the same spacing, the transfer function does decrease, but does not show the same steep dip. The (shallow) dip in the simulation results occurs for $f > 5.5$ GHz. This might be caused by the three-layer model of the body used for the simulations,

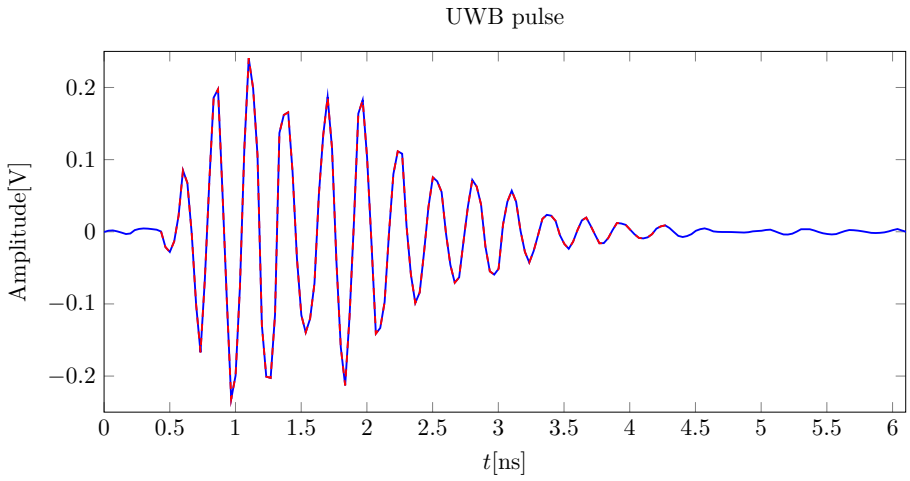

Figure 5.7: UWB pulse (blue). The part containing 99.95 % of pulse's power is marked with red dashes (between 0.47 ns and 4.34 ns).

which might be overly simple.

Let it be clear that it is extremely difficult to accurately model the interaction of electromagnetic radiation with the human body. Besides, the simulations of the antenna on the human body were also time and memory consuming. Fortunately, the tedious and to a greater or lesser extent inaccurate process of running the on-body simulations, can be entirely circumvented by using the proposed framework and by plugging in measurements of the antenna deployed on the body into the simulation. Using the on-body measurements, the power delivered to the on-body antenna (P_L) by the free-standing antenna (P_s) is expressed by (with $\boldsymbol{H}^C$ the stand-alone simulated monopole transfer function in free space)

$$P_L = 4 \cdot \left|\boldsymbol{H}_b^M\right|^2 \cdot \left|\boldsymbol{H}_{CH}\right|^2 \cdot \left|\boldsymbol{H}^C\right|^2 \cdot P_s \ . \tag{5.32}$$

Finally, to put emphasis on the difference between a single direct propagation path and two-path propagation, the results are normalized with respect to the (direct) distance (d) between transmitter and receiver. This means that the result is divided by the energy transmitted along the direct path. Therefore, if the result is larger (smaller) than one, more (less) energy is transported by the two-path system compared to the direct propagation scenario. The differences between multipath and direct path propagation are caused by the Δd (rather than by the direct propagation distance d). Therefore results will be presented as a function of Δd (rather than d).

In Fig. 5.10, the received power is plotted as a function of Δd for a two-path link. First note that the effect of the second path is independent of the

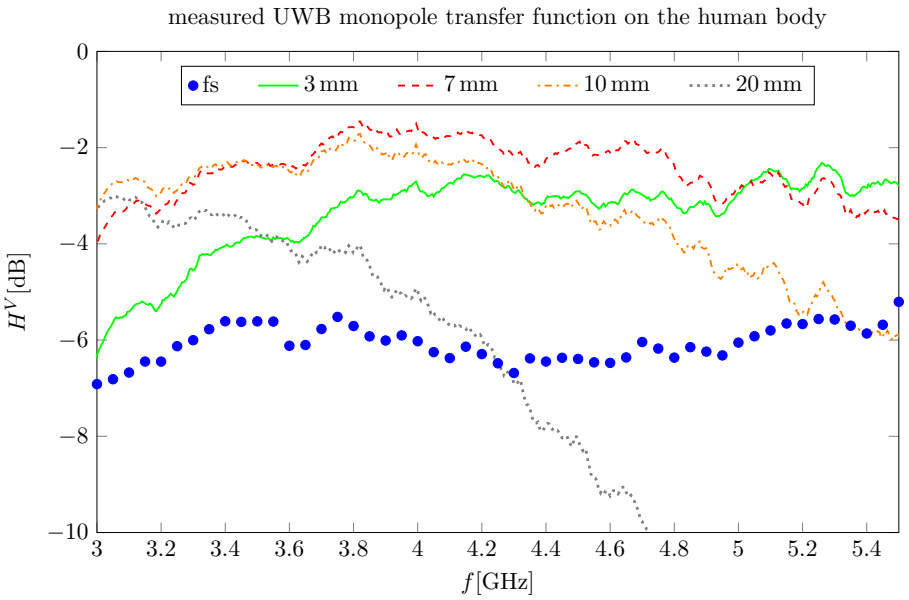

Figure 5.8: the transfer function of the UWB monopole placed on the human body as measured for distances varying between 3 mm and 20 mm. As a reference the transfer function of the free-standing monopole (blue, dots) is added.

spacing between the antenna and the human body. One can observe that, for $\Delta d > 1.3$ m, the curve is flat and slightly larger than one. This means that the second path delivers additional power to the receive antenna (compared to only a direct path). A Δd of 1.3 m corresponds to a time delay between the two pulses of 4.34 ns. Since almost all the energy of the pulse is concentrated in a smaller time frame, no interference occurs. A Δd of 1.3 m corresponds to a direct path length of 3.79 m (given that transmitter and receiver are placed at a height of 1.7 m)

When Δd drops below 1.3 m, the pulses received over both propagation paths overlap more and more and a pattern of constructive and destructive interference appears. The pattern is fairly regular, the constructive interference peaks increase with decreasing Δd, while the destructive interference dips deepen. The distance between peaks is fixed at about 0.085 m. The highest additional relative power transmission caused by the second path occurs for a Δd of 0.042 m.

Similar to the adopted approach at the end of section 5.3, a concrete ceiling is added 4 m above the floor. As mentioned in section 5.3, fifteen propagation paths are considered, because this was found to be the minimum number of paths to ensure convergence in the received versus transmitted power ratio. The

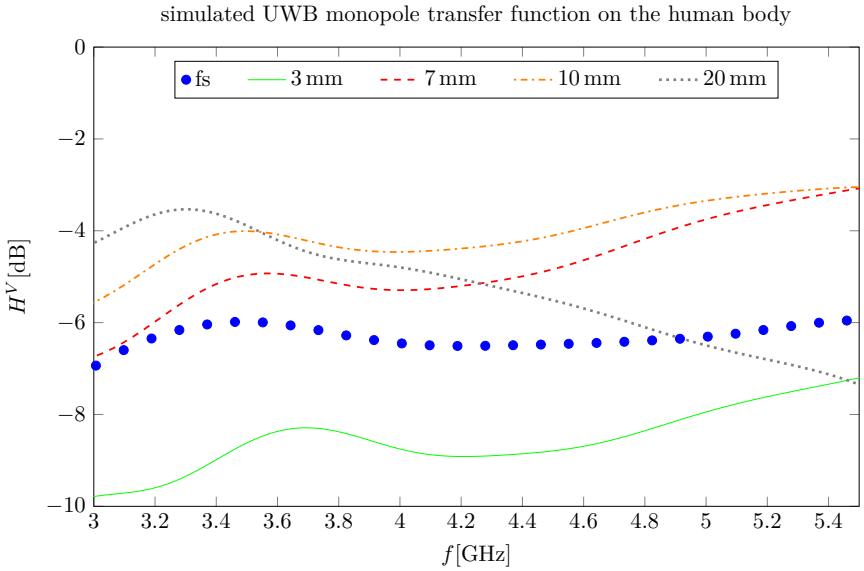

Figure 5.9: the transfer function of the UWB monopole placed on the human body as simulated with CST-MWS® for distances varying between 3 mm and 20 mm. As a reference the transfer function of the free-standing monopole (blue, dots) is added.

results for the received power are displayed in Fig. 5.11. Note that Δd is not uniquely defined, because there is a difference between the direct path and all the indirect paths. We chose Δd to be the difference between the direct path and the first reflected path (as above). Adding thirteen propagation paths on top of the two in the two-path configuration, destroys the regularity observed in the two-path case. Now it is impossible to easily predict the next peak in the received power with a simple formula. But the proposed framework solves this problem. From Fig. 5.11 one can see that the highest additional relative power transmission via the multiple paths occurs for a Δd of 0.15 m.

5.5 Conclusion and future research

In this paper, a framework for the simulation of frequency dependent, multi-path configurations was presented. It was shown that the framework provides accurate results in the simulation of antenna links and power transmitted over them. As an example, the ideal distance between transmitter and receiver for maximal power transfer was determined for two more complex propagation channels. In future research even more intricate propagation channels should be studied, modelled and included in the framework, to make it more versatile.

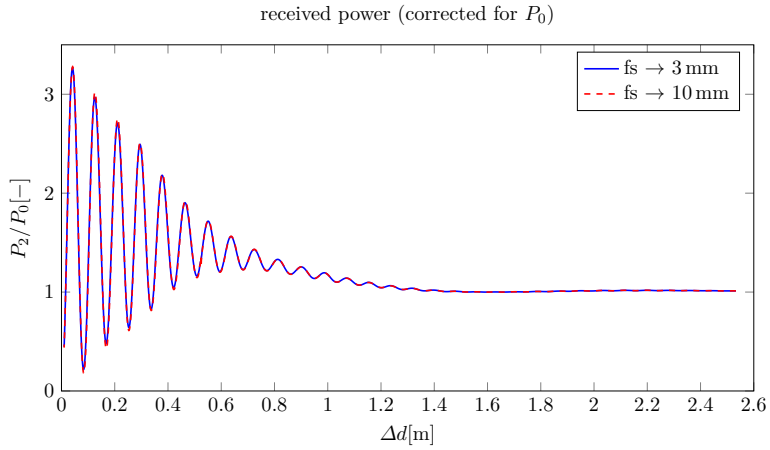

Figure 5.10: Received power versus Δd for the two-path configuration (P_2, Tx→Rx, free-standing (fs) to on-body), corrected for the power received via the direct path (P_0)

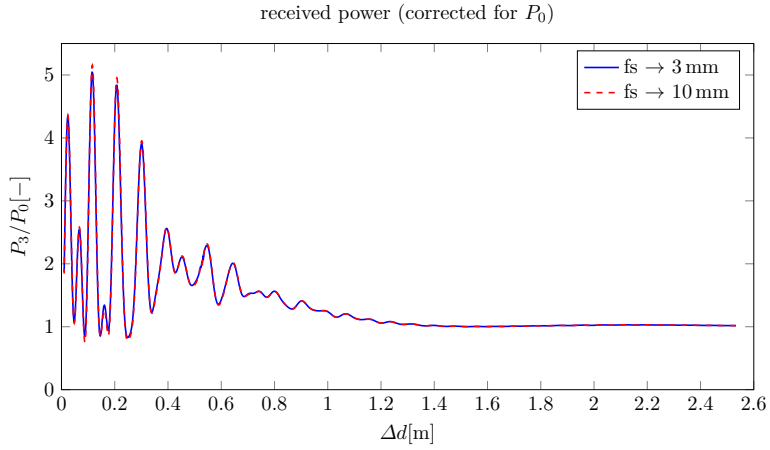

Figure 5.11: Received power versus Δd for the three-path configuration (P_3, Tx→Rx, free-standing (fs) to on-body), corrected for the power received via the direct path (P_0)

Extra attention should also be paid to polarisation cross-over in reflected paths, especially for rough surfaces.

References

[1] G. De Vita and G. Iannaccone, "Design criteria for the RF section of UHF and microwave passive RFID transponders", *Microwave Theory and Techniques, IEEE Transactions on*, vol. 53, no. 9, pp. 2978–2990, Sep. 2005, issn: 0018-9480.

[2] A. Dolgov, R. Zane, and Z. Popovic, "Power Management System for Online Low Power RF Energy Harvesting Optimization", *Circuits and Systems I: Regular Papers, IEEE Transactions on*, vol. 57, no. 7, pp. 1802–1811, Jul. 2010, issn: 1549-8328.

[3] C. Walsh, S. Rondineau, M. Jankovic, and G. Zhao, *A Conformal 10 GHz Rectenna for Wireless Powering of Piezoelectric Sensor Electronics*, 2005. [Online]. Available: `http://ecee.colorado.edu/microwave/docs/publications/2005/2005%20Rectenna%20Paper.pdf`.

[4] Wireless Power Consortium, *Qi standard*, 2009. [Online]. Available: `http://www.wirelesspowerconsortium.com/`.

[5] Power Matters Alliance, *PMA Inductive Wireless Power and Charging Specifications for Receiver (Rx), Transmitter (Tx), and Host Control Interface (HCI)*. [Online]. Available: `http://www.powermatters.org/`.

[6] V. Rizzoli, A. Costanzo, D. Masotti, P. Spadoni, and A. Neri, "Prediction of the End-to-End Performance of a Microwave/RF Link by Means of Nonlinear/Electromagnetic Co-Simulation", *Microwave Theory and Techniques, IEEE Transactions on*, vol. 54, no. 12, pp. 4149–4160, Dec. 2006, issn: 0018-9480.

[7] W. Wiesbeck, G. Adamiuk, and C. Sturm, "Basic Properties and Design Principles of UWB Antennas", *Proceedings of the IEEE*, vol. 97, no. 2, pp. 372–385, Feb. 2009, issn: 0018-9219.

[8] S. Promwong and P. Panthap, "Experimental evaluation of complex form Friis' transmission formula with indoor/outdoor for ultra wideband inpulse radio", in *Computer and Communication Engineering, 2008. ICCCE 2008. International Conference on*, May 2008, pp. 1037–1041.

[9] A. Sani, A. Alomainy, and Y. Hao, "Characterisation of ultra wideband wearable antennas and body-centric wireless-networks in indoor environment", in *Wireless Technology, 2008. EuWiT 2008. European Conference on*, Oct. 2008, pp. 135–138.

[10] R. Di Bari, Q. H. Abbasi, A. Alomainy, and Y. Hao, "An Advanced UWB Channel Moel For Body-Centric Wireless Networks", *Progress In Electromagnetics research*, vol. 136, pp. 79–99, 2013.

[11] H. Friis, "A Note on a Simple Transmission Formula", *Proceedings of the IRE*, vol. 34, no. 5, pp. 254–256, May 1946, issn: 0096-8390.

[12] Time Domain, *Datasheet UWB Ranging Radio*. [Online]. Available: http://www.timedomain.com/datasheets/320-0289E%20P410%20Data%20Sheet.pdf.

[13] Time Domain, *Datasheet PulseOn 200*. [Online]. Available: http://www.timedomain.com/datasheets/TD_Broadspec_Antenna.pdf.

[14] Rhode & Schwartz, *Datasheet double ridged UWB horn HF906*. [Online]. Available: http://cdn.rohde-schwarz.com/pws/dl_downloads/dl_common_library/dl_brochures_and_datasheets/pdf_1/HF906_brief_e.pdf.

[15] Scientific Atlanta, *Datasheet 12-2.6 and 12-3.9 standard gain horns*. [Online]. Available: http://www.atecorp.com/ATECorp/media/pdfs/datasheets/Scientific-Atlanta-Series12_Datasheet.pdf.

[16] D. Andreuccetti, R. Fossi, and C. Petrucci, *An Internet resource for the calculation of the dielectric properties of body tissues in the frequency range 10 Hz - 100 GHz*, F. (IFAC-CNR, Ed., 1997. [Online]. Available: http://niremf.ifac.cnr.it/tissprop/.

Conclusions

Presented research

In this thesis, two major problems were tackled. In the first part, local arbitrary subgridding of the Finite Difference Time Domain method (FDTD) meshes was introduced, whereas in the second part Wireless Power Transmission (WPT) over Ultra Wide Band (UWB) links was studied. In both topics, special attention was devoted to (spurious) reflections.

In part I, a novel technique was presented to relax the stringent requirement of uniform mesh cells in FDTD. This technique not only allows for more accurate modelling of objects that are either non-cuboidal, or not aligned according to the grid axes (thereby strongly reducing staircasing), but also results in a tremendous increase in calculation speed and a substantial reduction in memory use. In a first step, the theory was outlined for a classic FDTD grid. In a next step, the provided theory was extended towards Perfectly Matched Layers (PMLs). This extension provided additional benefits. Either reflections at the mesh/PML interface can be reduced, resulting in a more accurate solution, or the number of PML cells can be reduced at a minimal cost, again yielding a memory use reduction and a calculation speed increase. To validate the claims made, first, the influence of the type of subgridding (being parallel with respect to the coarse mesh/fine mesh interface, perpendicular with respect to the interface or both) on the magnitude of spurious reflections was investigated. From the results it was clear that parallel subgridding accounted for far larger spurious reflections than perpendicular subgridding did. This result was used in a second step to devise a strategy for terminating a mesh with a PML. One can either match the PML refinement to mimic the standard mesh refinement, or one can reduce the number of PML cells. Extensive simulations have shown that by parallelized unrefinement of the PML, the best trade-off between accuracy and calculation time was achieved. Finally, to quantify speed gains and memory reductions, the characteristic impedance of two representative configurations, being a stripline pair and a microstrip, were calculated and compared to the result obtained by an in-house tool, usging the Method of Moments. The simulations report speed-ups of up to a factor 5 and a memory reduction of up to a factor 6, without any concession to the accuracy.

In part II, the time consuming, tedious and costly simulation of Maxwell's equations was bypassed altogether in favour of the development of a specialist tool to calculate WPT for intricate UWB links. The transmitter, the receiver and the channel, being the building blocks of the antenna link, were represented using

a transfer function. Because of the frequency dependency of all building blocks, the antenna link had to be described in terms of amplitude and phase (rather than power), taking into account the aforementioned frequency dependency and a sequence of, again frequency dependent, transmissions and reflections the electromagnetic fields undergo while travelling from transmitter to receiver. The presented framework allows to incorporate measurement data, simulation data, models or a combination thereof as representations of the transfer functions. This provides tremendous freedom in the selection of the best data source. If one wants to determine the power delivered to systems near the human body, one has to take into account the influence of the human body on the antenna characteristics. This influence is difficult to simulate using tools such as Computer Simulation Technology's Microwave Studio® or Keysight Technology's EMPro 3D EM Simulation Software®. An accurate measurement of this interaction is much easier obtainable. The gathered data can then be used in the framework. On the other hand, the manufacturer of some system, can provide a black box model to use with the framework instead of disclosing his intellectual property, therefore allowing a client to run accurate simulations without giving up any industrial secret. The framework was tested by determining the points with best power reception in a UWB to UWB antenna link near the human body in a multipath environment, considering both a single reflection and a configuration with many reflections on a floor and a ceiling.

Future research

First, the existing FDTD code operates more as a proof of concept than as a fully-fledged software suite. A series of concepts such as finite conductivity, complex permittivity, non-linear materials, the total field - scattered field formalism, near field- far field transformation, discrete components (impedances, inductors, capacitors, ...), non-linear components (diodes, junctions, transistors, ...) and others were not implemented nor researched. The use of subgridding might make the implementation of these features not straightforward and might need some extra attention. For a complete product, however, one cannot get around these features.

Second, subgridding was only considered in the spatial domain. This resulted in a stable time step related to the smallest cell size in the mesh. If one could also subgrid in time, coarser cells would need less frequent updates, and, therefore, the total number of updates and consequently the total simulation time, can be reduced significantly. Some research effort has been dedicated to time subgridding by i.a. Ryan Chilton [1], but the problem was not yet solved. Some preliminary simulations have shown that the naive approach of just making the number of updates related to the relative cell size (thereby neglecting any subgridding theory) does work to some extent, but stable operation of the FDTD algorithm could not be guaranteed. It is clear that time subgridding is not a straightforward extension of the presented method and will need extensive

research to produce a stable, reciprocal temporal and spatial subgridded FDTD algorithm.

The second part of this thesis resulted in a framework for a quick simulation of UWB multipath environments. Additional validation could be done by completely measuring simple set-ups with a limited number of reflections, as a way to amend the work done using a crafty combination of simulations and measurements. This will require a careful measurement set-up in the anechoic chamber. A second topic worthy of further research, is the study of even more complex propagation channels, with an emphasis on polarisation cross-over in reflected paths, the effect of rough surfaces and other realistic properties of the channels and materials involved that were not considered so far.

References

[1] R. A. Chilton, "H-, P-, And T-Refinement Strategies For The Finite-Difference-Time-Domain (FDTD) Method Development Via Finite-Element (FE) Principles", PhD thesis, Ohio State University, 2008.